

ISSN:1305-130X

e-ISSN:1305-1385

CELAL BAYAR UNIVERSITY JOURNAL OF SCIENCE



Manisa Celal Bayar Üniversitesi
Fen Bilimleri Dergisi

2024

VOLUME:20

ISSUE:2



Journal of Science

Volume: 20, Issue: 2, Year: 2024

Contact

Manisa Celal Bayar University

The Graduate School

Campus of Şehit Prof Dr İlhan Varank 45140 Yunusemre – MANİSA, TÜRKİYE

Tel: (00 90) 236 201 27 05

Fax: (00 90) 236 241 21 49

e-mail: lee.fendergi@cbu.edu.tr

Web: <https://dergipark.org.tr/tr/pub/cbayarfbe>

“CBU Journal of Science is indexed by ULAKBIM-TUBITAK TR-DIZIN”



ISSN 1305-130X

E-ISSN 1305-1385

CBUJOS is published quarterly at The Graduate School of Manisa Celal Bayar University

“CBU Journal of Science is a refereed scientific journal”



Celal Bayar University Journal of Science

Owner: Manisa Celal Bayar University, The Graduate School

Editor in Chief: Prof. Dr. Kamil ŞİRİN

Editor: Assoc. Prof. Dr. İlker Çetin KESKİN

Layout Editor & Secretary

Res. Assist. Musa OVALI

Res. Assist. Gencay TEPE

Subject Editors

Prof. Dr. Abdullah AKDOĞAN, Pamukkale University, Chemical Engineering

Prof. Dr. Ali KONURALP, Manisa Celal Bayar University, Mathematics

Prof. Dr. Fatih KALYONCU, Manisa Celal Bayar University, Biology

Prof. Dr. Mehmet ÇEVİK, İzmir Katip Çelebi University, Mechanical Engineering

Prof. Dr. Sezai TAŞKIN, Manisa Celal Bayar University, Electrical and Electronics Engineering

Prof. Dr. Tuğba Özacar ÖZTÜRK, Manisa Celal Bayar University, Computer Engineering

Assoc. Prof. Dr. Mehmet Ali ILGIN, Manisa Celal Bayar University, Industrial Engineering

Assoc. Prof. Dr. Serhat ARAS, University of Health Science, Medical Physics

Assoc. Prof. Dr. Sermin ÇAM KAYNAR, Manisa Celal Bayar University, Physics

International Scientific Advisory Board

Prof. Dr. Arianit REKA; State University of Tetova, Macedonia

Prof. Dr. Tomasz NIEMIEC; Warsaw University of Life Sciences, Poland

Prof. Dr. Alyani ISMAIL; Universiti Putra, Malaysia

Prof. Dr. Iuliana APRODU; Dunarea de Jos University, Romania

Assoc. Prof. Can BAYRAM; University of Illinois, USA

Assoc. Prof. Dr. Johanan Christian PRASANN; Madras Christian College, South India

Assoc. Prof. Dr. Noureddine ISSAOUI; Université de Monastir, Tunisie.

Assoc. Dr. Edward Albert UECKERMANN; North-West University, South Africa

Assoc. Dr. Zhi-Qiang ZHANG; The University of Auckland, Holland

Assist. Prof. Dr. Young Ki KIM; Pohang University of Science and Technology, South Korea

Assist. Prof. Dr. Mona MIRHEYDARI; Rutgers University, USA

Assist. Prof. Dr. Donatella ALBANESE; Università Degli Studi Di Salerno, Italy

Assist. Prof. Dr. Jinghua JIANG; The University of Memphis, USA

Assist. Prof. Dr. Jens OLDELAND; University of Hamburg, Germany

Dr. Cheng CHENG; Apple Inc., USA

Dr. Sajedeh AFGHAH; Microsoft Corporation, USA

Dr. Jinghua JIANG; The University of Memphis

National Scientific Advisory Board

Prof. Dr. Mustafa Ersöz; Selçuk University

Prof. Dr. Oğuz Gürsoy; Mehmet Akif University

Prof. Dr. Mehmet Çevik; İzmir Katip Çelebi University

Prof. Dr. Sezgin Çelik; Yıldız Teknik University

Prof. Dr. Osman Dayan; Çanakkale Onsekiz Mart University

Prof. Dr. Serdar İplikçi; Pamukkale University

Prof. Dr. Yasin Üst; Yıldız Teknik University

Prof. Dr. Mahmut Kuş; Konya Teknik University

Prof. Dr. Ertuğ Gundüz; Hacettepe University

Prof. Dr. Tülin Aydemir; Manisa Celal Bayar University

Prof. Dr. Sezai Taşkın; Manisa Celal Bayar University

Prof. Dr. Fatma Şaşmaz Ören; Manisa Celal Bayar University

Prof. Dr. Fatih Selimefendigil; Manisa Celal Bayar University

Prof. Dr. Osman Çulha; Manisa Celal Bayar University

Prof. Dr. Ali Konuralp; Manisa Celal Bayar University

Prof. Dr. Erol Akpınar; Abant İzzet Baysal University

Prof. Dr. Ali Demir; Manisa Celal Bayar University

Prof. Dr. Serap Derman; Yıldız Teknik University

Prof. Dr. Özlem Çağındı; Manisa Celal Bayar University

Assoc. Prof. Dr. Fatih Doğan; Çanakkale Onsekiz Mart University

Assoc. Prof. Dr. Yeliz Yıldırım; Ege University

Assoc. Prof. Dr. Hayati Mamur; Manisa Celal Bayar University

Assoc. Prof. Dr. Mehmet Söylemez; Adıyaman University

Assoc. Prof. Dr. Nil Mansuroğlu; Ahi Evran University

Assist. Prof. Dr. Zeynep Çipiloğlu Yıldız; Manisa Celal Bayar University



CBU Journal of Science

Celal Bayar University Journal of Science (CBUJOS) covers scientific studies in the fields of Engineering and Science and publishes accounts of original research articles concerned with all aspects of experimental and theoretical studies. CBU Journal of Science is a refereed scientific journal published four times annually (March, June, September and December) by The Graduate School of Manisa Celal Bayar University. CBU Journal of Science considers the original research articles written in English for evaluation.

CBU Journal of Science is indexed by TUBİTAK ULAKBİM TR-DİZİN, and also is included in DOAJ, Cite Factor, Journal TOCS, Advanced Science Index and OAJI databases. Digital Object Identifier (DOI) number will be assigned for all the articles being published in CBU Journal of Science.

Instructions for Authors and Article Template can be found on the page of Celal Bayar University Journal of Science DergiPark (<https://dergipark.org.tr/tr/pub/cbayarfbe>)





Vol: 20, Issue: 2, Year: 2024

Contents

Research Article

Pages

- 1. Prediction Of The Remaining Useful Life Of Lithium-Ion Batteries Based On An Empirical Mode Approach With Artificial Neural Networks** 1-13
DOI: 10.18466/cbayarfbe.1429043
Ozancan Bayrı, Sıtkı Akkaya*
- 2. Comparison of Random Forest, SVR and KNN Based Models in Sea Level Prediction for Erdemli Coast of Mersin** 14-18
DOI: 10.18466/cbayarfbe.1384547
Yavuz Karsavran*
- 3. Microbiological Examination of Washbasin, Faucet Heads and Toilet Door Handles of the Students' Toilets at a State University** 19-27
DOI: 10.18466/cbayarfbe.1432698
Yasemin Keleş Dinç, Sedat Per*
- 4. Detection of Red, Yellow, and Green Lights in Real-Time Traffic Lights with YOLO Architecture** 28-36
DOI: 10.18466/cbayarfbe.1432356
Abdil Karakan*
- 5. An Extended UEHL Distribution: Properties and Applications** 37-44
DOI: 10.18466/cbayarfbe.1435139
Murat Genç*, Ömer Özbilen
- 6. The Impact of Image Reconstruction Parameters on TARE Treatment Dosimetric Calculation** 45-53
DOI: 10.18466/cbayarfbe.1478468
Bilal Kovan*, Emine Göknur Işık
- 7. An Alternative Approach to Find the Position Vector of a General Helix (Scrophulariaceae) and Their Taxonomic Significance** 54-60
DOI: 10.18466/cbayarfbe.1479066
Gizem Güzelkardeşler, Burak Şahiner*
- 8. Influence of Sintering Time on Electrical Properties, Densification, and Microstructure of PMN-PT- PMS Piezoelectric Ceramics** 61-66
DOI: 10.18466/cbayarfbe.1452081
Volkan Kalem*, Osman Düzen
- 9. Comparative Analysis of Alkaline Phosphatase Activity and Aerobic Spore-Forming Bacteria in Pasteurized Milk** 67-71
DOI: 10.18466/cbayarfbe.1475459
Mustafa Oskay*
- 10. Coffee Active Ingredient Loaded Biopolymer Nanoparticles: Synthesis and Characterization** 72-81
DOI: 10.18466/cbayarfbe.1448091
Özge Vardar, Ayça Mehmetoğlu Al, Yeliz Yıldırım*

Prediction Of The Remaining Useful Life Of Lithium-Ion Batteries Based On An Empirical Mode Approach With Artificial Neural Networks

Ozancan Bayrı¹ , Sıtkı Akkaya^{2*} 

¹ Institute Of Graduate Studies Defence Technology Programme, Sivas University of Science and Technology, Sivas, Türkiye

² Department of Electrical and Electronics Engineering, Sivas University of Science and Technology, Sivas, Türkiye
[*sakkaya@sivas.edu.tr](mailto:sakkaya@sivas.edu.tr)

* Orcid No: 0000-0002-3257-7838

Received: 31 January 2024

Accepted: 27 March 2024

DOI: 10.18466/cbayarfbe.1429043

Abstract

Forecasting future capacities and estimating the remaining useful life, while incorporating uncertainty quantification, poses a crucial yet formidable challenge in the realm of battery health diagnosis and management. In this study, a data-driven model based on artificial neural networks (ANN) and signal decomposition techniques including Empirical Mode Decomposition (EMD), Ensemble Empirical Mode Decomposition (EEMD), and Empirical Wavelet Transform (EWT) is presented to predict the capacity value of lithium-ion batteries. Signal decomposition was performed using the discharge voltage values for four different batteries. A total of 22 features were obtained. The features of the signal decomposition methods were evaluated separately as well as hybrid approaches. Mean Squared Error (MSE), Mean Absolute Percentage Error (MAPE) and Root Mean Square Error (RMSE) performance metrics are used in the proposed method and the values obtained are 3.67×10^{-6} , 0.001351 and 0.002311, respectively. According to the findings, the hybrid model proposed demonstrated positive results in terms of accuracy, adaptability, and robustness.

Keywords: Lithium-ion batteries, Signal decomposition, Artificial neural networks, Prediction

1. Introduction

Lithium-ion batteries stand out among the secondary batteries known for their remarkable energy density, and they find widespread application in today's energy storage landscape [1]. Their prominence extends to diverse sectors, including transportation, communication, aviation, and military defense, owing to their advantageous attributes such as lightweight design, robust safety features, and elevated voltage levels in comparison to alternative battery technologies [2]. Notably, as the electric vehicle market continues to expand and the prevalence of mobile phones and personal mobility devices rises, the prudent management of energy resources and the establishment of dependable, enduring battery solutions have assumed heightened significance [3].

Against this backdrop, the imperative to assess battery health becomes paramount. A pivotal threshold in this

evaluation lies in the battery's capacity, where a decline below 80% signifies the completion of its operational lifespan. Critical factors that impinge upon battery longevity encompass charge-discharge cycles, overcharging, discharging under strenuous conditions, and exposure to high currents. Anticipating battery longevity carries profound implications, underpinning efficient resource allocation, stable management practices, and the uninterrupted operation of devices.

Estimation techniques for assessing the Remaining Useful Life (RUL) of lithium-ion batteries can be broadly categorized into model-based, data-driven, and hybrid methods that combine aspects of both. Among the model-based approaches, two prominent methods are the utilization of electrochemical models and equivalent circuit models. However, within the realm of model-based techniques, the challenge lies in acquiring a suitable model that can effectively encapsulate the intricate dynamic behaviors of the system. This challenge arises from the intricate physical and chemical intricacies

inherent to batteries, coupled with the presence of numerous parameters that exert influence upon battery performance parameters such as charge/discharge currents, voltage, temperature, and internal impedance [4].

Forecasting the remaining lifespan of lithium-ion batteries through data-driven techniques proves to be notably more straightforward compared to model-based approaches. This avenue circumvents the necessity for specialized expertise, offering enhanced flexibility and practicality. Within data-driven methodologies, the demand for explicit mathematical formulations to articulate the deterioration trajectory of batteries over time, as seen in model-based methodologies, is obviated. Instead, this approach hinges on the foundation of historical degradation data, harnessing machine learning algorithms like Support Vector Machines (SVM), Logistic Regression, and Artificial Neural Networks (ANN) for prognosticating the RUL of lithium-ion batteries [5]. To illustrate, exemplar studies conducted with data-driven strategies further underscore the viability of this approach.

The data-driven approach disregards the intricacies of the battery's internal reactions and parameters, instead focusing on extracting vital insights from the battery's historical data to assess its capacity degradation pattern [6]. Unlike traditional approaches that rely on specific physical models, data-driven methods leverage extensive historical battery measurement data to construct pertinent models through the use of machine learning techniques. This inherent flexibility and versatility make these methods highly promising for various applications [7]. The crux of data-driven methods lies in the careful selection and processing of data to establish the intricate relationships between parameters and State of Health (SOH). Commonly employed data-driven techniques encompass Neural Networks (NNs) [8], Relevance Vector Machines [9], Autoregressive Moving Average models [10], Support Vector Regression (SVR) [11], and SVM [12]. For instance, Li et al. [13] employed SVR to predict SOH for two batteries under different aging conditions, implementing filtering technology to refine capacity curves and enhance model accuracy. Meanwhile, Fei et al. [14] meticulously crafted six machine learning models to forecast battery life, conducting a thorough comparison of each model's distinctive characteristics. Notably, battery prediction models founded on neural networks have recently garnered increasing interest within the research community.

However, there is room for improvement in current forecasting models. Signal decomposition methods are typically applied in isolation, and the preference for a hybrid approach is underrepresented in the literature. In this paper, we introduce a novel RUL forecasting

approach based on neural networks, which leverages hybrid decomposition methods.

This study introduces a data-driven model that employs artificial neural networks, built upon the foundations of Empirical Mode Decomposition (EMD), Ensemble Empirical Mode Decomposition (EEMD), and Empirical Wavelet Transform (EWT) signal processing techniques. The objective is to anticipate the capacity levels of lithium-ion batteries. The efficacy of this approach was evaluated using a dataset sourced from the NASA Ames Prognostics Center of Excellence (PCoE), focusing on lithium-ion batteries [15]. Contributions of this study are as follows.

- Expanded feature set with 22 features in total obtained from residues of EMD, EEMD, EWT, and different combinations of them.
- Then the hybrid models are composed of Multilayer Perceptron (MLP) and different combinations for different scenarios.
- Performance Comparison for different mentioned hybrid models.
- Performances Comparison for different batteries comparatively.
- The best results in terms of mean values for the EMD-EEMD model
- More effective performance than similar studies

The rest of the paper is organized as follows. Section 2 describes in detail the EMD, EEMD, EWT, and MLP methods used in the proposed hybrid forecasting model. In Section 3, battery capacity forecasting is performed with the proposed hybrid model and the prediction results and model performance are presented. The last section summarizes the results of the study.

2. Materials and Methods

2.1. Dataset

The data for this study originates from the NASA Prognostic Center of Excellence (PCoE). Detail of the data acquisition is given in Table 1 as follows. The raw dataset from NASA has a range of datasets for different battery types with different time ranges. Also, most of the time series (T.S.) capacity signals have some missing data. For these causes, similar to the other studies on lithium-ion batteries, B5, B6, B7, and B18 T.S. capacity signals which are more stable than the others are selected. We employed four distinct sets of NASA Lithium-Ion Batteries denoted as B0005, B0006, B0007, and B0018, each boasting a 2 Ah rated capacity. These batteries underwent a meticulous testing regimen conducted at room temperature. Initially, the charging process involved a constant current of 1.5 A, followed by charging under a constant voltage of 4.2 V. Subsequently, discharging commenced with a consistent 2 A current until the voltage levels for B0005, B0006, B0007, and B0018 reached 2.7 V, 2.5 V, 2.2 V, and 2.5 V,

respectively. The experiment was concluded once the actual battery capacity fell below a predetermined usage threshold [15, 16]. Visualization of the capacity degradation curves for B0005, B0006, B0007, and B0018 is encapsulated in Figure 1.

Table 1. Data Acquisition details

Number of Lithium-ion batteries	18,650
Manufacture	LG Chem
Chemistry	Lithium cobalt
Number of cells	28
Nominal capacity	2.10 Ah
Capacity range	2.10 Ah → 0.80 Ah
Voltage range	4.2–3.2 V
Cycling protocols	7
Sampling Frequency	10 Hz

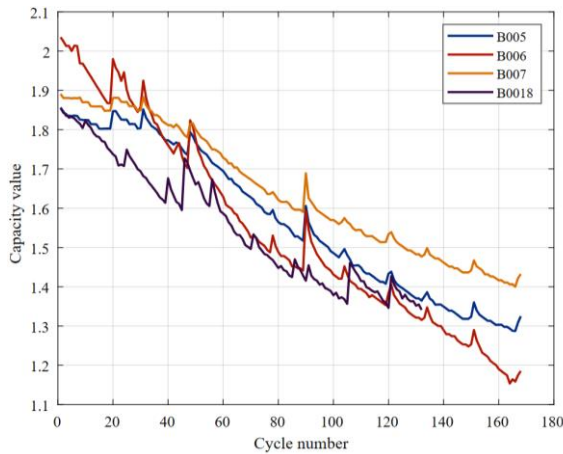


Figure 1. NASA Lithium-ion battery capacity degradation curves

2.2. Data pre-processing

Signal preprocessing refers to an important stage in the analysis of signals, where raw data undergoes a series of computational techniques aimed at improving its quality, extracting relevant features, and reducing unwanted artifacts or noise. This preparatory phase is fundamental in various fields such as signal processing, communications, and data analysis, as it forms the basis for subsequent analytical tasks. Data interpolation is one of the common preprocessing methods. Therefore, the interpolation method is applied to each T. S. signal to equalize each other in each cycle and to analyze with signal processing methods easily.

2.3. Empirical mode decomposition (EMD)

Empirical Mode Decomposition (EMD) stands as a versatile multiresolution technique, purpose-built to

dissect data and unveil its intricate constituents. EMD operates as a powerful tool for scrutinizing non-linear and non-stationary signals, unraveling their complexities by fragmenting them into distinct layers of varying resolutions. The core tenet of EMD involves the meticulous breakdown of temporal sequences into a compact set of intrinsic modes, each accompanied by a residual remainder. These distinctive modes, aptly dubbed Intrinsic Mode Functions (IMFs), encapsulate the essence of the signal's dynamic behavior [17].

The EMD methodology follows a systematic course: initially, it identifies local extrema peppered throughout the temporal sequence. Correspondingly, it constructs upper and lower envelopes, employing interpolation techniques like cubic splines. Subsequently, the average of these envelopes is differentially subtracted from the original signal, birthing a local intrinsic mode function. This twofold process iterates until certain conditions converge:

The mean of the upper and lower envelopes converges toward zero. The count of extremal points and zero crossings diverge by no more than one. This iterative protocol, known as the "elimination" procedure, culminates in the generation of a finite array of IMFs, complemented by a residual component, illustrated in Equation (1):

$$x(t) = \sum_{i=1}^N IMF_i(t) + R_N(t) \quad (1)$$

Where $IMF_i(t)$ represents all potential IMFs, N stands for the count of generated IMFs, and $R_N(t)$ signifies the residual arising from the decomposition.

2.4. Ensemble empirical mode decomposition (EEMD)

The EEMD method is a noise-assisted technique that aims to reduce mode mixing and improve the separation of oscillatory modes. By adding white noise to the input signal, the EEMD algorithm generates a set of IMFs that have statistical properties that are closer to the true intrinsic modes of the signal. The resulting ensemble of IMFs obtained from multiple noise realizations improves the signal-to-noise ratio and helps in the extraction of the underlying signal components [18].

The intricacies of EEMD are outlined in a sequential procedure: the EEMD steps commence with the addition of white noise possessing specific amplitude and frequency attributes to the input signal. Following this, the noisily augmented signal undergoes decomposition through the EMD algorithm, yielding IMFs. EMD, a data-centric methodology, dissects signals into oscillatory IMFs, each characterized by a well-defined frequency range. This process of addition and decomposition is iteratively undertaken numerous times

with distinct noise realizations. Subsequently, the IMFs derived from each iteration are amalgamated and averaged to form an ensemble. This ensemble then undergoes further decomposition via EMD to extract the ultimate IMFs, which faithfully portray the underlying authentic signal. Finally, the residual of the original input signal is computed by subtracting these final IMFs from the initial signal [19].

2.5. Empirical wavelet transform (EWT)

The Empirical Wavelet Transform emerges as a synergy of the wavelet transform and EMD techniques, presenting an instrumental signal decomposition approach that effectively disentangles a provided signal into distinct modes. From a Fourier perspective, this framework aligns with the architecture of a bandpass filter setup, ultimately grounded in the formulation of an adaptive wavelet filter bank [20]. This method achieves its functionality through the creation of adaptive wavelets, dynamically conforming to the informational essence embedded within the signal.

The initial phase of EWT entails an estimation of the signal's frequency components, subsequently leading to the computation of boundaries which, in turn, facilitates the extraction of diverse signal modes based on these determined thresholds. When engaging the EWT method, the initial step involves the reception of signals followed by the computation of the Hurst Exponent value as a measure of long-term memory of time series. Through the application of specified thresholds, signal frequencies are meticulously derived via mathematical computations within the Fourier spectrum, thereby establishing precise boundaries crucial for subsequent phases. With these identified boundaries at hand, the procedure advances to the creation of N wavelet filter banks, followed by the implementation of pertinent mathematical computations employing requisite formulas. This intricate process culminates in the extraction of distinct frequency bands, executed through meticulous filtering mechanisms [21].

Positioned as a swift and incredibly adaptive technique within the realm of signal analysis, the Discrete Wavelet Transform method stands analogous to EWT but boasts a robust and comprehensive mathematical foundation. This mathematical robustness ensures that both the scaling function and wavelets seamlessly conform to the information embedded within the analyzed signal,

obviating the necessity for any a priori knowledge of the signal [22].

2.6. Feature Extraction

Feature extraction involves selecting specific characteristics from a dataset to effectively represent it. This process plays a crucial role in addressing classification and regression challenges. This study focuses on estimating battery capacity by utilizing voltage, current, temperature, and time data, along with attributes derived from various transformation methods. The study employs a total of 22 features, organized into four distinct sets. The first set (attributes 1-10) comprises parameters extracted directly from the dataset without any signal processing. It is shown in Table 2. The remaining sets encompass attributes derived from residual signals resulting from EMD, EEMD, and EWT methods applied sequentially to discharge voltage values.

When using the attributes in the above table, the following mathematical expressions were used.

$$x_{RMS} = \sqrt{\frac{1}{N} \sum_{n=1}^N |x_n|^2} \quad (2)$$

$$x_{average} = \sqrt{\frac{1}{N} \sum_{n=1}^N x_n} \quad (3)$$

2.7. Artificial neural networks

Artificial Neural Networks are one of the most widely used supervised learning methods for regression and classification problems. They are a machine learning approach inspired by biological nervous systems. ANNs are employed for various tasks, such as processing large datasets, recognizing complex patterns, and making predictions. The Multilayer Perceptron (MLP) is a widely preferred type of ANN and consists of three main layers: input, hidden, and output. The input layer contains the attributes necessary to achieve the targeted result. The hidden layer processes the information through neurons, and the output layer predicts continuous values [23]. The architecture used in the study is shown in Figure 2.

Table 2. Created set groups and features.

	Number	Feature Name	Description
Set I	1	MaxVm	Maximum voltage at discharge
	2	MinVm	Minimum voltage
	3	AverageVm	Average voltage
	4	Vtime	Time of occurrence for minimum voltage
	5	MinCurrent	Lowest current value
	6	CurrentTime	Time of occurrence for lowest current
	7	MaxTemperature	Highest temperature
	8	MinTemperature	Lowest temperature
	9	AverageTemperature	Average temperature

	10	TempTime	Time of occurrence for the highest temperature
Set II	11	Max_Vmres_Emd	
	12	Min_Vmres_Emd	
	13	Average_Vmres_Emd	Max, min, average, and RMS values of residue signal obtained by taking EMD components of discharge voltage values
	14	RMS_Vmres_Emd	
Set III	15	Max_Vmres_Eemd	
	16	Min_Vmres_Eemd	
	17	Avarage_Vmres_Eemd	Max, min, average, and RMS values of residue signal obtained by taking EEMD components of discharge voltage values
	18	RMS_Vmres_Eemd	
Set IV	19	Max_Vmres_Ewt	
	20	Min_Vmres_Ewt	
	21	Avarage_Vmres_Ewt	Max, min, average, and RMS values of residue signal obtained by taking EWT components of discharge voltage values
	22	RMS_Vmres_Ewt	

2.7. Artificial neural networks

Artificial Neural Networks are one of the most widely used supervised learning methods for regression and classification problems. They are a machine learning approach inspired by biological nervous systems. ANNs are employed for various tasks, such as processing large datasets, recognizing complex patterns, and making predictions. The Multilayer Perceptron (MLP) is a widely preferred type of ANN and consists of three main layers: input, hidden, and output. The input layer contains the attributes necessary to achieve the targeted result. The hidden layer processes the information through neurons, and the output layer predicts continuous values [23]. The architecture used in the study is shown in Figure 2.

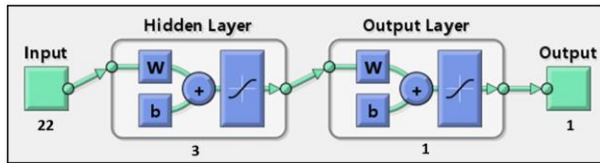


Figure 2. ANN architecture used in the study.

The basic unit of an artificial neural network is called an artificial neural cell or neuron. A neuron receives *input* signals, processes these signals, and produces an *output* signal. The basic mathematical function of a neuron is represented by Equation 4. The connections between neurons are represented by *weights*, and these weights are adjusted during the learning process [24].

$$\begin{aligned} \text{Output} = & \text{Activation function} \\ & \times (\text{weights} \times \text{inputs} \\ & + \text{bias}) \end{aligned} \quad (4)$$

The MLP conducts the learning process by assigning weights to the connections between the layers during training. This is achieved by utilizing the dataset and comparing the network's predictions with the actual results. A loss function quantifies the degree of agreement between the network's predictions and the actual results. The weights are subsequently updated

using a backpropagation algorithm. This iterative process enables the network to improve its predictions [25]. The MLP conducts the learning process by assigning weights to the connections between the layers during training. This is achieved by utilizing the dataset and comparing the network's predictions with the actual results. A loss function quantifies the degree of agreement between the network's predictions and the actual results. The weights are subsequently updated using a backpropagation algorithm. This iterative process enables the network to improve its predictions [25].

2.8. Performance evaluation

In this study similar to other studies on RUL prediction, performance evaluations stemming from capacity value estimations were conducted using widely employed regression metrics: Mean Square Error (*MSE*), Mean Absolute Percentage Error (*MAPE*), and Root Mean Square Error (*RMSE*). The mathematical formulations for these performance metrics are provided below.

$$MSE = \frac{1}{N} \sum_{i=1}^N (y_i - \hat{y}_i)^2 \quad (5)$$

$$MAPE = \frac{1}{N} \sum_{i=1}^N \frac{|y_i - \hat{y}_i|}{y_i} \quad (6)$$

$$RMSE = \sqrt{\sum_{i=1}^N \frac{(y_i - \hat{y}_i)^2}{N}} \quad (7)$$

Where y is the actual battery value, \hat{y} is the prediction value and N is the number of predicted data.

2.9 Proposed methodology

In order to evaluate the efficacy of the proposed hybrid prediction algorithm, a series of methods were implemented. These methods detailed within this paper pertain to forecasting the future capacity of batteries. The precise procedural steps for these methodologies can be found in Figure 3, and they are elaborated upon in the following section.

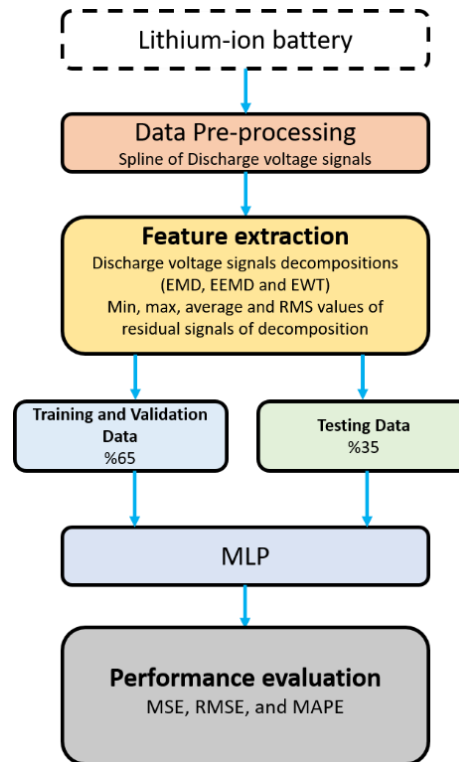


Figure 3. Proposed capacity estimation methodology.

Table 3. Feature sets used in the study.

Scenario number	Methods	Features sets
I	EMD	Set I and Set II
	EEMD	Set I and Set III
	EWT	Set I and Set IV
II	EMD-EEMD	Set I, Set II, and Set III
	EMD-EWT	Set I, Set II, and Set IV
	EEMD-EWT	Set I, Set III, and Set IV
	EMD-EEMD-EWT	Set I, Set II, Set III, and Set IV

In this study, data from NASA's battery database was utilized, specifically focusing on batteries labeled B0005, B0006, B0007, and B0018. The dataset encompasses various parameters in both charge and discharge states, including temperature, current, and voltage values during the discharge phase. To standardize the data before the feature extraction process, the spline command in MATLAB was employed to ensure an equal number of data points for each cycle.

As demonstrated in Table 3, four distinct feature sets were generated using signal processing techniques, including EMD, EEMD, and EWT. The study can be divided into two fundamental sections, each examining distinct strategies.

The common feature set used in both parts of the study is denoted as Set I. In Scenario I, each method is individually analyzed, facilitating a comparative discussion of their performance. Meanwhile, in Scenario II, the study delves into the impact of combining these methods, exploring the performance of a hybrid system encompassing all three approaches.

In the study focused on estimating capacity values, the data were partitioned into two distinct groups: training and test sets. The training dataset comprised roughly the initial 65%, while the test dataset encompassed approximately the remaining 35%. Specifically, for batteries B0005, B0006, and B0007, the initial 110 data points were designated as the training data, while the subsequent 58 data points were allocated to the test set. As for battery B0018, the first 86 data points were assigned to the training set, with the last 46 data points designated for the test set.

In this study, MLPs are utilized to predict battery capacity. The MLP architecture consists of a single hidden layer with 3 neurons. After conducting various tests, it was determined that this architecture produced the best results. The Levenberg-Marquardt algorithm was employed in the training process, as it is commonly used in the literature and is known for its speed compared to other algorithms. The training and test phases were conducted five times, and performance evaluation was based on average values.

Table 4. Options of Proposed MLP Model

Options	Abbreviation in MATLAB	Value
Maximum number of epochs	MaxEpochs	30
Size of mini-batch	MiniBatchSize	128
Option for data shuffling	Shuffle	once
Number of epochs for dropping the learning rate	LearnRateDropPeriod	10
Factor for dropping the learning rate	LearnRateDropFactor	0.1
Contribution of previous step	Momentum	0.9
Decay rate of gradient moving average	GradientDecayFactor	0.9
Denominator offset	Epsilon	1e-8
Maximum number of iterations	MaxIterations	1000
Frequency of neural network validation	ValidationFrequency	50
Factor for L2 regularization	L2Regularization	0.0001
Mode to evaluate statistics in batch normalization layers	BatchNormalizationStatistics	moving
Gradient threshold	GradientThreshold	Inf
Gradient threshold method	GradientThresholdMethod	l2norm
Option to pad or truncate sequences	SequenceLength	longest
Direction of padding or truncation	SequencePaddingDirection	right
Value to pad sequences	SequencePaddingValue	0

The options of the MLP consist of performance to normalization criteria are set as default and details are given in Table 4.

3. Results and discussion

In this section, we present the experimental results for battery test sets B0005, B0006, B0007, and B0018, respectively. The features in Table 2 extracted using EMD, EEMD, and EWT signal decomposition techniques were utilized to predict the capacity values over the battery's lifetime through MLP neural networks. The methodology proposed in Figure 3 was employed, and the performance was assessed using MSE, MAPE, and RMSE metrics. The analysis in this study was conducted using the Matlab programming language.

Analyses were conducted for four different batteries, and the results are depicted in Figures 4-7 and Tables 3-7. Figure 4 and Table 5 display the prediction results for battery B0005. The models were analyzed individually, as well as in their binary and ternary combinations. It can be observed from the figure and the values in the table that all methods yielded results close to the capacity value. When analyzing the methods individually, EEMD produced the best results, while the error values were the

lowest in the EMD-EEMD-EWT combination. Figure 5 and Table 6 display the prediction values for Battery 6. It is evident that the predicted values from the models closely match the actual battery values. Notably, these predictions exhibit a strong alignment with the actual values during the training phase and the initial segments of the test phase; however, they start to diverge noticeably after the 150th data point. In contrast to Battery 5, for this particular battery, the model based on the EEMD method outperformed other single models and binary-ternary combinations. Figure 6 and Table 7 contain the predictions for battery 7. Among the individual models, EWT appears to perform the best, exhibiting the lowest MSE, MAPE, and RMSE values, which signify its accuracy in predicting battery capacity values. When considering binary combinations of models, EMD-EEMD-EWT emerges as the top-performing combination, boasting the lowest MSE, MAPE, and RMSE values among the binary pairs. This suggests that integrating EMD, EEMD, and EWT decomposition techniques into a single model yields the most precise predictions for battery capacity values. Therefore, in the context of this dataset and analysis, the EMD-EEMD-EWT combination model demonstrates superior predictive capabilities compared to the individual models and other binary combinations.

Table 5. Performance evaluations of B0005 battery.

Model	MSE	MAPE	RMSE
EMD	5.29×10^{-6}	0.001434	0.002301
EEMD	3.70×10^{-6}	0.001163	0.001922
EWT	8.48×10^{-6}	0.001810	0.002913
EMD-EEMD	4.83×10^{-6}	0.001346	0.002199
EMD-EWT	8.70×10^{-6}	0.001841	0.002949
EEMD-EWT	7.96×10^{-6}	0.001734	0.002822
EMD-EEMD-EWT	1.35×10^{-6}	0.000703	0.001160

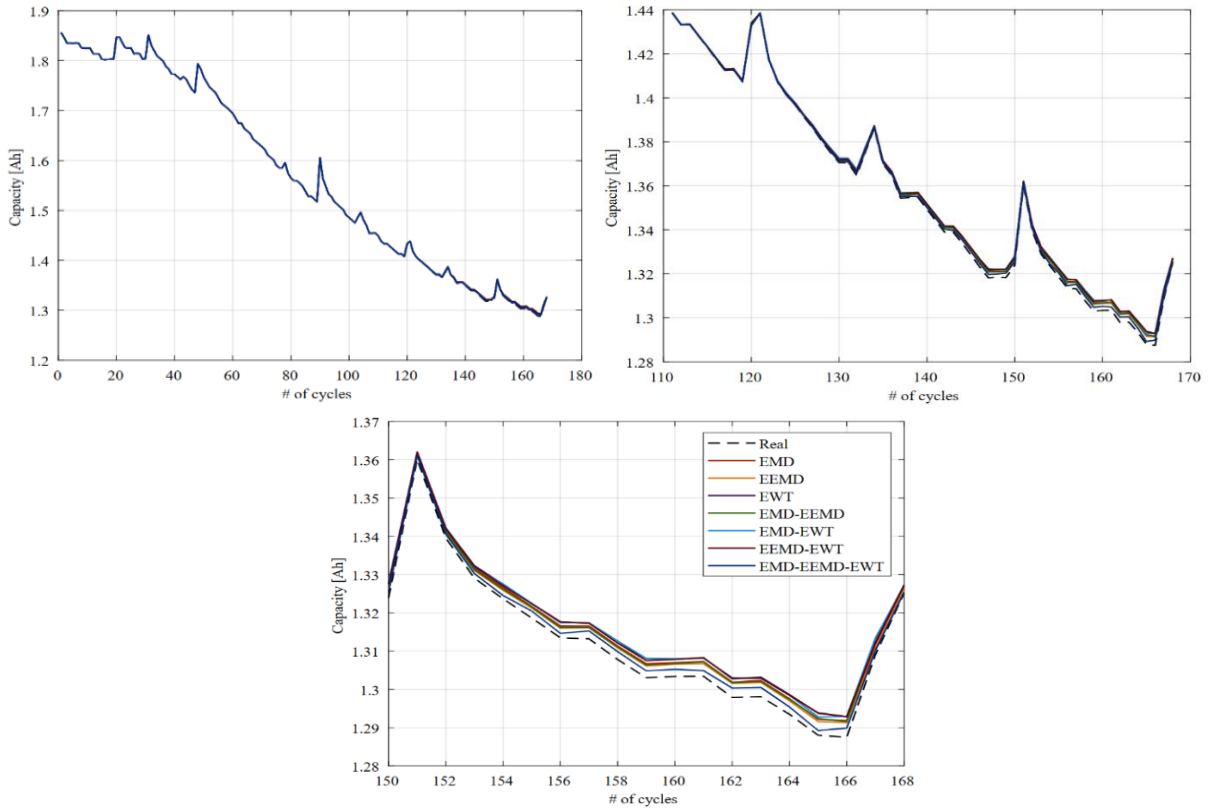


Figure 4. B0005 battery prediction results.

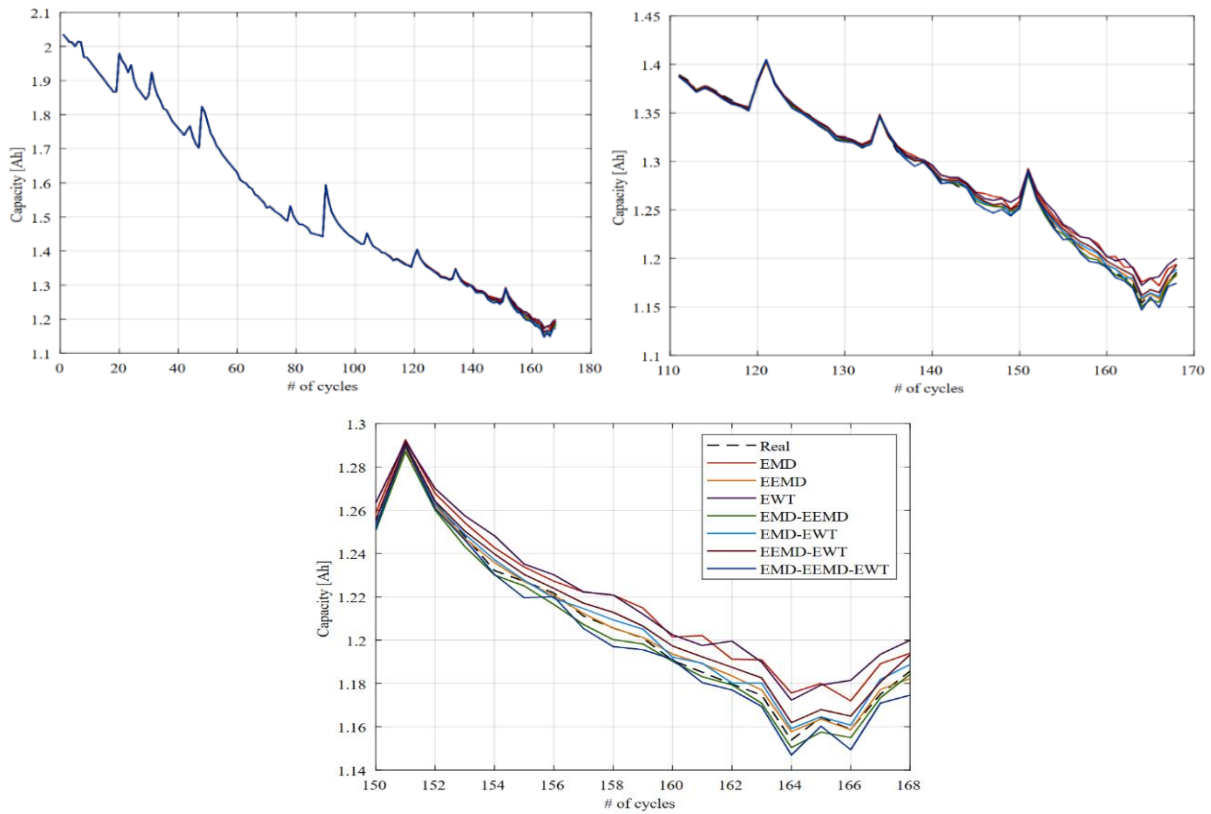


Figure 5. B0006 battery prediction results.

Table 6. Performance evaluations of B0006 battery.

Model	MSE	MAPE	RMSE
EMD	5.96×10^{-5}	0.004619	0.007721
EEMD	4.34×10^{-6}	0.001254	0.002083
EWT	7.31×10^{-5}	0.005011	0.008548
EMD-EEMD	6.41×10^{-6}	0.001646	0.002533
EMD-EWT	6.48×10^{-6}	0.001612	0.002546
EEMD-EWT	1.39×10^{-5}	0.002235	0.003729
EMD-EEMD-EWT	1.63×10^{-5}	0.002574	0.004041

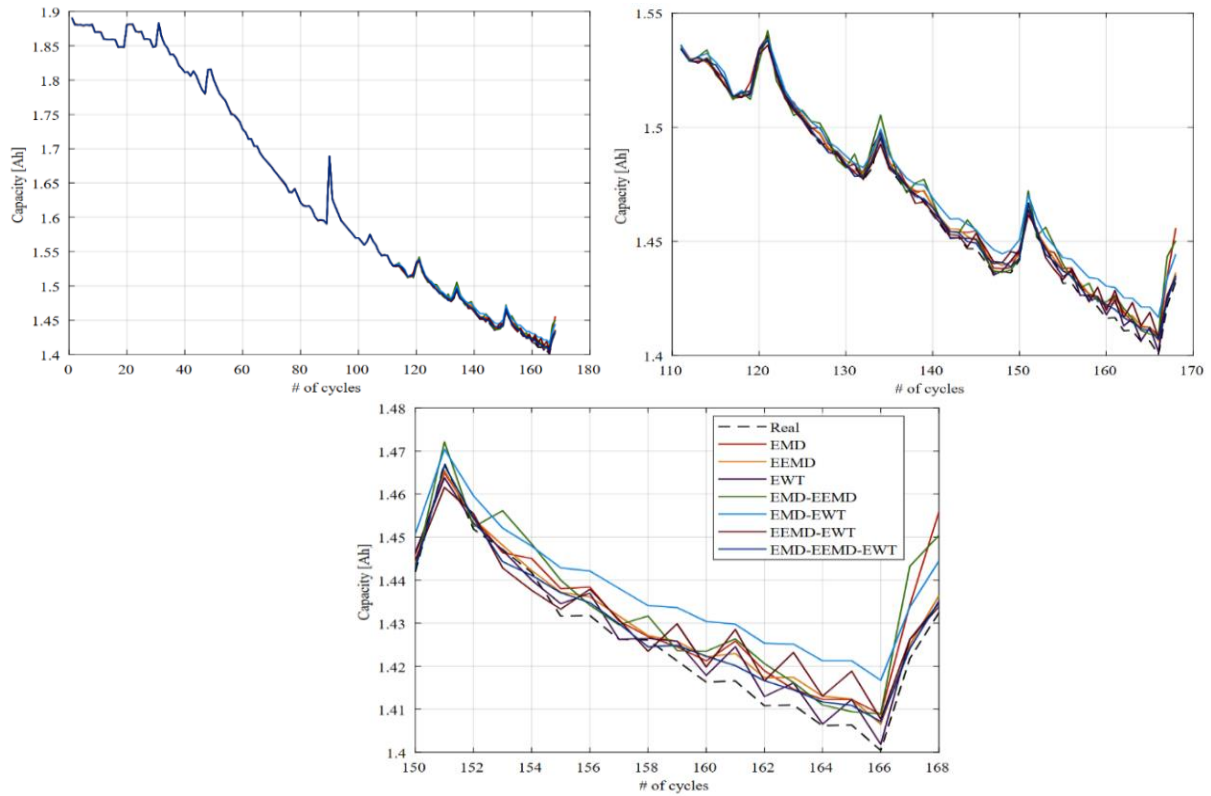


Figure 6. B0007 battery prediction results.

Table 7. Performance evaluations of B0007 battery.

Model	MSE	MAPE	RMSE
EMD	2.72×10^{-5}	0.002539	0.005218
EEMD	1.23×10^{-5}	0.002001	0.003509
EWT	8.47×10^{-6}	0.00133	0.00291
EMD-EEMD	3.94×10^{-5}	0.003155	0.006279
EMD-EWT	6.56×10^{-5}	0.00467	0.008101
EEMD-EWT	2.03×10^{-5}	0.002203	0.004507
EMD-EEMD-EWT	8.29×10^{-6}	0.001666	0.00288

Among the individual models, EMD shines as the standout performer, boasting the lowest MSE, MAPE, and RMSE values, underscoring its remarkable precision in forecasting battery capacity according to Figure 7 and Table 8. When exploring the realm of binary model combinations, EMD-EEMD takes center stage as the top-performing duo, displaying the most favorable MSE, MAPE, and RMSE values among the

binary pairs. This underscores the efficacy of amalgamating EMD and EEMD decomposition techniques into a singular model, yielding the utmost accuracy in predicting battery capacity values. For this battery, the EMD model in isolation and the EMD-EEMD combination model emerge as the optimal choices for predicting battery capacity values, as substantiated by the provided metrics.

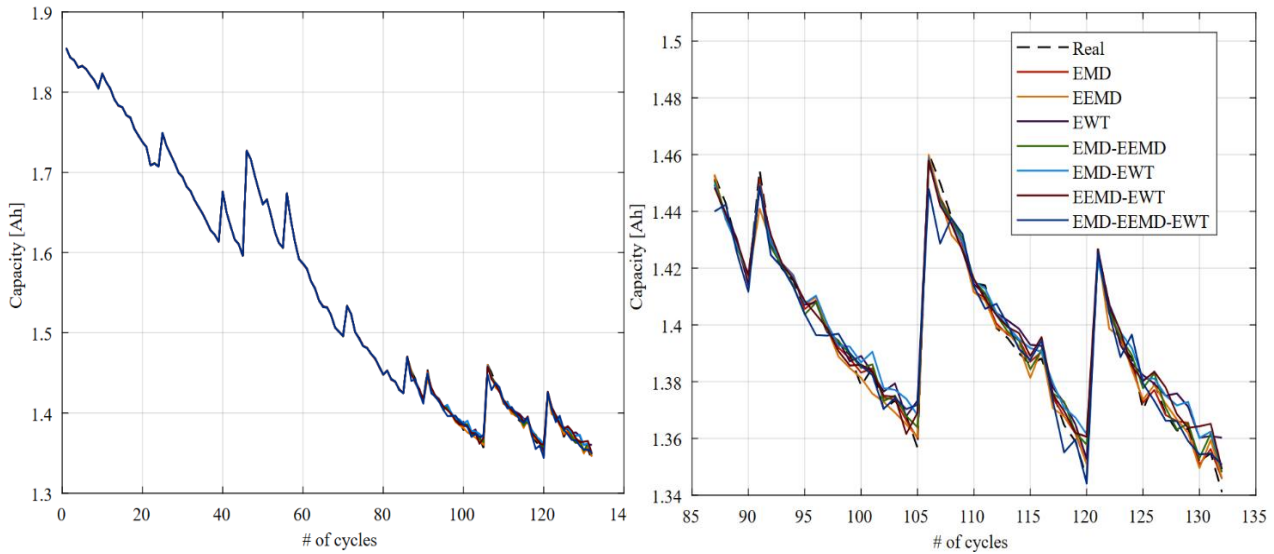


Table 8. Performance evaluations of B0018 battery.

Model	MSE	MAPE	RMSE
EMD	7.15×10^{-6}	1.58E-03	2.67E-03
EEMD	1.78×10^{-5}	0.002442	0.004223
EWT	4.06×10^{-5}	0.00339	0.006369
EMD-EEMD	1.49×10^{-5}	0.002107	0.003864
EMD-EWT	3.34×10^{-5}	0.003411	0.005783
EEMD-EWT	3.30×10^{-5}	0.003307	0.005741
EMD-EEMD-EWT	4.33×10^{-5}	0.003401	0.006581

Table 9 shows the performance metric values of the lithium-ion batteries according to the features obtained from different decomposition models. Lower values of MSE, MAPE, and RMSE indicate better model performance. Among the batteries analyzed, Battery B0005 demonstrates the most favorable results across all three metrics with the EMD-EEMD-EWT model, which boasts the lowest MSE, MAPE, and RMSE values, making it the optimal choice. Battery B0006, on the other hand, showcases distinct performance characteristics. The EEMD model stands out with the lowest MSE and RMSE values, while the EMD-EEMD model achieves the lowest MAPE value. Consequently, both the EMD-EEMD model and the EEMD model exhibit commendable performance across all three

evaluation criteria for Battery B0006. When examining Battery B0007, the EMD-EEMD model emerges as the top performer, displaying the lowest MSE and RMSE values. Meanwhile, the EWT model secures the lowest MAPE value. Notably, both the EMD-EEMD model and the EWT model consistently perform well across all three metrics for Battery B0007. Lastly, for Battery B0018, the EMD-EEMD-EWT model excels, recording the lowest MSE, MAPE, and RMSE values. This establishes it as the preeminent model in this context.

In addition to utilizing various established datasets for validation, we assessed the accuracy of our proposed technique by comparing it to other conventional, model-based, and intelligent approaches, as detailed in Table 10.

Table 9. Performance evaluations of models' mean values.

Model	MSE	MAPE	RMSE
EMD	3.96×10^{-5}	0.002288	0.004815
EEMD	2.42×10^{-5}	0.001965	0.003128
EWT	4.82×10^{-5}	0.003881	0.006438
EMD-EEMD	3.67×10^{-6}	0.001351	0.002311
EMD-EWT	5.53×10^{-6}	0.001741	0.002825
EEMD-EWT	9.37×10^{-6}	0.002620	0.004026
EMD-EEMD-EWT	1.64×10^{-5}	0.002211	0.003756

To ensure a fair and meaningful comparative analysis, we employed the same battery type and NASA datasets. Our comprehensive study considered key factors pertaining to the prediction of RUL for lithium-ion batteries, including input features, capacity, battery type, and error metrics. For example, in the work by Li et al. [26], a Particle Filtering (PF)-based technique for RUL prediction achieved an RMSE of 0.04408. Furthermore, Gao and Huang [12] introduced a hybrid approach using SVM and Particle Swarm Optimization (PSO) for RUL prediction, yielding RMSE values of 0.0213 and 0.0514,

respectively. Additionally, the model developed by Zhou and Huang [24], based on EMD and Auto-Regressive Integrated Moving Average (ARIMA), achieved an RMSE below 1%. In the case of the Relevance Vector Machine (RVM) [27], the relative error remained below 1%. On the contrary, the MLP-based hybrid EMD-EEMD-EWT model, incorporating 22 input parameters, delivered favorable outcomes in terms of accuracy, adaptability, and robustness.

Table 10. Comparison with existing studies.

Reference	Feature parameter	Algorithms	Performance
[26]	Impedance, aging, number of charging cycle	<i>PF</i>	RMSE: 0.2902
[12]	Discharge cycle data	<i>PSO and SVM</i>	MSE: 0.0213
[28]	Voltage, current, temperature, capacity and time	<i>SVM</i>	RMSE: 0.2159, 0.3108
[27]	Capacity	<i>EMD and RVM</i>	MSE: 4.4972×10^{-5} , 1.6437×10^{-5}
[29]	Voltage	<i>FFNN</i>	MAE: 29.4218
[30]	Voltage, current, temperature, capacity	<i>Deep neural network</i>	RMSE: 3.427
[31]	Voltage, current, temperature, capacity	<i>BPNN</i>	RMSE: 0.0819 MSE: 6.7114×10^{-5}
This study	Voltage, current, temperature	<i>EMD, EEMD, EWT, and MLP</i>	MSE: 3.67×10^{-6} MAPE: 0.001351 RMSE: 0.002311

PF: Particle Filtering; **PSO:** Particle Swarm Optimization; **SVM:** Support Vector Machine; **RVM:** Relevance Vector Regression; **FFNN:** Feed Forward Neural Network; **BPNN:** Back Propagation Neural Network.

Considering the B0005 battery analysis results, the best performance values of MSE (1.35×10^{-6}), MAPE (0.000703) and RMSE (0.001160) values belong to the EMD-EEMD-EWT model. Considering the experiments with this model B0005 battery makes it the most suitable choice. Considering the results of the B0006 battery, the EEMD model gave the most successful results with the lowest MSE (4.34×10^{-6}), MAPE (0.001254) and RMSE (0.002083) performance values. When the B0007 Battery was examined, the EMD-EEMD model emerged as the best performing model, showing the lowest MSE (8.29×10^{-6}) and RMSE (0.00288) values, and the EWT model achieved the lowest MAPE (0.00133) value. It does. In particular, both the EMD-EEMD model and the EWT model showed close performance for the B0007 Battery.

Finally, for Battery B0018, the EMD model highlights the lowest MSE (7.15×10^{-6}), MAPE (1.58×10^{-3}) and RMSE (2.67×10^{-6}) values. The EMD model showed the best results for B0018.

It can be seen that different models come to the fore for different battery groups. In this regard, the fact that the data sets of battery groups and especially the voltage values have different values can change the effect on the estimation algorithm and for batteries

It can be thought that it gives different results. For this reason, the error values were compared by taking the average values of the models. The most successful model emerged as the EMD-EEMD model with MSE (3.67×10^{-6}), MAPE (0.001351) and RMSE (0.002311) values.

Moreover, in the performance comparison with the studies in the literature, the proposed method outperforms in terms of the three performance metrics.

Due to the fact that the other studies in the literature utilized a few input and basic regression methods, their performances of them much lesser than ours. On the other hand, the proposed method uses 22 features obtained from different signal processing methods and MLP models.

Moreover, it is considered that the preprocessing composing elimination of misunderstanding samples and interpolation with equal size is effective in this performance.

Contributions of the paper are as follows

- This study proposed a RUL prediction method based on an expanded feature set with 22 features in total obtained from residues of EMD,

EEMD, EWT, and different combinations of them.

- Then the hybrid models are composed of Multilayer Perceptron (MLP) and different combinations for different scenarios.
- Performances of the method are carried out for different mentioned hybrid models.
- Performances of the method are carried out for different batteries comparatively.
- The best results in terms of mean values are obtained for the EMD-EEMD model as given in Table 9 in the paper.
- The results show that the value of this model has a more effective performance than similar studies in the literature like in Table 8.

In addition, the proposed models can be used to estimate the remaining life after pre-processing the data received from different sensors of the batteries that are a part of electric vehicles. However, it is anticipated that the models to be created and their performance may vary depending on the battery characteristics.

4. Conclusion

Given the significant influence of capacity regeneration on the prediction of Remaining Useful Life (RUL) in lithium-ion batteries, we introduce a novel approach to enhance RUL prediction accuracy. Our method combines decomposition techniques with a focus on the capacity regeneration phenomenon. To begin, we employ the Empirical Mode Decomposition (EMD), Ensemble Empirical Mode Decomposition (EEMD), and Empirical Wavelet Transform (EWT) methods to decompose the voltage curve's time series into multiple scales. Subsequently, we build time series prediction models based on Multilayer Perceptron (MLP) neural networks for each of these components. Finally, performance metrics for the models were calculated. While the findings of each method yielded good results, it can be stated that the metric values of the hybrid models used provide even better results.

In future studies, examining the model with the help of features obtained by different signal processing methods like CEEMDAN and machine learning methods like LightGBM, as well as methods based on deep learning like LSTM-based methods, can be explored.

Author's Contributions

Ozancan Bayrı: Data Acquisition, Writing, Software, Signal Processing, and Editing.

Sitki Akkaya: Supervising, Writing, Software, Analysis, Evaluation and Editing.

Ethics

There are no ethical issues after the publication of this manuscript.

References

- [1]. Adnan, M., The Future of Energy Storage: Advancements and Roadmaps for Lithium-Ion Batteries. 2023, MDPI. p. 7457.
- [2]. Fang, H. Challenges with the ultimate energy density with Li-ion batteries. in IOP Conference Series: Earth and Environmental Science. 2021. IOP Publishing.
- [3]. Hanifah, R.A., S.F. Toha, and S. Ahmad, Electric Vehicle Battery Modelling and Performance Comparison in Relation to Range Anxiety. *Procedia Computer Science*, 2015. 76: p. 250-256.
- [4]. Ji, Y., et al., An RUL prediction approach for lithium-ion battery based on SADE-MESN. *Applied Soft Computing*, 2021. 104: p. 107195.
- [5]. Pang, X., et al., A lithium-ion battery RUL prediction method considering the capacity regeneration phenomenon. *Energies*, 2019. 12(12): p. 2247.
- [6]. Deng, Y., et al., Feature parameter extraction and intelligent estimation of the State-of-Health of lithium-ion batteries. *Energy*, 2019. 176: p. 91-102.
- [7]. Dai, H., et al., A Novel Estimation Method for the State of Health of Lithium-Ion Battery Using Prior Knowledge-Based Neural Network and Markov Chain. *IEEE Transactions on Industrial Electronics*, 2019. 66(10): p. 7706-7716.
- [8]. Li, P., et al., State-of-health estimation and remaining useful life prediction for the lithium-ion battery based on a variant long short term memory neural network. *Journal of Power Sources*, 2020. 459: p. 228069.
- [9]. Chang, Y., H. Fang, and Y. Zhang, A new hybrid method for the prediction of the remaining useful life of a lithium-ion battery. *Applied Energy*, 2017. 206: p. 1564-1578.
- [10]. Chen, Z., et al., State of Health Estimation for Lithium-ion Batteries Based on Fusion of Autoregressive Moving Average Model and Elman Neural Network. *IEEE Access*, 2019. 7: p. 102662-102678.
- [11]. Wei, J., G. Dong, and Z. Chen, Remaining Useful Life Prediction and State of Health Diagnosis for Lithium-Ion Batteries Using Particle Filter and Support Vector Regression. *IEEE Transactions on Industrial Electronics*, 2018. 65(7): p. 5634-5643.
- [12]. Gao, D. and M. Huang, Prediction of remaining useful life of lithium-ion battery based on multi-kernel support vector machine with particle swarm optimization. *Journal of Power Electronics*, 2017. 17(5): p. 1288-1297.
- [13]. Li, X., C. Yuan, and Z. Wang, State of health estimation for Li-ion battery via partial incremental capacity analysis based on support vector regression. *Energy*, 2020. 203: p. 117852.
- [14]. Fei, Z., et al., Early prediction of battery lifetime via a machine learning based framework. *Energy*, 2021. 225: p. 120205.
- [15]. Sahaand, B. and K. Goebel, Battery Data Set, NASA ames prognostics data repository. NASA Ames Research Center, 2007.

- [16]. Zhao, L., Y. Wang, and J. Cheng, A Hybrid Method for Remaining Useful Life Estimation of Lithium-Ion Battery with Regeneration Phenomena. *Applied Sciences*, 2019. 9(9): p. 1890.
- [17]. Huang, N.E., et al., The empirical mode decomposition and the Hilbert spectrum for nonlinear and non-stationary time series analysis. *Proceedings of the Royal Society of London. Series A: mathematical, physical and engineering sciences*, 1998. 454(1971): p. 903-995.
- [18]. Wu, Z. and N.E. Huang, Ensemble empirical mode decomposition: a noise-assisted data analysis method. *Advances in adaptive data analysis*, 2009. 1(01): p. 1-41.
- [19]. Torres, M.E., et al. A complete ensemble empirical mode decomposition with adaptive noise. in *2011 IEEE international conference on acoustics, speech and signal processing (ICASSP)*. 2011. IEEE.
- [20]. Gilles, J., Empirical wavelet transform. *IEEE transactions on signal processing*, 2013. 61(16): p. 3999-4010.
- [21]. Liu, W. and W. Chen, Recent advancements in empirical wavelet transform and its applications. *IEEE Access*, 2019. 7: p. 103770-103780.
- [22]. Hu, Y., et al., An enhanced empirical wavelet transform for noisy and non-stationary signal processing. *Digital signal processing*, 2017. 60: p. 220-229.
- [23]. Yegnanarayana, B., *Artificial neural networks*. 2009: PHI Learning Pvt. Ltd.
- [24]. Zou, J., Y. Han, and S.-S. So, Overview of artificial neural networks. *Artificial neural networks: methods and applications*, 2009: p. 14-22.
- [25]. Abraham, A., *Artificial neural networks. Handbook of measuring system design*, 2005.
- [26]. Li, L., et al., Battery Remaining Useful Life Prediction with Inheritance Particle Filtering. *Energies*, 2019. 12(14): p. 2784.
- [27]. Zhang, C., et al., Capacity Prognostics of Lithium-Ion Batteries using EMD Denoising and Multiple Kernel RVM. *IEEE Access*, 2017. 5: p. 12061-12070.
- [28]. Ali, M.U., et al., Online Remaining Useful Life Prediction for Lithium-Ion Batteries Using Partial Discharge Data Features. *Energies*, 2019. 12(22): p. 4366.
- [29]. Wu, J., C. Zhang, and Z. Chen, An online method for lithium-ion battery remaining useful life estimation using importance sampling and neural networks. *Applied Energy*, 2016. 173: p. 134-140.
- [30]. Khumprom, P. and N. Yodo, A Data-Driven Predictive Prognostic Model for Lithium-ion Batteries based on a Deep Learning Algorithm. *Energies*, 2019. 12(4): p. 660.
- [31]. Ansari, S., et al., Multi-Channel Profile Based Artificial Neural Network Approach for Remaining Useful Life Prediction of Electric Vehicle Lithium-Ion Batteries. *Energies*, 2021. 14(22): p. 7521

Comparison of Random Forest, SVR and KNN Based Models in Sea Level Prediction for Erdemli Coast of Mersin

Yavuz Karsavran^{1*} 

¹İstanbul Şişli Vocational School, Architectural Restoration Program, İstanbul, Türkiye

*karsavran@itu.edu.tr

*Orcid No: 0000-0001-5944-0658

Received: 1 November 2023

Accepted: 28 March 2024

DOI: 10.18466/cbayarfbe.1384547

Abstract

Seawater level prediction is very important in terms of future planning of human living conditions, flood prevention and coastal construction. Nevertheless, it is hard to correctly predict the daily future of sea water level because of the atmospheric conditions and effects. Therefore, Random Forest (RF), Support Vector Regression (SVR) and K-Nearest Neighbor (KNN) methods were used for the prediction of seawater level on Erdemli coast of Mersin in this study. In this paper, root mean square error (RMSE) and coefficient of determination (R^2) were applied as model evaluation criteria. In addition, 15-minute sea water level data of Erdemli Station for approximately 18 months were obtained and used as is. The results depict that Random Forest model can predict the seawater level for 1st and 2nd days with R^2 of 0.80, 0.63, respectively, KNN model can predict for 1st and 2nd days with R^2 of 0.80, 0.64, respectively, and SVR model can predict for 1st and 2nd days with R^2 of 0.77, 0.60, respectively.

Keywords: Random Forest, SVR, KNN, sea level prediction, Mersin Erdemli coast, Mediterranean.

1. Introduction

Due to climate change and human endeavors, seawater level around the World has increased significantly in recent years [1-3]. Accurate prediction of sea level circulation is an important phenomenon for coastal areas with increasing population [3-5]. Because, sea level rise destructively influences ecological habitat and social economy of coastal zones [6,7].

There are commonly two approaches to predicting water levels; physically based modeling and machine learning. Unlike physically based models that need various hydrological and geomorphological data, machine learning methods only need historical water level data to predict future vision of water level. This makes machine learning methods more cost-effective and time-efficient than physically based models. For this reason, machine learning methods are widely used in predicting seawater level [8].

Machine learning methods are generally employed in ocean engineering, particularly in predicting sea level change [3,9,10]. Imani et al. [11] predicted Caspian Sea level using satellite altimetry data and they employed SVR and gene expression programming. Kişi et al. [12]

studied on daily water level prediction in Lake Urmia by applying hybrid of SVR and firefly algorithm. KNN was used to develop a model to predict the water level of the river during typhoons [13]. Khaledian et al. [14] estimated the Caspian Sea level using a 34-year water level dataset using SVR and ANN. Altunkaynak and Kartal [15] applied SVR and KNN methods to predict the sea level of the Bosphorus for up to 7 days lead time. Karsavran et al. [16] used SVR to predict seawater level oscillations of the Bosphorus. Sea level circulations of western Peninsular Malaysia were predicted using SVR [17]. Alshouny et al. [18] used both SVR and KNN methods for sea level prediction. Guyennon et al. [19] applied RF to predict the water level of Lake Bracciano. Karsavran [20] applied SVR, ANN and MLR models to forecast the Black Sea coast of Sinop.

As seen above, there are many studies in this field, but there is a lack of research on the future vision of sea water level oscillations on the Mersin Erdemli coast. In addition, comparing the prediction performances of RF, SVR and KNN methods is a new phenomenon on the Mersin coast. I evaluate the future prediction performance based on the performances of these machine learning methods.

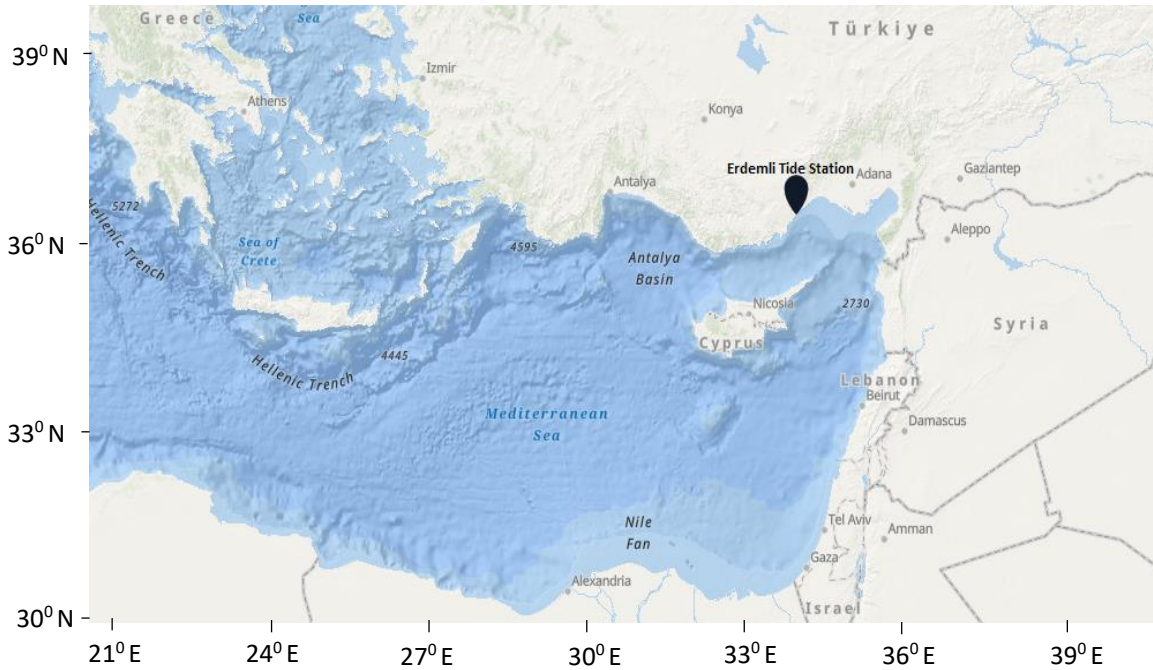


Figure 1. The location of the Erdemli Tide Gauge Station.

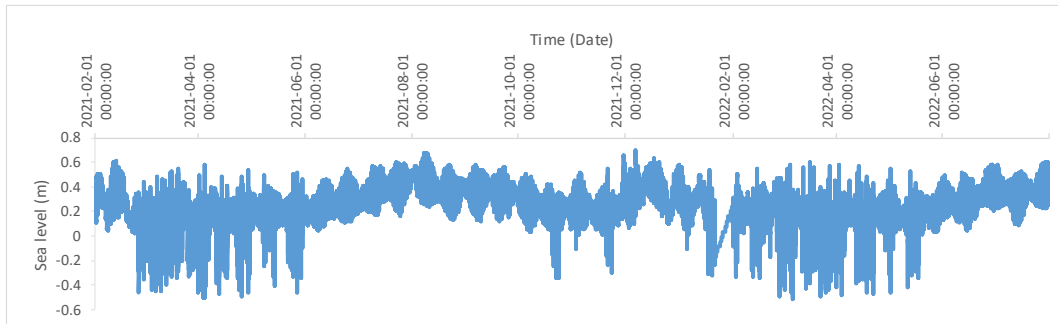


Figure 2. Time series of seawater level in Erdemli station.

2. Materials and Methods

2.1. Data and Study Area

In this study, measurements of the Erdemli tide gauge station (Figure 1), located in the northeast of the Mediterranean, were used. Turkish Sea Level Monitoring System (TUDES, <https://tudes.harita.gov.tr/>) provided sea level data at 15-minute time intervals. Seawater level has been measured at Erdemli Station since May 2003, and 18-month measurements from February 2021 to August 2022 were used in this study (Figure 2). Linear interpolation method was employed to estimate the missing data. In this study, 30% of the total data was used for testing and the remaining 70% was used for training all models [16]. Data separation was done randomly and the same test and training data were used for each model run.

2.2. Methods

2.2.1. Random Forest

Random Forest (RF), one of the ensemble machine learning methods, is a packing (bootstrap collection) model. RF creates multiple regression trees constructed independently using a bootstrap sample of the dataset [19,21,22]. Classification and regression trees (CART) algorithm is used to create decision trees. During creating these decision trees, a wide variety of randomly chosen variables are used by the random subspace method. Accordingly, the best-branched variable in each leaf node is decided by the random sub-space technique. The prediction results are introduced by RF according to the individual results of the decision trees and overall results are adjusted according to the average predictions of the decision trees [23].

2.2.2. Support Vector Regression

SVR is a statistical learning-based neural network used in various engineering regression problems [24]. It has a hyperplane-driven machine learning algorithm to partition data from one dimension into higher dimensional space [18]. SVR solves the regression problems with Equation 2.1:

$$f(x) = \sum_{i=1}^n w_i \phi_i(X) + b \quad (2.1)$$

where w =weight, $\phi_i(X)$ = Kernel function and b =bias. The optimal objective function is shown in Equation 2.2:

$$\min R = \frac{1}{2} w^2 + C \sum_{i=1}^n (\xi_i + \xi_i^*) \quad (2.2)$$

The constraint conditions are depicted in Equation 2.3:

$$\text{Subject_to} \left\{ \begin{array}{l} f(x_i) - y_i \leq \varepsilon + \xi_i \\ y_i - f(x_i) \leq \varepsilon + \xi_i^* \\ \xi_i \geq 0, \xi_i^* \geq 0, i = 1, 2, \dots, n \end{array} \right\} \quad (2.3)$$

where C = cost factor, ε = allowable error, ξ_i and ξ_i^* are relaxation numbers. Both will be greater than zero if there are some prediction errors, otherwise both will be zero [16,25].

2.2.3. K-Nearest Neighbor

K-Nearest Neighbor (KNN) method is one of the most commonly applied method in machine learning studies. The KNN method is a modeling methodology for regression and classification based on the value of the K parameter, which estimates the distance between the sample features. The distance can be estimated applying Euclidean, Minkowski and Manhattan distance equidistant formulas [26]. In addition to being a plain and easy method to put into action, the KNN is also very effective in predicting yield. It requires no assumptions about data distribution. Due to example-based learning algorithm, incremental learning is easily achieved, requiring no training before making predictions. Thus, KNN has commonly been used for various supervised learning tasks [3].

2.2.4. Model Evaluation Criteria

Model performances were acquired from two different numerical error statistics. These are the coefficient of determination (R^2) and the root mean square error (RMSE) depicted in Equation 2.4 and Equation 2.5, respectively.

$$R^2 = \frac{\left[\frac{1}{n} \sum_{i=1}^n (WL_0(i) - WL_0')(WL_f(i) - WL_f') \right]^2}{\sqrt{\frac{1}{n} \sum_{i=1}^n (WL_0(i) - WL_0')^2} \cdot \sqrt{\frac{1}{n} \sum_{i=1}^n (WL_f(i) - WL_f')^2}} \quad (2.4)$$

$$RMSE = \sqrt{\frac{1}{n} \sum_{i=1}^n (WL_f(i) - WL_0(i))^2} \quad (2.5)$$

where $WL_0(i)$ and $WL_f(i)$ are observed and forecasted seawater level, respectively. WL_0' and WL_f' shows their averages, and n is the number of data [27-28].

3. Results and Discussion

In this study, the performances of RF, KNN and SVR for sea level forecast of Mersin Erdemli coast were compared for the next 4 days. First of all, the model input set combination is decided by applying RF. Comparison of input sets for the next day ($t+1$) prediction results of the RF model at Erdemli Station is shown in Table 1.

The input values $WL(t)$ and $WL(t-1)$ increase the value of R^2 to 0.80, while the next three values $WL(t)$, $WL(t-1)$ and $WL(t-2)$ reduce the performance of the RF. As a result, $WL(t)$ and $WL(t-1)$, which produced the highest performance, were used as inputs in all models.

After decision on the input set, seawater level for Erdemli was estimated using the RF model for lead times of 1, 2, 3 and 4 days. Finally, R^2 is 0.80 and 0.63 for lead times of 1 and 2 days, respectively (Table 2).

In the same way, the KNN was applied to estimate seawater level with related lead times [3]. Similar to the RF, the results are 0.80 and 0.64 of R^2 for lead times of 1 and 2 days, respectively (Table 2).

Additionally, the SVR model was used to predict Erdemli's sea water level with specified lead times. In this model, Radial Basis Function (RBF) was applied as the Kernel function and the C parameter of the Kernel is 1000 [16,29]. The best results of SVR model are 0.77 and 0.60 of R^2 for lead times of 1 and 2 days, respectively (Table 2).

The results of the RF, KNN and SVR models show that the RF and KNN models have similar prediction performances, while the SVR model has slightly worse prediction performance than the RF and KNN models. The RF and KNN models have the same performance in seawater level prediction with $R^2=0.80$ and $RMSE=0.07$ for 1-day lead time. Moreover, RF and KNN have similar prediction performances with $R^2=0.63$ and 0.64, respectively, for 2-day lead time. Similarly, the SVR

model provides prediction performance with $R^2=0.77$ and 0.60 for 1 and 2 days of lead time, respectively. However, all model prediction performances decrease significantly at 3 and 4 days lead time (Table 2). Accordingly, RF and KNN models are more ideal than SVR in prediction seawater level in Mersin Erdemli for next 1 and 2 days. However, all models have no ability to accurately predict the seawater level for next 3 and 4 days.

Comparison of the RF, KNN and SVR prediction performances of the water level on the Mersin coast is helpful to choose the accurate method in the machine learning methods for future studies in the Mediterranean. Additionally, this research can be used to create a warning system against sudden increases in water levels in Mersin Erdemli. Long-term projections can also be produced according to the increase in water levels in Mersin coast. The results and the approach

presented and used in this paper can be applied for the analysis of such phenomena.

4. Conclusion

In this article, RF and KNN models achieved higher determination coefficient R^2 in predicting the sea water level at Mersin Erdemli coast for 1 and 2 days lead time, but SVR model gave slightly worse results than RF and KNN. However, the results of all models show that they have no capability to predict seawater level in Mersin Erdemli coast for the 3 and 4 day lead time.

I believe that the results presented here can open new insights in modeling seawater level. Especially, the machine learning methods used in this paper can be applied to the other regions of the Mediterranean coast, including but not limited to Antalya, Hatay and Adana.

Table 1. Model performance of RF for sea level t+1 based on input sets.

Input Set	Output Set	RMSE (m)	R^2
WL(t)	WL(t+1)	0.079	0.75
WL(t)WL(t-1)	WL(t+1)	0.071	0.80
WL(t)WL(t-1)WL(t-2)	WL(t+1)	0.072	0.79
WL(t)WL(t-1)WL(t-2)WL(t-3)	WL(t+1)	0.072	0.79

Table 2. Model performances with respect to lead time prediction WL(t+L)

Inputs (t = day)	Prediction (t = day)	RF		KNN		SVR	
		RMSE (m)	R^2	RMSE (m)	R^2	RMSE (m)	R^2
WL(t)WL(t-1)	WL(t+1)	0.07	0.80	0.07	0.80	0.07	0.77
WL(t)WL(t-1)	WL(t+2)	0.09	0.63	0.09	0.64	0.10	0.60
WL(t)WL(t-1)	WL(t+3)	0.11	0.48	0.11	0.49	0.11	0.45
WL(t)WL(t-1)	WL(t+4)	0.13	0.34	0.13	0.34	0.13	0.31

Acknowledgement

Thanks to Professor Tarkan Erdik for his support in this study. Also, thanks to TUDES for providing the data.

Author's Contributions

Yavuz Karsavran: Drafted and wrote the manuscript, performed the modeling and result analysis.

Ethics

There are no ethical issues after the publication of this manuscript.

References

[1]. Woodworth, PL, Hunter, JR, Marcos, M, Hughes, CW. 2021. Towards reliable global allowances for sea level rise. *Global and Planetary Change*; 203: 103522.

[2]. Yesudian, AN, Dawson, RJ. 2021. Global analysis of sea level rise risk to airports. *Climate Risk Management*; 31: 100266.

[3]. Jin, H, Zhong, R, Liu, M, Ye, C, Chen, X. 2023. Using EEMD mode decomposition in combination with machine learning models to improve the accuracy of monthly sea level predictions in the coastal area of China. *Dynamics of Atmospheres and Oceans*; 102: 101370.

[4]. Primo de Siqueira, BV, Paiva, A de M. 2021. Using neural network to improve sea level prediction along the southeastern Brazilian coast. *Ocean Model*; 168: 101898.

[5]. Zhao, J, Cai, R, Sun, W. 2021. Regional sea level changes prediction integrated with singular spectrum analysis and long-short-term memory network. *Advances in Space Research*; 68: 4534–4543.

[6]. Bernstein, A, Gustafson, MT, Lewis, R. 2019. Disaster on the horizon: The price effect of sea level rise. *Journal of Financial Economics*; 134: 253–272.

[7]. Meilianda, E, Pradhan, B, Comfort, LK, Alfian, D, Juanda, R, Syahreza, S, Munadi, K. 2019. Assessment of post-tsunami disaster land use/land cover change and potential impact of future sea-level

- rise to low-lying coastal areas: A case study of Banda Aceh coast of Indonesia. *International Journal of Disaster Risk Reduction*; 41: 101292.
- [8]. Zakaria, MNA, Ahmed, AN, Malek, MA, Birima, AH, Khan, M MH, Sherif, M, Elshafie, A. 2023. Exploring machine learning algorithms for accurate water level forecasting in Muda river, Malaysia. *Heliyon*; 9(7).
- [9]. Ishida, K, Tsujimoto, G, Ercan, A, Tu, T, Kiyama, M, Amagasaki, M. 2020. Hourly-scale coastal sea level modeling in a changing climate using long short-term memory neural network. *Science of the Total Environment*; 720: 137613.
- [10]. Accarino, G, Chiarelli, M, Fiore, S, Federico, I, Causio, S, Coppini, G, Aloisio, G. 2021. A multi-model architecture based on Long Short-Term Memory neural networks for multi-step sea level forecasting. *Future Generation Computer Systems*; 124: 1–9.
- [11]. Imani M, You RJ, Kuo CY. 2014. Forecasting Caspian Sea level changes using satellite altimetry data (June 1992–December 2013) based on evolutionary support vector regression algorithms and gene expression programming. *Glob Planet Change*; 121:53–63.
- [12]. Kisi O, Shiri J, Karimi S, Shamshirband S, Motamedi S, Petkovi'c D, Hashim R. 2015. A survey of water level fluctuation prediction in Urmia Lake using Support Vector Machine with firefly algorithm. *Appl Math Comput*; 270:731–743.
- [13]. Paul, GC, Senthilkumar, S, Pria, R. 2018. An efficient approach to forecast water levelsowing to the interaction of tide and surge associated with a storm along the coast of Bangladesh. *Ocean Engineering*; 148: 516–529.
- [14]. Khaledian, MR, Isazadeh, M, Biazar, SM, & Pham, QB. 2020. Simulating Caspian Sea surface water level by artificial neural network and support vector machine models. *Acta Geophysica*; 68: 553-563.
- [15]. Altunkaynak A, Kartal E. 2021. Transfer sea level learning in the Bosphorus Strait by wavelet based machine learning methods. *Ocean Engineering*; 233: 109116
- [16]. Karsavran, Y, Erdik, T. 2021. Artificial Intelligence Based Prediction of Seawater Level: A Case Study for Bosphorus Strait. *International Journal of Mathematical, Engineering and Management Sciences*; 6(5): 1242.
- [17]. Balogun, AL, Adebisi, N. 2021. Sea level prediction using ARIMA, SVR and LSTM neural network: assessing the impact of ensemble Ocean-Atmospheric processes on models' accuracy. *Geomatics, Natural Hazards and Risk*; 12(1): 653-674.
- [18]. Alshouny, A, Elnabwy, MT, Kaloop, MR, Baik, A, Miky, Y. 2022. An integrated framework for improving sea level variation prediction based on the integration Wavelet-Artificial Intelligence approaches. *Environmental Modelling & Software*; 152: 105399.
- [19]. Guyennon, N, Salerno, F, Rossi, D, Rainaldi, M, Calizza, E, Romano, E. 2021. Climate change and water abstraction impacts on the long-term variability of water levels in Lake Bracciano (Central Italy): A Random Forest approach. *Journal of Hydrology: Regional Studies*; 37: 100880.
- [20]. Karsavran, Y. 2024. Comparison of ANN and SVR based models in sea level prediction for the Black Sea coast of Sinop. *Turkish Journal of Maritime and Marine Sciences*; 1-8.
- [21]. Liaw, A, Wiener, M. 2002. Classification and regression by random Forest. *R news*; 2 (3): 18–22.
- [22]. Loh, WY. 2011. Classification and regression trees. *Wiley Interdisciplinary Reviews: Data Mining and Knowledge Discovery*; 1 (1): 14–23.
- [23]. Başakın, EE, Ekmekcioğlu, Ö, Özger, M. 2023. Developing a novel approach for missing data imputation of solar radiation: A hybrid differential evolution algorithm based eXtreme gradient boosting model. *Energy Conversion and Management*; 280: 116780.
- [24]. Patil, SG, Mandal, S, Hegde, AV. 2012. Genetic algorithm based support vector machine regression in predicting wave transmission of horizontally interlaced multilayer moored floating pipe breakwater. *Advances in Engineering Software*; 45: 203–212.
- [25]. Lin, GQ, Li, LL, Tseng, ML, Liu, HM, Yuan, DD, Tan, RR. 2020. An improved moth-flame optimization algorithm for support vector machine prediction of photovoltaic power generation. *Journal of Cleaner Production*; 253: 119966.
- [26]. Li, G, Liu, F, Yang, H. 2022. Research on feature extraction method of ship radiated noise with K-nearest neighbor mutual information variational mode decomposition, neural network estimation time entropy and self-organizing map neural network. *Measurement*; 199: 111446.
- [27]. Mehr AD, Kahya E, Olyae E. 2013. Streamflow prediction using linear genetic programming in comparison with a neuro-wavelet technique. *J Hydrology*; 505: 240–249.
- [28]. Karsavran, Y, Erdik, T, & Ozger, M. 2023. An improved technique for streamflow forecasting between Turkish straits. *Acta Geophysica*; 1-12.
- [29]. Wang, WC, Chau, KW, Cheng, CT, Qiu, L. 2009. A comparison of performance of several artificial intelligence methods for forecasting monthly discharge time series. *Journal of Hydrology*; 374(3-4): 294-306.

Microbiological Examination of Washbasin, Faucet Heads and Toilet Door Handles of the Students' Toilets at a State University

Yasemin Keleş Dinç¹ , Sedat Per^{2*} 

¹ Yozgat City Hospital, Türkiye

² Department of Chemistry and Chemical Processing Technologies, Mustafa Çıkrıkçıoğlu Vocational School, Kayseri University, Türkiye

*sedatper@kayseri.edu.tr

*Orcid No: 0000-0002-6131-3321

Received: 6 February 2024

Accepted: 6 April 2024

DOI: 10.18466/cbayarfbe.1432698

Abstract

This study, it was aimed to determine the presence of pathogenic bacteria in the sinks, faucets, and door handles of the toilets actively used by boys and girls in nine faculties located on Yozgat Bozok University Erdoğan Akdağ campus. 54 swab samples were taken from the sinks, faucets, and door handles of toilets, which have the largest share of the main sources of bacteria transmission, between April and June 2019. Each swab sample brought to the laboratory via a cold chain was inoculated separately on 5% sheep blood agar, EMB agar and Mac Conkey agar. In 34 (62.96%) of the swab samples taken, a total of 49 pathogenic bacteria were detected, growing singly or in multiples. Of the 49 bacteria detected, 15 were (30.6%) *Escherichia coli*, 12 were (24.5%) *Staphylococcus aureus*, nine were (18.3%) *Klebsiella spp.*, six were (12.3%) *Pseudomonas spp.*, five were (10.2%) *Proteus spp.* and two were (4.1%) *Enterococcus spp.*

Keywords: Contamination, Hygiene, Pathogenic bacteria, School toilet

1. Introduction

Education, which focuses on the upbringing of the individual, includes formal and informal learning that has been going on since primitive societies. While the family and the environment are influential in the upbringing of the individual in an unofficial sense; Schools have assumed this role in an official sense.¹ Schools, which have an important place in human life, are places where individuals between the ages of 6-and 24 spend most of their time. School-age individuals are more sensitive to physical, biological, and social environmental conditions than adults and are significantly affected by changes in the environment. Therefore, a healthy school environment is necessary for healthy students.²

Hygiene is defined as all the practices made to prevent, maintain, and improve human health factors. Hygiene covers all human activities from the moment of fertilization to death and because it has a wide range of actions, it can be divided into sub-units as an individual, public, and social hygiene. Also, hygiene always has a common purpose: protection, maintenance, and promotion of health. Personal hygiene is a branch of

hygiene that deals with the factors affecting the individual's health and formulates the principles that the individual will apply to protect, maintain, and improve health.³

Hands play an important role in healthcare institutions, industrial settings such as the food industry, as well as in all community and home settings in the transmission of infection. However handwashing has been seen as a measure of personal hygiene for centuries, the specific link between handwashing and the spread of infectious diseases has emerged over the past 200 years.

The microbial population of the skin is divided into resident microbiota and transient microbiota. The resident microbiota is associated with the deeper layers of the skin, such as the sebaceous glands. Temporary microbiota colonizes the superficial layers of the skin and is less adherent. Also, they are more easily removed by hand washing and can be transferred by direct hand contact between human skin and the inanimate environment such as work surfaces or food.⁴

Microorganisms are the oldest living things on earth, due to their ability to adapt quickly to changing living

conditions. Thanks to these abilities, bacteria can find a way to escape from every new antibiotic developed against them.⁵ Bacteria were first observed in 1676 by Antonie van Leeuwenhoek with a single-lens microscope he had designed and built. Leeuwenhoek named the creatures he observed "animalcules". The word "bacterium" was used for the first time in 1838 by Christian Gottfried Ehrenberg and later it was used in the scientific world. The word "bacterium" is originally derived is derived from the Greek word bacterion, meaning "small staff."⁶

Although there are similar studies in other countries in the literature, the fact that it was conducted in universities for the first time in our country makes the study valuable.⁷⁻¹⁵ In this study, the presence of pathogenic bacteria in the sinks, tap heads, and door handles of the toilets are actively used by female and male students in nine faculties located on the Erdoğan Akdağ campus of Yozgat Bozok University was investigated.

2. Materials and Methods

The study examined swab samples taken from the toilet door handles, faucet heads, and washbasin of the toilets belonging to 9 different faculties during the education period (in the Figure that will cover the months of April, May, June) on the campus. A total of 54 swab samples were taken by taking three samples from each of the male and female student toilets, which are actively used in the faculties. The samples taken were transported to the laboratory at the cold chain for cultivation (considering the season in which the samples were collected, they were transported in a bag containing ice wrapped in gauze without contacting the battery in order to protect the characteristics of the medium and the presence of bacteria).

2.1. Cultivation of Specimens

Each swab sample was cultivated separately on 5% sheep blood agar, EMB agar, and MacConkey agar. The media were incubated at 37°C for 36-48 hours. At the end of the incubation, non-growth media were noted. To colonies with multiple growths on 5% sheep blood agar were applied Gram staining. After that gram-negative colonies were passaged on EMB and MacConkey agar. In addition, were passaged again to obtain pure colonies from the mixed growing colonies on EMB and MacConkey agar. The media taken into the passage were again incubated at 37°C for 36-48 hours.

2.2. Macroscopic Examination

Grown on EMB, Macconkey agar, and 5% sheep blood agar and macroscopic appearance of bacteria with characteristic morphology were used.

2.3. Gram Staining

Colonies spread on the slide were dried and fixed, and crystal violet dye solution was dropped on it and waited for one minute. After the preparations were washed with distilled water, Lugol was dripped and waited for one minute. It was washed with distilled water again, 95% ethanol was dropped and waited for 10-15 seconds, then washed with distilled water and covered with aqueous fuchsin and waited for 30 seconds. After washing with distilled water, air-dried preparations were examined under a light microscope with oil immersion.

2.4. Catalase Test

Catalase activities of all bacterial colonies that fell pure after the passage process was performed with hydrogen peroxide (H₂O₂). Colonies that formed gas by releasing O₂ when the colony was mixed with the catalase reagent dripped on the slide were evaluated as catalase positive.

2.5. Coagulase Test

The pure colony grown in the medium was suspended in the tube containing 0.5 ml of blood plasma. Tubes with plasma were incubated at 37°C. The tubes were evaluated for the presence of fibrin at the 4th hours, 8th hours, and 24th hours. Tubes with full clotting in the 4th hour were evaluated as positive results. Tubes without complete fibrin formation were allowed to incubate again. At the end of the incubation, the coagulase test of tubes with coagulation plasma was evaluated as positive, and the homogeneous liquid plasmas coagulase test was evaluated as negative.

2.6. Oxidase Test

For the oxidase test, the colony was rubbed into blotting paper and oxidase solution was dripped onto it. After 30-60 seconds, the formation of violet-purple color on the colony applied area was evaluated as oxidase-positive.

2.7. PYR (Pyrrolidonyl Arylamidase) Test

One drop of distilled water was dropped on the sticks that came out of the PYR test kit, and it was waited for 30 seconds for the stick to absorb the water evenly, and then the colony was applied to the place where the distilled water was dripped. The PYR solution included in the kit was dripped onto the colony. After 40-50 seconds, the formation of a pink-fuchsia color on the colony applied area was considered as a positive result.

2.8. TSI Agar (Triple Sugar Iron Agar) Test

Bacteria determined to be gram-negative as a result of gram staining were inoculated into a TSI medium and incubated at 37°C for 16-18 hours. Blackening in the

medium was evaluated as H₂S positive. The gas formation seen with the disintegration of the medium was evaluated. In addition, the bottom of the medium turning from red to yellow was evaluated as the presence of bacteria that use glucose. The presence of bacteria that use lactose when the slanted part turned from red to yellow was evaluated as positive and the absence of color change was evaluated as negative.

2.9. Urea Test

Bacteria determined to be gram-negative as a result of gram staining were inoculated into a urea medium and incubated at 37°C for 16-18 hours. The fuchsia-pink color formed in the medium at the end of the incubation was evaluated as the presence of bacteria that use urea.

2.10. Citrate Test

Bacteria determined to be gram-negative as a result of gram staining were inoculated into a citrate medium and incubated at 37°C for 16-18 hours. The color change from green to blue that occurred in the medium at the end of incubation was evaluated as the presence of bacteria that use citrate.

2.11. Motility Test

The colony which was taken with the help of a loop into the movement medium was cultured perpendicularly and incubated at 37°C for 16-18 hours. The spread of growth towards the periphery of the culture area after incubation was evaluated as positive motility of the cultured bacteria.

2.12. Indole (Tryptophan) Test

Bacteria determined to be gram-negative as a result of gram staining were inoculated into liquid media and incubated at 37°C for 16-18 hours. After incubation, 3-4 drops of Kovac's reagent were dropped into a liquid indole medium. After 4-5 seconds, the red ring formed on the liquid media was evaluated as the indole test was positive.

3. Results and Discussion

No growth was observed in 20 of the 54 swab samples examined. In the remaining 34 swab samples, a total of 49 bacteria were detected, 21 of which were single and 13 were multiple growths. A total of 15 (30.6%) *E. coli* bacteria were detected, 8 (53.33%) single and 7 (46.67%) multiples. A total of 12 (24.5%) *S. aureus* bacteria were detected, 6 (50%) single and 6 (50%) multiples. A total of 9 (18.3%) *Klebsiella spp.* bacteria were detected, 2 (22.22%) single and 7 (77.78%) multiples. A total of 6 (12.3%) *Pseudomonas spp.* bacteria were detected, 2 (33.33%) single and 4 (66.67%) multiples. A total of 5 (10.2%) *Proteus spp.* bacteria were detected, 1 (20%) single and 4 (80%) multiples. Finally, 2 (100%) single

(4.1%) *Enterococcus spp.* bacteria were detected (Figure 1-5).

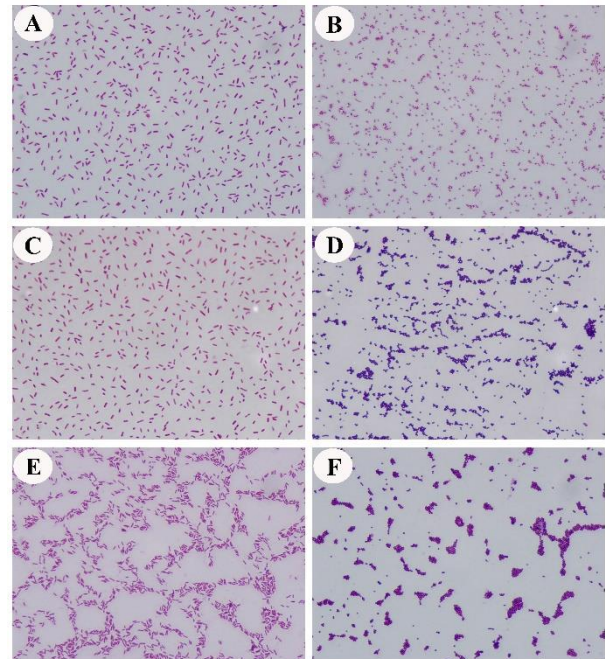


Figure 1. Microscope images A) *Escherichia coli*, B) *Proteus spp.*, C) *Klebsiella spp.*, D) *Enterococcus spp.*, E) *Pseudomonas spp.*, F) *Staphylococcus aureus*.

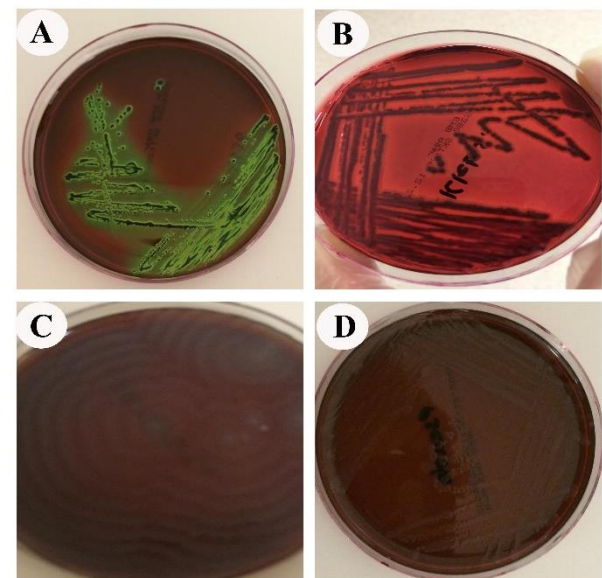


Figure 2. Images on Eosin Methylene Blue agar A) *Escherichia coli* B) *Klebsiella spp.*, C) *Proteus spp.*, D) *Pseudomonas spp.*.

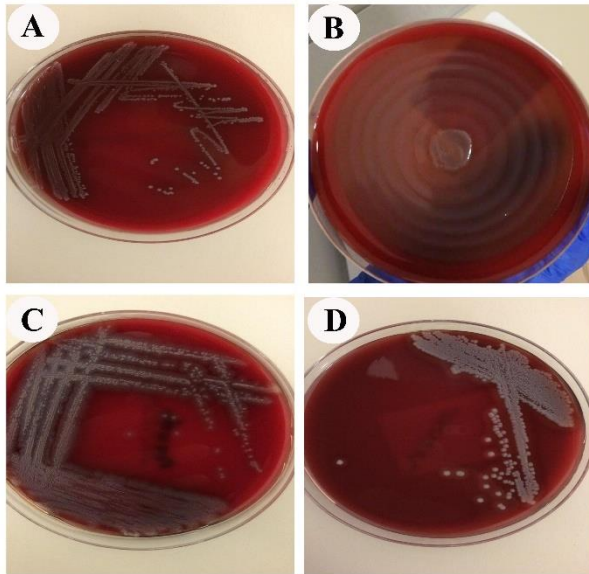


Figure 3. Images on blood agar **A)** *Enterococcus* spp., **B)** *Proteus* spp., **C)** *Pseudomonas* spp., **D)** *Staphylococcus aureus*.

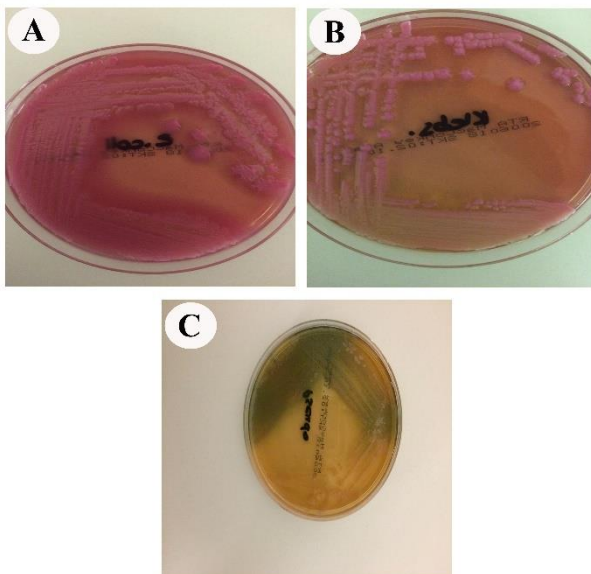


Figure 4. Images on Mac Conkey agar **A)** *Escherichia coli*, **B)** *Klebsiella* spp., **C)** *Pseudomonas* spp..

Staphylococcus aureus was reported to be the most common organism in a study conducted by taking swab samples from 200 door handles in two universities (Khartoum University, Sudan University of Science and Technology, and Al Neelain University) in the state of Khartoum in Sudan.¹⁵

Alonge et al. (2019) in their study, in which they conducted a microbiological scan of the door handles of 12 toilets in the Abuja campus of Baze University of Nigeria, stated that there was general contamination by seven bacterial species. (*Staphylococcus aureus* 2.9%;

Salmonella typhimurium 21.4%; *Escherichia coli* 14.3%; *Pseudomonas aeruginosa* 9.5%; *Proteus mirabilis* 4.8%; *Klebsiella oxytoca* 4.8%; *Klebsiella pneumoniae* 2.3%).¹⁶ In the study in which the water flowing from the sinks in some schools in Erzurum (Turkey) city center and the swab samples taken from faucet heads of the toilets were examined microbiologically, bacteria were detected in 136 (90.7%) of the 150. The isolated bacteria were *Escherichia coli* in 54 samples (36%), and *Staphylococcus aureus* in 52 (34.6%) of the swab samples. Total coliform bacteria and fecal coliform bacteria were not found in any of the water samples examined.¹⁷

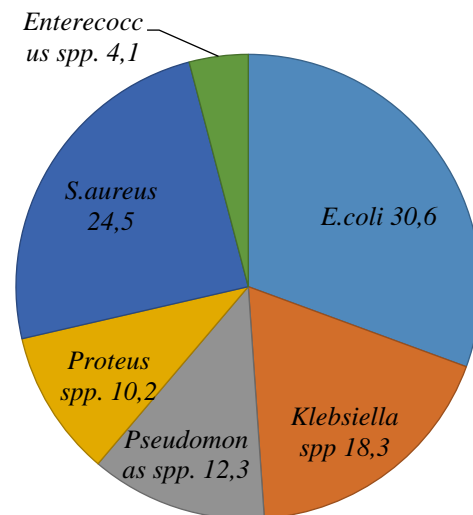


Figure 5. The growth results of pathogenic bacteria on washbasin, faucet heads and toilet door handles.

Approximately 10 surfaces were sampled from each of the 12 public toilets and 19 bacterial phyla were identified using high-throughput barcoded pyrosequencing of 16 S rRNA genes. Most sequences belonged to four phyla: *Actinobacteria*, *Bacteroidetes*, *Firmicutes* and *Proteobacteria*.¹⁸

It was determined that, except for one of the toilets used by the students in the faculties (Faculty of Engineering and Architecture, men's toilet), foaming hand soap was found in the rest. It was determined that the availability of toilet paper varies according to faculties (Table 1). A total of 26 (53.1%) of the toilets used by female students and 23 (46.9%) of the toilets used by male students were found to have bacterial growth.

Table 1. Availability of soap and toilet paper in faculty toilets.

Faculty names	Gender	Soap	Toilet paper
Faculty of Medicine	F	+	+
	M	+	-
Faculty of Engineering and Architecture	F	+	+
	M	-	-
Faculty of Health Sciences	F	+	-
	M	+	+
Faculty of Theology	F	+	-
	M	+	+
Faculty of Agriculture	F	+	+
	M	+	-
Faculty of Education	F	+	+
	M	+	+
Faculty of Economics and Administrative Sciences	F	+	-
	M	+	-
Faculty of Communication	F	+	-
	M	+	-
Faculty of Art and Sciences	F	+	-
	M	+	+

Percentage distribution of bacteria detected from toilets used by female students; *E. coli* 38.5%, *S. aureus* 19.2%, *Klebsiella spp.* 15.4%, *Pseudomonas spp.* 11.5%, *Proteus spp.* 11.5%, *Enterococcus spp.* 3.9% (Figure 6).

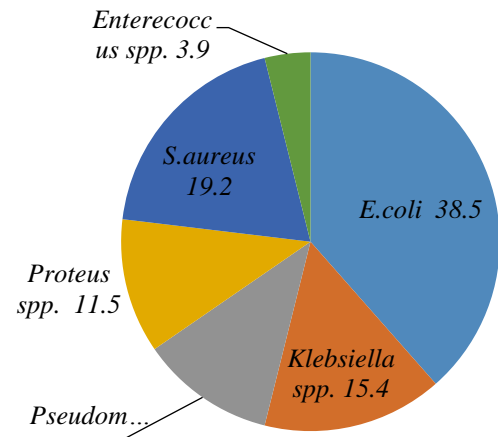


Figure 6. The growth results of pathogenic bacteria on washbasin, faucet heads and toilet door handles used by female students.

Percentage distribution of bacteria detected from toilets used by male students; 30.4% *S. aureus*, 21.7% *E. coli*, 21.7% *Klebsiella spp.*, 13.1% *Pseudomonas spp.*, 8.8% *Proteus spp.*, 4.3% *Enterococcus spp.* (Figure 7).

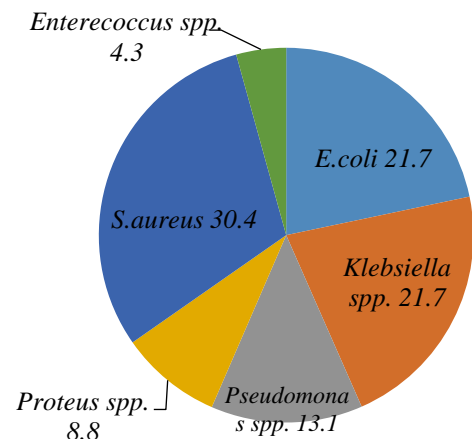


Figure 7. The growth results of pathogenic bacteria on washbasin, faucet heads and toilet door handles used by male students



Table 2. According to faculties, the distribution of pathogenic bacteria growth on the washbasin, faucet heads, and toilet door handles..

Faculty names	Gender	W	FH	TDH	W	FH	TDH	W	FH	TDH	W	FH	TDH	W	FH	TDH	W	FH	TDH
Faculty of Medicine	F				+										+				
	M					+			+						+				
Faculty of Engineering and Architecture	F							+											+
	M					+	+		+			+				+			
Faculty of Health Sciences	F		+	+								+	+						
	M		+					+						+					
Faculty of Theology	F		+	+	+			+			+								
	M	+																	+
Faculty of Agriculture	F	+																	
	M	+					+									+			
Faculty of Education	F						+									+			
	M												+			+			
Faculty of Economics and Administrative Sciences	F		+													+			
	M		+				+										+		
Faculty of Communication	F	+		+	+														
	M	+														+			
Faculty of Art and Sciences	F	+	+					+						+		+			
	M																		
		<i>E. coli</i>			<i>Klebsiella spp.</i>			<i>Pseudomonas spp.</i>			<i>Proteus spp.</i>			<i>S. aureus</i>			<i>Enterococcus spp.</i>		

*W: Washbasin FH: Faucet heads TDH: Toilet door handles

The material with the highest growth was the faucet heads with 21 (42.9%) bacterial growth. In total, 21 (42.9%) of 49 bacteria were found at the faucet heads, 15 (30.6%) in the washbasins, and 13 (26.5%) on toilet door handles (Figure 8-10). Scott et al., (1892) were examined the kitchens, toilets, and bathrooms of more than 200 homes to determine the occurrence and contamination levels of potential pathogens and were found high numbers to be mostly in wet areas associated with bathrooms, bathtubs, washbasin, washing machines, and diaper pails.¹⁹

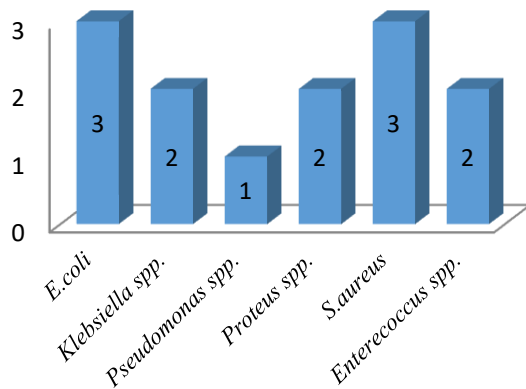


Figure 8. The growth results of pathogenic bacteria on toilet door handles

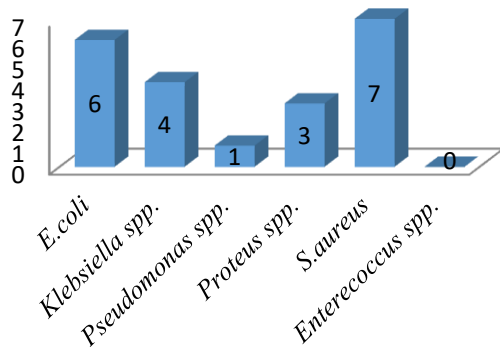


Figure 9. The growth results of pathogenic bacteria on faucet heads

In a study in Kathmandu (Nepal), one hundred and ninety swab samples were collected from five household toilets and total coliform and *Escherichia coli* concentrations were measured using membrane filtration methods. The faucet, spray arm, or bucket used for anal cleaning, where toilet stones have the highest median bacterial concentrations (mean total coliform = 214 / cm² and mean *E. coli* = 56 / cm²), have the highest median bacterial contamination in household (mean total

coliform = 56 / cm²) = 1/cm² and mean *E. coli* = 0.4/cm²).²⁰

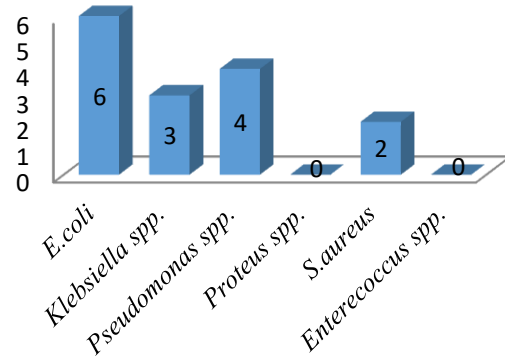


Figure 10. The growth results of pathogenic bacteria on washbasin

Here, *E. coli*, which was 10 out of a total of 26 bacteria grown in the girls' toilet, and *S. aureus*, which was 7 (30.4%) of the 23 bacteria that grew in the boys' toilet, were determined as the dominant bacteria. In our study, *E. coli* 15 (30.6%) was the most encountered bacteria. In addition, the bacteria detected from the targeted places of the faculties are given in Table 2. Microbial contamination research was carried out on 7,482 samples collected in public toilets in Tehran, the capital of Iran. The data were obtained by analyzing the inner and outer door handles of 804 toilets, 1062 faucet heads, 826 sink faucets, 1,062 toilet hoses, 804 flush handles, 643 soap dispenser bases, 643 liquid soaps, 99 bar soap, 169 toilet paper, 50 hand dryers. It was determined that 89.25% (6678 samples) of the samples were contaminated and 10.75% (804 samples) were not contaminated. In the study, it was reported that *Escherichia coli* with 28.48% and *Pseudomonas* species with 0.39% were the most common bacteria, respectively.²¹

Samples were taken from frequently touched surfaces in Mecca, Mina, Arafat, and Medina to detect the presence of respiratory bacteria and viruses during Hajj (in 2016 and 2018). 70/142 (49.3%) environmental samples collected were determined to be positive for at least one respiratory pathogen. Among the positive samples, the most frequently tested positive bacteria was *Klebsiella pneumoniae* (57.1%), followed by *Streptococcus pneumoniae* (12.9%), and *Staphylococcus aureus* (10.0%), and *Haemophilus influenzae* (7.1%). The surfaces with the highest positive sample rate were kitchen tables (100%), water fountain faucet heads (73.3%), and water cooler cover edge (84.6%).²²

Samples were taken from a total of 99 toilet door handles and 45 faucet heads, which are frequently used by health personnel, patients, and visitors in different units of the Firat University Faculty of Medicine hospital (Elazığ-Turkey). Growth was observed in 55 (55.5%) of 99 toilet

door handles and 31 (68.8%) of 45 faucet heads. Multiple growths were detected in 87% of positive cultures.¹⁶

4. Conclusion

The risk of infection is increasing the shared use of areas such as toilets in schools. With the study, results were obtained regarding the bacterial presence in the toilets with swab samples from washbasin, faucet heads, and toilet door handles of the toilets actively used by female and male students in 9 faculties located on the Erdoğan Akdağ campus of Yozgat Bozok University.

The swab samples were taken to the laboratory in accordance with the cold chain rules and pathogenic bacteria researches were carried out. In 34 (62.96%) of the swab samples taken, a total of 49 pathogenic bacteria were detected, growing singly or in multiples. Of the 49 bacteria detected, 15 were (30.6%) *Escherichia coli*, 12 were (24.5%) *Staphylococcus aureus*, nine were (18.3%) *Klebsiella spp.*, six were (12.3%) *Pseudomonas spp.*, five were (10.2%) *Proteus spp.* and two were (4.1%) *Enterococcus spp.*

Extremely important results in terms of hygiene have been revealed in the research. Hand hygiene is one of the most effective ways to prevent the transmission of microorganisms that cause infection in the school environment. Improving the cleaning services of shared toilets, supply of cleaning materials, correct and hygienic use and compliance with hand washing rules will greatly reduce bacterial contamination and infection. In addition, monitoring, monitoring, and protection of the cleaning processes in the nine faculties of Yozgat Bozok University Erdoğan Akdağ campus, training on personal hygiene, and ensuring the continuity of these training are extremely important in preventing the transmission and spread of infectious diseases.

Acknowledgement

This study was produced from the master's thesis prepared by the first author under the supervision of the second author, supported by the Scientific Research Projects Unit of Yozgat Bozok University (Project Number: 6601-FBE/19-270). Also, we would like to thank for his opinions, suggestions, and help during the laboratory studies, Prof. Dr. Dilek PANDIR (Yozgat Bozok University), Prof. Dr. Neziha YILMAZ (Ufuk University), and we would like to thank Dr. Müge ARSLAN (Yozgat City Hospital).

Author's Contributions

Yasemin KELEŞ DİNÇ: Performed the experiments' progress, result interpretation and helped in manuscript preparation.

Sedat PER: Prepared experimental method, supervised

the experiment's progress, result in interpretation and helped in manuscript preparation

Ethics

There are no ethical issues after the publication of this manuscript.

References

- [1]. Sarı, MH. Okul, Öğretmen ve Öğrenci. In: Uzunöz A (ed) Eğitim Bilimine Giriş, Pegem Akademi, Ankara, 2016, pp 341-380.
- [2]. Temel, F, Akın, L, Vaizoğlu, SA, Kara, Ö, Kara, A, Halas, AM, Gurunaidu, SS, Oğur, R, Tekbaş, ÖF, Güler, Ç. 2006. Altındağ İlçesindeki Bir İlköğretim Okulunda Suyun ve Tuvalet, Musluk ve Kapı Kollarının Sürüntü Örneklerinin Değerlendirilmesi. *Gülhane Tıp Dergisi*; 48: 70-74.
- [3]. Thanou, N, Nikolopoulou, E, Cigarettes, DE. 2018. Hygiene Microbiology (Υγιεινή Μικροβιολογία). Diofantos Computer Technology and Publications Institute, 2018, pp 267.
- [4]. Jumaa, PA. 2005. Hand hygiene: simple and complex. *International Journal of Infectious Diseases*; 9(1): 3-14.
- [5]. Öztürk O, Öztürk C, Delialioğlu N, Emekdaş G 2010. Çoklu antibiyotik dirençli gram negatif bakterilerde kolistin duyarlılığının belirlenmesi, *Mersin Üniversitesi Sağlık Bilimleri Dergisi*; 3(3): 15-20.
- [6]. Bektaşlı, F. 2018. Fen ve Biyoloji Öğretmen Adaylarının Arkebakteri, Bakteri ve Protista Alemi Hakkındaki Bilgi Düzeyleri ve Kavram Yanılgıları, Hacettepe Üniversitesi. Eğitim Bilimleri Enstitüsü, Yüksek Lisans Tezi, pp 151.
- [7]. Flores, GE, Bates, ST, Knights, D, Lauber, CL, Stombaugh, J, Knight R, Fierer N. 2011. Microbial Biogeography of Public Restroom Surfaces. *PLoS ONE* 6(11): e28132. <https://doi.org/10.1371/journal.pone.0028132>
- [8]. Amala, SE., Ade, AJ. 2015. Bacteria Associated with Toilets and Offices Lock Handles. *International Journal of Epidemiology and Infection* 3(1): 12-15.
- [9]. Mohammed, ANAY, 2015. Assessment of Gram-Positive Bacteria on Door Handles of Service Offices at some Universities in Khartoum State, Sudan University of Science and Technology College of Graduate Studies, MSc, pp 37.
- [10]. Salah, HAA. 2015. Assessment of Gram-Negative Bacterial Contamination on Door Handles of Service Offices in Sudanese Universities, Khartoum State, Sudan University of Science and Technology College of Graduate Studies, MSc, pp 35.
- [11]. Shawly, S. 2017. Prevalence, Antibiotic Susceptibility and Plasmid Profile of Bacteria Isolated from Door Handles of Washrooms of a Hospital in Dhaka, BRAC University, Bangladesh, BSc, pp 81.
- [12]. Alkhamis AM, Noweir, M. 2018. Role of common environmental surfaces in the school in transmission enteric bacterial pathogens. *Archives of General Internal Medicine*, 2(3), 36-41.
- [13]. Arhin, RE, Hackman, HK, Whyte, BK, Sa-eed, A. 2020. Microbial diversity and antibiotic resistance of bacteria on washroom fomites in a public university. *European Journal of Health Sciences*. 5(1):1-11.
- [14]. Tijani, NA, Awojobi, OK. 2021. Characterization of Bacteria from Toilet Door Handles in some Selected Buildings at Obafemi Awolowo University, Ile-Ife, Osun State. *Premier Journal of Engineering and Applied Sciences*, 7(3): 29-38.



- [15]. Nay, MA. 2015. Assessment of Gram-Positive Bacteria on Door Handles of Service Offices at some Universities in Khartoum State. Sudan University, PhD, pp 37.
- [16]. Alonge, OO, Auwal BM, Aboh MI 2019. Bacterial Contamination of Toilet Door Handles On Baze University Campus Abuja Nigeria. *African Journal Clinical Experimental Microbiology*; 20 (1): 35-41.
- [17]. Yılmaz, A, Uslu, H, Ayyıldız, A. 2014. Erzurum Merkezindeki Bazı Okullardaki Lavabo-Tuvalet Muslukları ve Sularının Mikrobiyolojik Yönden İncelenmesi. *Türk Hijyen ve Deneysel Biyoloji Dergisi*; 71(2): 75-80.
- [18]. Flores, GE, Bates, ST, Knights, D, Lauber, CL, Stombaugh, J, Knight, R, Fierer, N. 2001. Microbial Biogeography of Public Restroom Surfaces. *PLoS ONE*; 6(11): e28132.
- [19]. Scott, E, Bloomfield, S, Barlow, C. 1982. An investigation of microbial contamination in the home. *Journal of Hygiene Cambridge*; 89(2), 279-293.
- [20]. McGinnis, S, Marini, D, Amatya, P, Murphy, HM. 2019. Bacterial Contamination on Latrine Surfaces in Community and Household Latrines in Kathmandu, Nepal. *International Journal of Environmental Research Public Health*; 16: 257.
- [21]. Matini, E, Shayeghi, F, Vaghar, ME, Nematian, J, Hosseini, SS, Mojri, N, Taherabadi, NT, Hakimi, R, Ahmadi, N, Badkoubeh, N, Esmaeili, H, Akhlaghi, M, Vaseghnia, H. 2020. A survey of public restrooms microbial contamination in Tehran city, capital of Iran, during 2019. *Journal of Family Medicine and Primary Care*; 9(6): 3131-3135.
- [22]. Hoang, VT, Sow, D, Belhouchat, K, Dao, TL, Ly, TDA, Fenollar, F, Yezli, S, Alotaibi, B, Raoult, D, Parola, P, Santi, VP, Gautret, P. 2020. Environmental investigation of respiratory pathogens during the Hajj 2016 and 2018. *Travel Medicine and Infectious Disease*; 33: e101500.

Detection of Red, Yellow, and Green Lights in Real-Time Traffic Lights with YOLO Architecture

Abdil Karakan^{1*} 

¹ Department, Dazkırı Vocational Scholl, Afyon Kocatepe University, 03204 Afyonkarahisar, Türkiye

* akarakan@aku.edu.tr

* Orcid No: 0000-0003-1651-7568

Received: 5 February 2024

Accepted: 2 May 2024

DOI: 10.18466/cbayarfbe.1432356

Abstract

In the study, red, yellow, and green lights at traffic lights were detected in real-world conditions and in real time. To adapt to real-world conditions, A data set was prepared from traffic lights in different locations, lighting conditions, and angles. A total of 5273 photographs of different traffic lights and different burning lamps were used in the data set. Additionally, grayscale, bevel, blur, variability, added noise, changed image brightness, changed color vibrancy, changed perspective, and resized and changed position have been added to photos. With these additions, the error that may occur due to any distortion from the camera is minimized. Four different YOLO architectures were used to achieve the highest accuracy rate on the dataset. As a result, the study obtained the highest accuracy at 98.3% in the YOLOV8 architecture, with an F1-Score of 0.939 and mAP@.5 value of 0.977. Since the work will be done in real time, the number of frames per second (FPS) must be the highest. The highest FPS number was 60 in the YOLOv8 architecture.

Keywords: Deep learning, traffic light, real-time detection, YOLOV8

1. Introduction

In recent years, electric vehicles have come to the fore again. The most important reason is that technology is advancing rapidly, and fossil fuels are losing their appeal [1]. Another reason is that electric vehicles are environmentally friendly [2]. Internal combustion engines have carbon emissions. Although efforts are made to reduce these rates, they remain high. Carbon emissions exceed the acceptable level with the increased number of vehicles. For this reason, it has accelerated the search for cleaner automobiles globally [3]. With the rapid development of technology, the concept of driverless vehicles has been added to electric vehicles. Electric vehicles have a very suitable structure for autonomous vehicles [4]. Mechanical control in an electric vehicle is minimal. It is mainly controlled electrically. In an electric vehicle, many controls, such as vehicle movement, braking, charging, and steering control, are performed by electrical signals. For this reason, it facilitates software-based control [5]. Artificial intelligence is used in many areas. One of these is electric vehicles. Electric vehicles can recognize their surroundings through sensors around the car. Thanks to sensors, vehicles can be developed as driverless [6]. The first way to get information from the environment of an

electric and autonomous vehicle is through cameras and sensors. The use of sensors produced with the advanced technology used today in autonomous vehicles is also efficient and active [7-13]. The most important example of this is traffic lights. More than detecting traffic lights by cameras is required. The condition of the lights is also essential for autonomous drivers. There are many studies on the detection of traffic lights [14-20].

Many different deep-learning architectures are used to detect traffic lights. YOLO architecture provides good results in detecting traffic lights. They focused on specific features such as shape, color, and texture to detect traffic lights. In the study, hand-made features were added to the system to prevent sensor and atmospheric noise. Bosch small traffic light dataset was used as the dataset. As a result of the study, 55.7% mAP result was obtained. As a result of the study, only a traffic light was detected [21]. Multi Backbone Network (MBBNet) is a different architecture used for traffic light detection. MBBNet consists of three co-convolution modules. These are normal, residual, and DenseNet highway modules. With the study conducted, an accuracy of 0.94 was achieved. The size of the work is 1.35 MB. With this small size, it has achieved low power consumption, high resolution, and 14 FPS speed [22].

Using an accurate data set to detect traffic lights may be appropriate sometimes. Obtaining an actual data set is high in terms of time and cost. More accurate data is needed for this dataset. Somewhat unrealistic computer graphics were used. In this way, the data set was fast and cost-effective. As a result of the study, it was compared with the studies obtained with the actual data set; in the study in which the data set was prepared using computer graphics, a 4% higher accuracy rate was obtained [23]. Traffic lights are always working. For this reason, an effort was made to detect traffic lights during the day and at night. He used color features to detect traffic lights. The data set used two types of traffic lights: those illuminated by traditional bulbs and LED lights. Bayesian methane was used to filter the captured images. As a result of the study, an accuracy of 99.4% was achieved [24]. The regression method is a different method of detecting traffic lights. In this method, they used images taken from cameras mounted on vehicles. With this image, they detected small traffic lights with a focus regression deep learning architecture consisting of an encoder-decoder. In their study, they used the Bosch small traffic lights and LISA large traffic lights dataset. The study conducted with a small data set reached a maximum accuracy rate of 42%. The study was conducted with a large data set, reaching a maximum accuracy rate of 49%. The larger the data set, the higher the accuracy rate [25]. Traffic lights are only sometimes located in flat places. It is not easy to detect, especially at level crossings. Traffic flow is very intense at level crossings. They worked on a portable system to detect traffic lights at this density. In their study, they used DTDNet-Lite architecture to detect traffic lights. ResNet18 was used to increase the accuracy rate in their studies. VOC 2007 and a customized data set were used as the data set [26]. Convolutional Neural Networks and Deep Learning can be used to detect traffic lights. It used YOLOV5 and AlexNet architectures for traffic light detection. It used YOLOV5 architecture to detect and identify traffic lights. They then used AlexNet architecture to classify images. They created their own data sets instead of ready-made ones in their study. The data set they created contained low-light images. They used the ZeroDCE low light enhancement algorithm on the data set for this. As a result of their study, they achieved an accuracy of 87.75% [27].

In literature studies, only traffic lights are detected. More than detecting traffic lights is required in autonomous driving. In addition to the traffic light, it is also necessary to determine which light is on. Thus, autonomous driving takes place. In addition, Bosch's small traffic light dataset was mainly used in literature studies. The LISA ample traffic light dataset is mainly used. Studies carried out with this data remain only in simulation. It could be more successful in real applications. In real life, traffic lights' locations, sizes, shapes, and sizes vary. The data set created for autonomous driving should include traffic lights in real life. The data set created for this was

obtained from traffic lights used in real life. While creating the data set, the traffic lights' location and height were considered. Photos were taken from different angles. In addition, a data set was created by taking photographs at different light intensities to detect day and night. Eight different YOLO architectures were used to achieve the highest accuracy rate in the created data set. In addition to accuracy, the FPS rate must also be very high. When the detection process is real-time, the FPS rate must be high as well as accurate. As a result of the study, FPS was 60.

2. Materials and Methods

The study was carried out in three stages. In the first stage, the data set was prepared. For this purpose, real-life traffic lights were used. Thus, when the study is implemented, it will provide higher compliance in real life. The highest accuracy was achieved in the second stage using the data set in four different architectures. Since the work will be real-time, the FPS rate must also be excellent. In the last stage, it has been implemented in real life. Figure 1 shows the general structure of the study carried out to detect traffic lights.

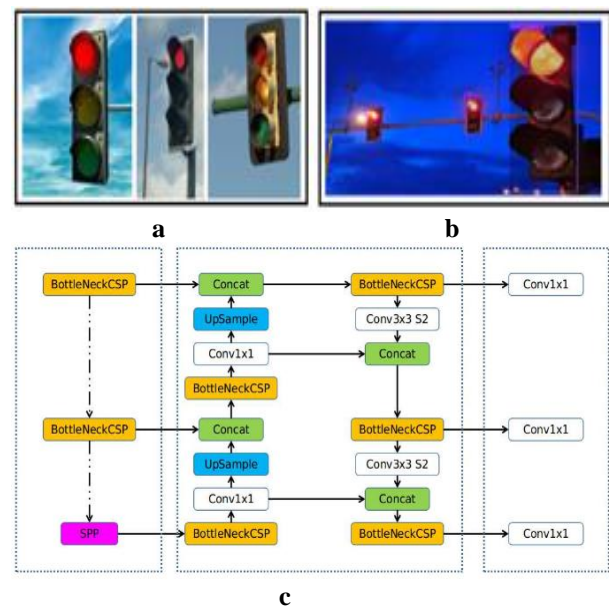


Figure 1. a) Preparation of the data set b) Study implementation in real life. c) Using the data set in eight different YOLO architectures [28].

2.1. Data Set

The first process to perform deep learning operations is to create the data set. Data set: Depending on the field in which it will be used, it may consist of mathematical expressions or visuals. Since traffic lights will be detected in real-time within the scope of this study, the data set consists of their images. It consists of an image matrix for digital processing. This matrix contains values between 0-255. With this data set, deep learning was

carried out using the Yolo algorithm to find traffic lights in a photo, video, or real-time image. For this process, the data to be used must first be collected. Data collection was achieved through manual photography. There are three essential points to consider when collecting images.

Different locations: To find an object in a photo, video, or real-time image to be used in machine learning, the images of that object to be used in the data set must consist of images taken from different angles. This is important in minimizing erroneous object detection caused by an autonomous vehicle located on the right or left side of the road or at different heights when detecting traffic lights.

Different lighting conditions and levels: Machine learning, performed with a data set consisting of photographs taken into account, will facilitate object detection in images with light levels that will likely be encountered at different times of the day. Thanks to deep learning performed with a data set consisting of images taken at different distances, the vehicle can detect traffic lights from different distances.

Deep learning will be much more efficient because it addresses these issues. The data must be labeled after the collection process is completed. The labeling process enables marking the parts of the image containing meaningful pixels belonging to the desired object or person. In the study, red, yellow, and green lights of traffic lights were labeled. Many changes were made to the images that make up the data set, thus increasing their compatibility with the natural environment. The work carried out will be detected in real time. This will be done with images taken from the camera. An error that may occur in the camera will make detection difficult. For this purpose, all errors that may occur in the camera were applied to the photographs in the data set. Figure 2a, 25% variability has been added to the positioning and sizing of the images that comprise the database. Thus, this process was done with the help of the model being more durable, depending on the camera position. In Figure 2b, the images in the database are grayscale. In Figure 2c, +15% and -15% slope has been added to the images. In Figure 2d, random Gaussian blurring was performed to be more resistant to camera focus. In Figure 2e, +15% and -15% variability has been added to the rotations to be more resistant to camera roll. In Figure 2f, noise has been added to make it more robust against camera artifacts. In Figure 2g, +15% and -15% changes were made to the image brightness to make the model resistant to lighting and camera changes. In Figure 2h, the vividness of the colors in the images is randomly adjusted. In Figure 2i, perspective variability has been added to make it more resistant to camera, subject curtain, and aberration.

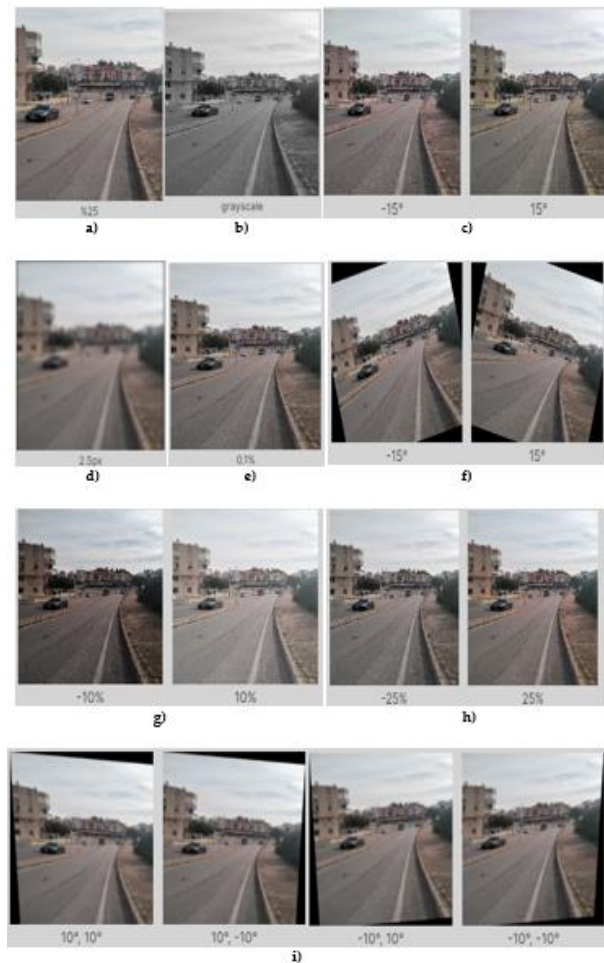


Figure 2 a) Sizing and position change, b) Grayscale, c) Adding slope, d) Blurring, e) Adding variability, f) Adding noise, g) Image brightness change, h) Colour vividness change, i) Perspective change.

2.2. YOLO Architecture

As its working principle, YOLO transforms the detection process into a regression process. Unlike Fast R-CNN, a traditional method, YOLO does not require possible areas where the object can be found to detect an object. Regression allows bounding box coordinates and probabilities to be created simultaneously for each class in the image. Instead of processing the image separately for each class, the image is looked at only once. After viewing the image, bounding box coordinates and probabilities for all classes are created. In this way, learning which objects are in the image and where precisely the objects are in the image is achieved very quickly. This significantly shortens the detection time compared to traditional object detection systems. Figure 3 shows the general structure of the YOLO architecture.

$$mAP = \int_0^1 P(R)dR \quad (3.5)$$

1_i^{obj} = If there is an object in the cell, it is 1, otherwise it is 0.

$A_i(C)$ = It means the conditional class probability for class c in cell i.

The localization loss calculates the loss value related to the location and size of the estimated bounding box. It is calculated only for the box detecting the object. It is possible to see the localization loss equation in Equation 3.6.

$$\begin{aligned} & \lambda_{coord} \sum_{i=0}^{S^2} \sum_{j=0}^B 1_{ij}^{obj} \left[(E_i - \hat{E}_i)^2 + (y_i - \hat{y}_i)^2 \right] \\ & + \lambda_{coord} \sum_{i=0}^{S^2} \sum_{j=0}^B 1_{ij}^{obj} \left[(\sqrt{w_i} - \sqrt{\hat{w}_i})^2 + (\sqrt{h_i} - \sqrt{\hat{h}_i})^2 \right] \end{aligned} \quad (3.6)$$

1_{ij}^{obj} = If the bounding box j in cell i is responsible for object detection, it is 1, otherwise it is 0.

λ_{coord} = It increases the weight of the loss value in the bounding box coordinates.

Confidence loss calculates the confidence value of the detecting box when the object is detected. It is possible to see the loss of trust equation in Equation 3.7 and 3.8.

$$\sum_{i=0}^{S^2} \sum_{j=0}^B 1_{ij}^{obj} (C_i - \hat{C}_i)^2 \quad (3.7)$$

\hat{C}_i = is the confidence value of box j in cell

1_{ij}^{obj} = If the bounding box j in cell i is responsible for object detection, it is 1, otherwise it is 0.

Loss of trust if no object is detected in the box:

$$\lambda_{noobj} \sum_{i=0}^{S^2} \sum_{j=0}^B 1_{ij}^{noobj} (C_i - \hat{C}_i)^2 \quad (3.8)$$

\hat{C}_i = is the confidence value of box j in cell i.

$1_{ij}^{noobj} = 1 - 1_{ij}^{obj}$ is the complement value of.

λ_{noobj} = It is used to reduce loss when background is detected.

Final loss value; It is the sum of classification, localization and loss of confidence values.

$$\begin{aligned} & \lambda_{coord} \sum_{i=0}^{S^2} \sum_{j=0}^B 1_{ij}^{obj} \left[(E_i - \hat{E}_i)^2 + (y_i - \hat{y}_i)^2 \right] + \\ & \lambda_{coord} \sum_{i=0}^{S^2} \sum_{j=0}^B 1_{ij}^{obj} \left[(\sqrt{w_i} - \sqrt{\hat{w}_i})^2 + (\sqrt{h_i} - \sqrt{\hat{h}_i})^2 \right] + \\ & \sum_{i=0}^{S^2} \sum_{j=0}^B 1_{ij}^{obj} (C_i - \hat{C}_i)^2 + \\ & \lambda_{noobj} \sum_{i=0}^{S^2} \sum_{j=0}^B 1_{ij}^{noobj} (C_i - \hat{C}_i)^2 + \\ & \sum_{i=0}^{S^2} \sum_{c \in \text{classes}} 1_{ij}^{obj} (A_i(C) - \hat{A}_i(C))^2 \end{aligned} \quad (3.9)$$

3.1. YOLOv8 Architecture Results

Firstly, the dataset YOLOV8 architecture was used in the study. The training period for identifying the red, yellow, and green lights in traffic lights to the YOLOV8 architecture lasted 3 hours, 7 minutes, and 13 seconds. The highest accuracy rate for traffic lights was 99.1% in red lights, 98.6% in yellow lights, and 98.6% in green lights. The average accuracy rate was 98.3%. Table 1 shows the results occurring in the YOLOv8 architecture.

Table 1. Results of YOLOv8 architecture

Class	Precision	Recall	F1-Score	mAP@.5
All	0.983	0.903	0.939	0.977
Red	0.991	0.916	0.943	0.975
Yellow	0.986	0.893	0.937	0.980
Green	0.972	0.910	0.939	0.971

The training process was carried out using the data set consisting of red, yellow, and green lights in the YOLOV8 architecture. The performance values of YOLOV8 architecture are Precision 98.3%, Recall 90.3%, F1-Score 0.939, mAP@.5 0.977, mAP@.5:95:0.788. As a result of the YOLOV8 architecture, the complexity matrix consists of two parts: the predicted value and the actual value. Figure 4 shows the complexity matrix realized in the system.



Figure 4. Complexity matrix resulting from YOLOV8 architecture

3.2. Other Architecture Results

In addition to the YOLOV8 architecture, YOLOV5, YOLOV6, and YOLOV7 architectures were also used in the study. The same data set was used in YOLOV5, YOLOV6, and YOLOV7 architectures. In this way, the error rate was tried to be minimized. Different mathematical algorithms were used in YOLOV5,

YOLOV6, and YOLOV7 architectures. For this reason, the results are different. Table 2 shows the average values of YOLOV5, YOLOV6, and YOLOV7 architectures.

Table 2. Average results of YOLOV5, YOLOV6, and YOLOV7 architectures.

Class	Precision	Recall	F1-Score	mAP@.5
YOLOV5	0.920	0.939	0.932	0.971
YOLOV6	0.68	0.935	0.962	0.985
YOLOV7	0.911	0.899	0.911	0.949

Even though the same data set is used in YOLO architectures, different results are obtained. The biggest reason is that different mathematical algorithms are used in each architecture. This varies depending on the size or smallness of the data set. However, the most essential feature is the usage area.

When the study examined the accuracy, the highest accuracy was obtained at 98.30% in the YOLOv8 architecture. The lowest accuracy was in the YOLOv6 architecture. The second and third accuracy rates were achieved in YOLOv5 and YOLOv7. When the F1 scores are examined, the highest rate occurred in the YOLOv6 architecture. It was later implemented in YOLOv8, YOLOv5 and YOLOv7 architectures.

All architectures used in the system used the same number of photos and photo sizes. As a result of the study, the highest accuracy rate was 0.98 for the YOLOv8 architecture. These values are average values. There are different accuracy rates for red, yellow, and green traffic lights. The reason for this is the differences between the lights. Average values were taken in the study. An accuracy rate of 0.98 was achieved in the YOLOv8 architecture. The lowest accuracy rates were 0.68 in the YOLOv6 architecture. It was 0.920 and 0.911 in YOLOv5, and YOLOv7 architectures. The accuracy rates of YOLOv5 and YOLOv8 architectures are close to each other. Figure 5 shows one result of the operation of the system.



Figure 5. One result of the operation of the system. Since the work will be real-time, the FPS speed must be sufficient. In the YOLOv8 architecture, which gives the highest accuracy rate, the speed has increased to 60 FPS.

At this rate, it is sufficient for real-time detection. For this reason, a camera has been placed inside the vehicle. Real-time detection was carried out with images taken from the camera.

When the literature studies are examined, many studies have been done. In these studies, ready-made data sets were only used. In some studies, the most appropriate data set for the system was prepared. Table 3 shows the comparison of literature studies.

Table 3. Comparison of literature studies.

Writer	Number of Image	Architectural	Precision
Xie et al. [29]	7000	Faster R-CNN	%97.20
Boyuk et all. [30]	8726	Faster R-CNN	%75.16
Kamran et all. [31]	1586	Faster R-CNN	%60.72
Gupta et all. [32]	6772	YOLOv3-Tiny	%77.00
Kyrkou et all. [33]	350	Dronet	%95.00
Sun et all. [34]	32	YOLOv5	%93.30
Yong et all. [35]	755	GoogleNet	%73.01
Mansour et all. [36]	397	Faster R-CNN	%89.21
Bayram et all. [37]	3008	YOLOv6	%98.30
Galayol et all. [38]		YOLOv7	%93.42
Hassan et all. [39]		YOLOv6	%55.7
Ngoc et all. [40]		YOLOv8	%98.50
Gao et all. [41]		YOLOv4	%80.00
Sarhan et all. [42]	90	YOLOv3	%76.00
Omar et all. [43]		YOLOv3	%67.21
Nui et all. [44]		YOLOv5	%87.75

As a result of the literature review, it is understood that the use of previously made systems in daily life is quite difficult. These difficulties have low fps value. For this reason, the systems cannot be used in real-time. The systems only stopped at traffic lights in certain places. In this case, different traffic lights cause the systems to be

detected at a very low rate or not at all. The data sets used in the studies consist of photographs taken at a certain time of the day. In real life, traffic lights are encountered at different times of the day.

Four of the latest versions of the YOLO architecture were used in the study. In this way, the highest accuracy and fps rates were determined by comparison. Since YOLO architectures only look at the image once and perform the detection process, their frame rates are excellent. A speed of 60 fps was achieved in the YOLOv8 algorithm. In this way, detection can be done very quickly in real-time.

Since the study will be used in real life, the data set must be prepared very well. For this purpose, the data set was prepared according to three important rules. These include different locations, lighting conditions, and levels, and finally, different distances. Examples were taken from traffic lights in different locations in real life. Images of traffic lights were taken under different lighting conditions and levels. Images were taken at different times of the day. Finally, images were taken from different distances. Thanks to these images, a data set was created. The more suitable the data set is to real life, the more accurate the detection process becomes.

4. Conclusion

Autonomous devices are increasing in our lives day by day. The most important of these is that electric vehicles are autonomous. For electric vehicles to be autonomous, detecting traffic lights will not be enough. In order for the vehicle to move, it is necessary to determine which traffic light is on. The study carried out the detection of red, yellow, and green lights of traffic lights. For this, YOLOv8, YOLOv7, YOLOv6, and YOLOv5 architectures were used. An accuracy of 98.3% was achieved in the YOLOv8 architecture. A speed of 60 fps was achieved in the YOLOv8 architecture. Thus, real-time detection was made. The data set was prepared with images obtained from real traffic lights. These images were obtained at traffic lights of different shapes. In this way, the detection of red, yellow, and green lights in real-life traffic lights has been achieved at a very high rate.

The locations, shapes, and scales of traffic lights are very different. Traffic lights are difficult to detect in real-world conditions due to their similarity to other objects. In addition to these features, detecting traffic lights is not sufficient in autonomous driving. It is necessary to determine which of the red, yellow, and green lights is on at traffic lights. In the study, red, yellow, and green lights on traffic lights were detected in real-time. With the study conducted, traffic lights were detected in many different ways in real life with high accuracy. For autonomous driving, detection alone is not enough. The detection process needs to be adapted to the autonomous system. First of all, a warning system should be added to the driver. The driver must be warned audibly and visually.

In the next work, the vehicle should be enabled to switch to autonomous driving and brake automatically. In this way, human error will be minimized.

Ethics

There are no ethical issues after the publication of this manuscript.

References

- [1]. Diaz-Cabrera, M, Cerri, P, Medici, P. 2015. Robust real-time traffic light detection and distance estimation using a single camera. *Expert. Syst. Appl.*; 42, 3911–3923. <https://doi.org/10.1016/j.eswa.2014.12.037>
- [2]. Hosseinyalamdary, S, Yilmaz, A. 2017. A Bayesian approach to traffic light detection and mapping, ISPRS J. Photogram. *Remote Sens.*; 125, 184–192. <https://doi.org/10.1016/j.isprsjprs.2017.01.008>
- [3]. Li, X, Ma, H, Wang, X, Zhang, X. 2018. Traffic light recognition for complex scene with fusion detections. *IEEE Trans. Intell. Transp. Syst.*; 19, 199–208. <https://doi.org/10.1109/TITS.2017.2749971>
- [4]. Bolor, A, Garimella, K, He, K, Gill, C, Vorobeychik, Y, Zhang, X. 2020. Attacking vision-based perception in end-to-end autonomous driving models. *J. Syst. Archit.*; 101766. <https://doi.org/10.1016/j.sysarc.2020.101766>
- [5]. Jensen, M.P, Philipsen, M.P, Møgelmoose, A, Moeslund, T.B, Trivedi, M.M. 2016. Vision for looking at traffic lights: issues, survey, and perspectives. *IEEE Trans. Intell. Transp. Syst.*; 17, 7, 1800–1815. <https://doi.org/10.1109/TITS.2015.2509509>
- [6]. Ouyang, Z, Niu, J, Liu, Y, Guizani, M. 2019. Deep cnn-based real-time traffic light detector for self-driving vehicles. *IEEE Trans. Mob. Comput.*; 19, 2, 300–313. <https://doi.org/10.1109/TMC.2019.2892451>
- [7]. Kim, J, Cho, H, Hwangbo, M, Choi, J, Canny, J, Kwon, Y.P. Deep traffic light detection for self-driving cars from a large-scale dataset, in: 2018. *21st International Conference on Intelligent Transportation Systems (ITSC)*, Maui, Hawaii, USA, 4-7 November 2018, pp. 280–285. <https://doi.org/10.1109/ITSC.2018.8569575>
- [8]. Jensen, M, Philipsen, M, Møgelmoose, A, Moeslund, T, Trivedi, M. 2016. Vision for looking at traffic lights: issues, survey, and perspectives. *IEEE Trans. ITS.*; 17, 7, 1800–1815. <https://doi.org/10.1109/TITS.2015.2509509>
- [9]. Behrendt, K, Novak, L, Botros, R. 2017. A deep learning approach to traffic lights: detection, tracking, and classification. *IEEE ICRA*; pp. 1370–1377. <https://doi.org/10.1109/ICRA.2017.7989163>
- [10]. Sommer, L.W, Schuchert, T, Beyerer, J. Fast deep vehicle detection in aerial images. *IEEE Winter Conference on Applications of Computer Vision (WACV)*, IEEE; Santa Rose, California, USA. 24-31 March 2017. pp. 311–319. <https://doi.org/10.1109/WACV.2017.41>
- [11]. Zhang, X, Story, B, Rajan, D. 2021. Night time vehicle detection and tracking by fusing vehicle parts from multiple cameras. *IEEE Trans. Intelligent Transp. Syst.*; pp. 258-265. <http://dx.doi.org/10.1109/TITS.2021.3076406>
- [12]. Chen, C, Liu, B, Wan, S, Qiao, P, Pei, Q. 2021. An edge traffic flow detection scheme based on deep learning in an intelligent transportation system. *IEEE Trans. Intelligent Transp. Syst.*; 22, 3, 1840–1852. <https://doi.org/10.1155/2021/5583874>
- [13]. Zhang, Z, Zaman, A, Xu, J, Liu, X. 2022. Artificial intelligence-aided railroad trespassing detection and data analytics: methodology and a case study. *Accident Anal. Prevention*; 168, 106594. <https://doi.org/10.1016/j.aap.2022.106594>



- [14]. Tsai, L.W, Hsieh, J.W, Fan, K.C. 2007. Vehicle detection using normalized color and edge map. *IEEE Trans. Image Process*; 16, 3, 850–864. <https://dx.doi.org/10.1109/tip.2007.891147>
- [15]. Ehtesham, H, Yasser, K, Imtiaz, A. 2023. Learning deep feature fusion for traffic light detection. *Journal of Engineering Research*; 11, 94–99. <https://dx.doi.org/10.1155/2020/7286187>
- [16]. Zhenchao, O, Jianwei, N, Tao, R, Yanqi, L, Jiahe, C, Jiyan, W. 2020. MBBNet: An edge IoT computing-based traffic light detection solution for autonomous bus. *Journal of Systems Architecture*; 109, 101835. <http://dx.doi.org/10.1016/j.sysarc.2020.101835>
- [17]. Jean, P, V, M, Lucas, T, Rodrigo, F, B, Thiago, M, Alberto, F, S, Claudine, B, Nicu, S, Thiago, O, S. 2021. Deep traffic light detection by overlaying synthetic context on arbitrary natural images. *Computers & Graphics*; 94, 76–86. <https://doi.org/10.48550/arXiv.2011.03841>
- [18]. Moises, D.C, Pietro, C, Paolo, M. 2015. Robust real-time traffic light detection and distance estimation using a single camera. *Expert Systems with Applications*; 42, 3911–3923. <https://doi.org/10.1016/j.eswa.2014.12.037>
- [19]. Eunseop, L, Daijin, L. 2019 Accurate traffic light detection using deep neural network with focal regression loss. *Image and Vision Computing*, 87, 24–36. <https://doi.org/10.1016/j.imavis.2019.04.003>
- [20]. Feng, G, Yi, W, Yu, Q. 2023. Real-time dense traffic detection using lightweight backbone and improved path aggregation feature pyramid network. *Journal of Industrial Information Integration*; 31, 100427. <https://doi.org/10.1016/j.jii.2022.100427>
- [21]. Chuanxi, N, Kexin, L. 2022. Traffic Light Detection and Recognition Method Based on YOLOv5s and AlexNet. *Appl. Sci*; 12, 10808. <https://doi.org/10.3390/app122110808>
- [22]. Lin, T.Y, Goyal, P, Girshick, R, He, K, Doll'ar, P. Focal loss for dense object detection. *Proceedings of the IEEE international conference on computer vision*, Venice, Italy, 22-29 Oct. 2017, pp. 2980–2988. <https://doi.org/10.1109/ICCV.2017.324>
- [23]. Liu, Y, Sun, P, Wergeles, N, Shang, Y. 2021. A survey and performance evaluation of deep learning methods for small object detection. *Expert Syst. Applied*, 172, 114602. <https://doi.org/10.1016/j.eswa.2021.114602>
- [24]. Yu, W, Yang, T, Chen, C. Towards resolving the challenge of long-tail distribution in uav images for object detection, *Proceedings of the IEEE/CVF Winter Conference on Applications of Computer Vision*; Waikoloa, HI, USA. 3-8 June 2021. pp. 3258–3267. <https://doi.org/10.48550/arXiv.2011.03822>
- [25]. Sang, J, Wu, Z, Guo, P, Hu, H, Xiang, H, Zhang, Q, Cai, B. 2018. An improved YOLOv2 for vehicle detection. *Sensors*; 18, 12, 4272. <https://doi.org/10.3390/s18124272>
- [26]. Zhang, F, Yang, F, Li, C, Yuan, G. 2019. CMNet: a connect-and-merge convolutional neural network for fast vehicle detection in urban traffic surveillance. *IEEE Access*; 7, 72660–72671. <https://doi.org/10.1155/2021/5583874>
- [27]. Tan, M, Pang, R, Le, and Q.W. Efficientdet: scalable and efficient object detection. *Proceedings of the IEEE/CVF conference on computer vision and pattern recognition*; Seattle, Washington, USA. 14-19 June 2020. pp. 10781–10790. <https://doi.org/10.1109/CVPR42600.2020.01079>
- [28]. Xu, R, Lin, H, Lu, K, Cao, L, Liu, Y. 2021. A Forest Fire Detection System Based on Ensemble Learning. *MDPI Forests*, 12 (217), pp. 1568–1570. <https://doi.org/10.3390/f12020217>
- [29]. Xie, X, He, C. Object detection of armored vehicles based on deep learning in battlefield environment. *Proceedings - 2017 4th International Conference on Information Science and Control Engineering, ICISCE; Changsha, Chania, 21-23 July 2017*. 1568–1570. <https://doi.org/10.1109/ICISCE.2017.327>
- [30]. Boyuk, M, Duvar, R, Urhan, O. Deep learning based vehicle detection with images taken from unmanned air vehicle. *Proceedings 2020 Innovations in Intelligent Systems and Applications Conference, ASYU; Istanbul, Türkiye, 15-17 October 2020*. pp.175. <https://doi.org/10.1109/ASYU50717.2020.9259868>
- [31]. Kamran, F, Shahzad, M, Shafait, F. Automated military vehicle detection from low-altitude aerial images. *2018 International Conference on Digital Image Computing: Techniques and Applications, DICTA*. Canberra, Australis, 10-13 December 2018, 2 <https://doi.org/10.1109/DICTA.2018.8615865>
- [32]. Gupta, P, Pareek, B, Singal, G, Rao, D. V. 2022. Edge device based military vehicle detection and classification from UAV. *Multimedia Tools and Applications*; 81(14), 19813–19834. <https://doi.org/10.1007/S11042-021-11242-Y/FIGURES/12>
- [33]. Kyrkou, C, Plastiras, G, Theocharides, T, Venieris, S. I, Bouganis, C. S. 2018. DroNet: Efficient convolutional neural network detector for real-time UAV applications. *Proceedings of the 2018 Design, Automation and Test in Europe Conference and Exhibition*; 967–972. <https://doi.org/10.23919/DATE.2018.8342149>
- [34]. Sun, Y, Wang, W, Zhang, Q, Ni, H, Zhang, X. 2022. Improved YOLOv5 with transformer for large scene military vehicle detection on SAR image. *2022 7th International Conference on Image, Vision and Computing, ICIVC*; 87–93. <https://doi.org/10.1109/ICIVC55077.2022.9887095>
- [35]. Yong, S. P, Yeong, Y. C. 2018. Human object detection in forest with deep learning based on drone's vision. *2018 4th International Conference on Computer and Information Sciences: Revolutionizing Digital Landscape for Sustainable Smart Society, ICCOINS*; <https://doi.org/10.1109/ICCOINS.2018.8510564>
- [36]. Mansour, A, Hassan, A, Hussein, W. M, Said, E. 2019. Automated vehicle detection in satellite images using deep learning. *IOP Conference Series: Materials Science and Engineering*; 610(1). <https://doi.org/10.1088/1757-899X/610/1/012027>
- [37]. Bayram, A.F, Nabiye, V. 2023. Detection of Hidden Camouflaged Tanks Based on Deep Learning: Comparative Analysis of the art YOLO Network. *Gümüşhane University of Journal of Science and Technology*; 182-193. <https://doi.org/10.17714/gumusfenbil.1271208>
- [38]. Gelayol, G, Ignacio, M.A, Qi, W, Jose, M.A.C. 2023. Robust Real-Time Traffic Light Detection on Small-Form Platform for Autonomous Vehicles. *Journal of Intelligent Transportation System*; 1-11 <https://doi.org/10.1080/15472450.2023.2205018>
- [39]. Hassan, E, Khalil, Y, Ahmad, I. 2023. Learning Deep Feature Fusion for Traffic Light Detection. *Journal of Engineering Research*; 11, 94-99. <https://doi.org/10.1016/j.jer.2023.100128>
- [40]. Ngoc, H.T, Nguyen, K.H, Hua, H.K, Nguyen. H.V.N, Quach, L. 2023. Optimizing YOLO Performance for Traffic Light Detection and End-to-End Steering Control for Autonomous Vehicles in Gazebo-ROS2. *International Journal of Advanced Computer Science and Applications*; Vol.14. 7. <https://doi.org/10.14569/IJACSA.2023.0140752>
- [41]. Gao, H, Wang, W, Yang, C, Jiao, W, Chen, Z, Zhang, T. 2021. Traffic Signal Image Detection Technology Based on YOLO. *Journal of Physics: Conference Series*; 1-21. <https://doi.org/10.1088/1742-6596/1961/1/012012>
- [42]. Serhan, N.H, Olmary, A. Y. 2022. Traffic Light Detection Using Opencv and YOLO. *International Conference on Innovation and Intelligence for Informatics, Computing and Technologies*; 604-608. <https://doi.org/10.1088/1742-6596/1961/1/012012>



- [43]. Omar, W, Lee, I., Lee, G, Park, K.M. 2020. Detection and Localization of Traffic Light Using YOLOv3 and Stereo Vision. *The International Archives of the Photogrammetry, Remote Sensing and Spatial Information Sciences*; Vol.18, 1247-1252. <https://doi.org/10.5194/isprs-archives-XLIII-B2-2020-1247-2020>
- [44]. Nui, C, Li, K. 2022. Traffic Light Detection and Recognition Method Based on YOLOv5s and AlexNet, *Applied Science*; 12, 10808. <https://doi.org/10.3390/app122110808>

An Extended UEHL Distribution: Properties and Applications

Murat GENÇ^{1*} , Ömer ÖZBİLEN² 

¹ Department of Management Information Systems, Faculty of Economics and Administrative Sciences, Tarsus University, Mersin, Türkiye

² Department of Mathematics Education, Faculty of Education, Mersin University, Mersin, Türkiye

* muratgenc@tarsus.edu.tr

* Orcid No: 0000-0002-6335-3044

Received: 11 February 2024

Accepted: 7 June 2024

DOI: 10.18466/cbayarfbe.1435139

Abstract

This study introduces a new distribution, a Lehmann-type exponentiated distribution, which is built upon the unit exponentiated half-logistic distribution. The analytical characteristics of the proposed distribution, like moments, moment-generating function, quantiles, and stress-strength reliability, are explored in detail. The renowned maximum likelihood estimation method is employed for the statistical inference of the distribution's parameters. A computer experiment is run to explore the performance of the maximum likelihood estimates of the distribution parameters under diverse scenarios. Additionally, the practicality and efficacy of the distribution are illustrated through a numerical example using a real-world dataset.

Keywords: Exponentiated family, G-family, Maximum likelihood estimator, Reliability, UEHL distribution.

1. Introduction

Scientists have proposed many probability distributions in recent decades for data-modeling in such diverse fields as biological studies, engineering, economics and medical sciences. Recently, there has been strong interest in pursuing more flexible distributions. Researchers are constantly developing new families of probability distributions that not only expand upon existing ones but also offer greater flexibility in representing the characteristics of real-world data. In this context, constructing extended G-family distributions by applying a particular transformation to the baseline distribution is widely adopted in statistics [1, 2, 3].

The Weibull method, which builds upon the existing "exponential" method, became popular because it is better at describing many types of data across various fields. With the contribution of the extra parameters, the Weibull method can handle a wider range of data types than the exponential method. Also, the Weibull distribution is successful in modeling monotone hazard rates in reliability theory. However, the distribution has limitations in capturing scenarios with non-monotonic hazard rates, where the likelihood of failure can fluctuate over time [4, 5].

Over the years, many continuous distributions with bounded domains have been proposed and applied in various fields of application to model uncertainty in a bounded phenomenon. In particular, modeling approaches on the unit interval, have grown in popularity recently since they address specific difficulties such as the recovery rate, mortality rate, and so on. Many useful unit distributions have been proposed, such as Johnson S_B distribution [6], unit logistic distribution [7], logit slash [8], unit Johnson S_U [9] distribution, log-xgamma distribution [10], unit-Weibull distribution [11], unit Birnbaum-Saunders distribution [12], unit inverse Gaussian distribution [13], log-weighted exponential distribution [14] and Generalized exponentiated unit Gompertz distribution [15].

Dombi et al. [16] proposed the omega distribution as a generalization of the Weibull distribution with bounded support, which has several applications in reliability theory. Dombi et al. [16] demonstrated that as the parameter in the omega distribution approaches infinity, it behaves identically to the Weibull distribution. This is because the hazard rate of the omega distribution, under these conditions, becomes indistinguishable from that of the Weibull distribution. In this context, [17] proposed the unit exponentiated-half logistic (UEHL) distribution by assigning a specific value to the parameter of the omega distribution. The UEHL distribution is obtained

by a simple transformation of the exponentiated half-logistic distribution, which has been widely utilized in reliability theory [18, 19, 20, 21].

This study extends the UEHL distribution by constructing an exponentiated G-family UEHL distribution using a specific member of the G-Family distributions. Thus, we aim to improve the performance of the UEHL distribution by utilising G-Family distributions. The characteristics of this new distribution are thoroughly examined, and a performance analysis is conducted.

The rest of the paper is structured as follows: Section 2 introduces the new distribution and explores its properties (moments, MGF, quantiles, etc.). Section 3 evaluates the distribution's performance through simulations and real-data analysis. Lastly, Section 4 concludes the paper.

2. Material and Method

The proposal of novel statistical distributions based on the G-family method has gained popularity [22, 23]. The Weibull-G family of distributions was introduced by Bourguignon et al. [24], who also studied the distribution's characteristics. Shukla et al. [25] further explored the reliability characteristics of the Weibull-G family using progressively Type-II censored data. Tahir et al. [26] proposed a new G-family type generator based on the Weibull random variable and studied the mathematical properties of the distribution. Korkmaz [27] introduced the extended Weibull-G distribution based on an extended form of the Weibull distribution and discussed the special members of the new family. Alizadeh et al. [28] proposed the Gompertz-G family of distribution with some special models based on the distribution. To address the deficiencies of the odd Fréchet-G family proposed by [29], Badr et al. [30] proposed the Transmuted Odd Fréchet-G family of distributions. Eghwerido et al. [31] proposed the transmuted alpha power-G class of models for modeling lifetime processes. Chakraborty [32] introduced the Kumaraswamy Poisson-G distribution by mixing the distribution of the minimum of a random number of identically and independent Kumaraswamy-G random variables and zero truncated Poisson random variable. Alnssyan et al. [33] introduced the weighted Lindley-G family of probabilistic models as a novel family based on Lindley distribution.

Recently, depending on the structure of the dataset, the use of distributions with bounded support sets has become widespread. Mazucheli et al. [34] proposed the unit-Weibull distribution and compared the model performance with that of the Kumaraswamy distribution [35]. Guerra et al. [36] proposed the unit extended Weibull families of distributions and used the distribution to model the literacy rate data. Chakraborty

et al. [37] obtained a generalized log-Lindley distribution defined in the unit interval by extending the Log-Lindley distribution and, use the distribution to model outpatient health expenditure. Masood et al. [38] brought up the unit interval exponentiated exponential distribution and illustrated the performance of the distribution using COVID-19 data. Korkmaz and Korkmaz [39] proposed the unit log-log distribution and an alternative quantile regression with application to educational measurement data. Akata et al. [40] proposed the Kumaraswamy unit-Gompertz distribution and studied the applications of the distribution in lifetime datasets. Genç and Özbilen [41] proposed the DUS-UEHL distribution by implementing the transformation of DUS to the distribution of UEHL and investigated its characteristics in detail. Genç and Özbilen [42] proposed the EUEHL distribution, which is derived from the exponentiated transformation of the UEHL distribution and explored its characteristics using a computer experiment and an analysis of real data.

2.1. EG-UEHL distribution

The Lehmann-type exponentiated distributions are commonly used in statistics. In this context, Nadarajah [43] and, Tahir and Nadarajah [23] consider the cumulative distribution function (CDF)

$$F(x) = [1 - G(e^{-x})]^\lambda \quad (1)$$

based on the log transformation on the Lehmann type 2 distribution, where $G(x)$ is the baseline CDF and λ is a shape parameter. In this section, we introduce the two-parameter exponentiated UEHL distribution based on the G-family of distributions given by Equation (1). The CDF of the UEHL distribution is given by

$$F_{UEHL}(x; \theta, \lambda) = 1 - \left(\frac{1 - x^\theta}{1 + x^\theta} \right)^\lambda, 0 < x < 1. \quad (2)$$

By applying the distribution function in Equation (2) to the G-family of distributions in Equation (1), the CDF of the exponentiated G-family UEHL distribution is obtained as

$$F_{EG-UEHL}(x; \theta, \lambda) = \left(\frac{1 - e^{-\theta x}}{1 + e^{-\theta x}} \right)^\lambda, 0 < x < \infty \quad (3)$$

where $\theta > 0$ and $\lambda > 1$. In this study, we will use the notation $EG-UEHL(\theta, \lambda)$ to represent the exponentiated G-family UEHL distribution with the parameters θ and λ . As described in Equation (3), the probability density function (PDF) of the $EG-UEHL(\theta, \lambda)$ is given by

$$f_{EG-UEHL}(x; \theta, \lambda) = \frac{2\lambda\theta}{e^{\theta x} - e^{-\theta x}} \left(\frac{1 - e^{-\theta x}}{1 + e^{-\theta x}} \right)^\lambda, \quad 0 < x < \infty. \quad (4)$$

Figure 1 illustrates the PDF of the $EG - UEHL(\theta, \lambda)$ distribution for the different values of the parameters θ and λ . The distribution is skewed to the right and the skewness of the distribution decreases as the parameter λ increases. In addition, for large values of θ , the probabilities are large for small values of the random variable X , while the reverse is the case for small values of θ .

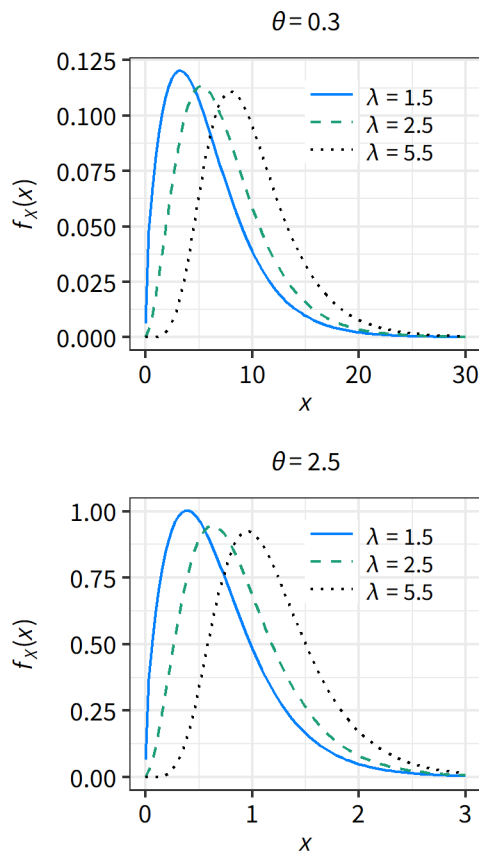


Figure 1. Plots of the PDF of the $EG - UEHL(\theta, \lambda)$ distribution for the selected θ and λ parameters.

The survival and the hazard rate functions of the $EG - UEHL(\theta, \lambda)$ distribution are provided, respectively, by

$$S_{EG-UEHL}(x; \theta, \lambda) = \frac{(1 + e^{-\theta x})^\lambda - (1 - e^{-\theta x})^\lambda}{(1 + e^{-\theta x})^\lambda}$$

and

$$h_{EG-UEHL}(x; \theta, \lambda) = \frac{2\lambda\theta}{(e^{\theta x} - e^{-\theta x}) \left(\left(\frac{1 + e^{-\theta x}}{1 - e^{-\theta x}} \right)^\lambda - 1 \right)}. \quad (5)$$

Figure 2 shows the hazard rate function for the chosen values of the parameters of the distribution. According to Figure 2, the hazard function of the $EG - UEHL(\theta, \lambda)$ distribution given by Equation (5) is an increasing function.

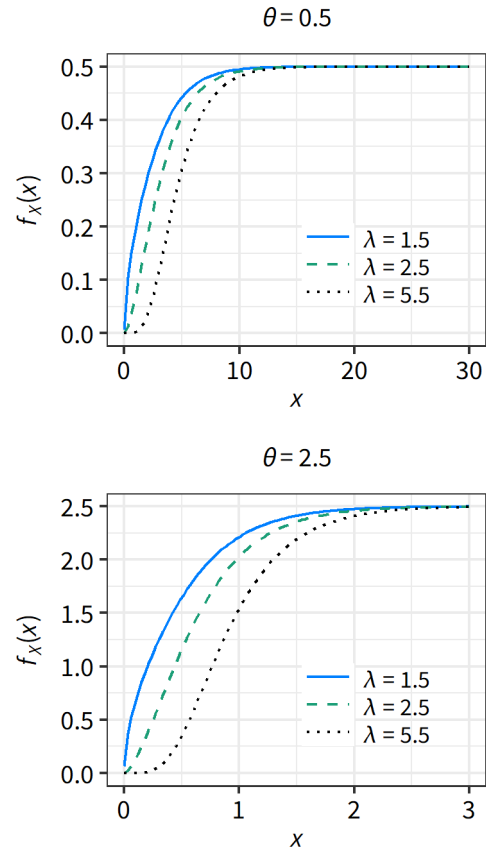


Figure 2. Plots of the hazard function of the $EG - UEHL(\theta, \lambda)$ distribution for the selected θ and λ parameters.

2.2. Statistical Characteristics of the $EG-UEHL(\theta, \lambda)$ Distribution

This section explores several analytical properties of the $EG - UEHL(\theta, \lambda)$ distribution. These include the moments, quantile function, stress-strength reliability, and maximum likelihood estimation of the distribution parameters.

2.2.1. Moments

Moments serve as valuable tools for understanding various facets of a statistical distribution. This section delves into the moments of the $EG - UEHL(\theta, \lambda)$ random variable. Let X follow a $EG - UEHL(\theta, \lambda)$ distribution with the PDF given by Equation (4). Then the r -th raw moment of X for $r = 1, 2, 3, \dots$ is

$$E(X^r) = \int_0^\infty x^r f(x; \theta, \lambda) dx$$

$$= 2\lambda\theta \int_0^\infty \frac{x^r}{e^{\theta x} - e^{-\theta x}} \left(\frac{1 - e^{-\theta x}}{1 + e^{-\theta x}} \right)^\lambda dx$$

By the transformation $u = e^{-\theta x}$, the expectation is written as

$$E(X^r) = \frac{2\lambda}{\theta^r} \int_0^1 (-\log u)^r (1-u)^{\lambda-1} (1+u)^{-\lambda-1} du.$$

By using the Binomial series $(1-t)^z = \sum_{j=0}^\infty (-1)^j \binom{z}{j} t^j$, we obtain

$$E(X^r) = \frac{2\lambda}{\theta^r} \sum_{j=0}^\infty (-1)^j \binom{\lambda-1}{j}$$

$$\times \int_0^1 (-\log u)^r u^j (1+u)^{-\lambda-1} du.$$

Applying the Equation 4.272.14 provided in [44], we obtain the r -th raw moment of the $EG - UEHL(\theta, \lambda)$ random variable as

$$E(X^r) = \frac{2\lambda}{\theta^r} r! \sum_{j=0}^\infty \sum_{k=0}^\infty \frac{(-1)^{j+k}}{(1+j+k)^{1+r}} \binom{\lambda-1}{j} \binom{\lambda+k}{k}.$$

2.2.2. Moment Generating Function

The moment generating function (MGF) offers an alternative approach for analytical characteristics instead of directly working with PDFs. Let X be an $EG - UEHL(\theta, \lambda)$ random variable with the PDF given by Equation (4). Then, the MGF of X

$$M_X(t) = \int_0^\infty e^{tx} f(x; \theta, \lambda) dx$$

$$= \int_0^\infty 2\lambda\theta \frac{e^{tx}}{e^{\theta x} - e^{-\theta x}} \left(\frac{1 - e^{-\theta x}}{1 + e^{-\theta x}} \right)^\lambda dx.$$

Using the transformation $u = e^{-\theta x}$, we write

$$M_X(t) = \int_0^1 \frac{2\lambda\theta u^{-\frac{t}{\theta}}}{1-u^2} \left(\frac{1-u}{1+u} \right)^\lambda du$$

$$= 2\lambda\theta \int_0^1 u^{-\frac{t}{\theta}} (1-u)^{\lambda-1} (1+u)^{-\lambda-1} du.$$

By applying Equation 3.197.3 provided in [44], we obtain the MGF as

$$M_X(t) = B\left(1 - \frac{t}{\theta}, \lambda\right)$$

$$\times {}_2F_1\left(\lambda + 1, 1 - \frac{t}{\theta}; 1 + \lambda - \frac{t}{\theta}; -1\right)$$

where

$$B(a, b) = \int_0^1 t^{a-1} (1-t)^{b-1} dt$$

is the beta function and

$${}_2F_1(a, b; c; z) = \sum_{n=0}^\infty \frac{(a)_n (b)_n}{(c)_n} \cdot \frac{z^n}{n!}$$

is the Gauss hypergeometric function and $(a)_n = a(a+1)\cdots(a+n-1)$.

2.2.3. Quantile Function

The quantile function of the $EG - UEHL(\theta, \lambda)$ distribution is given by

$$Q(u; \theta, \lambda) = \frac{1}{\theta} \log\left(\frac{1+u^{1/\lambda}}{1-u^{1/\lambda}}\right). \quad (6)$$

Equation (6) indicates that the median of the $EG - UEHL(\theta, \lambda)$ distribution is written as

$$Q(0.5; \theta, \lambda) = \frac{1}{\theta} \log\left(\frac{1+0.5^{1/\lambda}}{1-0.5^{1/\lambda}}\right). \quad (7)$$

Additionally, random numbers from the $EG - UEHL(\theta, \lambda)$ can be obtained by using the Equation (6) by the following algorithm:

- S1. Generate a uniform random number from the interval $[0, 1]$.
- S2. Run the quantile function in Equation (6) on the uniform random number in S1.

2.2.3. Stress-Strength Reliability

Stress-strength reliability is denoted as R and is defined by the relation $R = P(Y < X)$, where Y and X represent the stress and strength random variables, respectively. The stress-strength reliability for the $EG - UEHL(\theta, \lambda)$ model is derived using Proposition 1.

Proposition 1. Given Y and X independent stress-strength random variables having $EG - UEHL(\theta, \lambda)$ distribution with parameters (θ, λ_1) and (θ, λ_2) , respectively, the stress-strength reliability is obtained as

$$R = 2\lambda_2 \sum_{j=0}^\infty (-1)^j \left(\binom{\lambda_1 + \lambda_2 + j}{j} B(j+1, \lambda_1 + \lambda_2) \right.$$

$$\left. - \binom{\lambda_2 + j}{j} B(j+1, \lambda_2) \right)$$

Proof:

By definition,

$$R = \int_0^{\infty} \left(1 - \left(\frac{1 - e^{-\theta x}}{1 + e^{-\theta x}} \right)^{\lambda_1} \right) \times \left\{ \frac{2\lambda_2 \theta}{e^{\theta x} - e^{-\theta x}} \left(\frac{1 - e^{-\theta x}}{1 + e^{-\theta x}} \right)^{\lambda_2} \right\} dx \quad (8)$$

By simplifications after substituting $u = e^{-\theta x}$ in Equation (8), we get

$$R = 2\lambda_2 \int_0^1 (1-u)^{\lambda_1 + \lambda_2 - 1} (1+u)^{-\lambda_1 - \lambda_2 - 1} du - 2\lambda_2 \int_0^1 (1-u)^{\lambda_2 - 1} (1+u)^{-\lambda_2 - 1} du \quad (9)$$

Utilizing the binomial expansion as outlined in Equation (9), the stress-strength reliability can be expressed as:

$$R = 2\lambda_2 \sum_{j=0}^{\infty} (-1)^j \binom{\lambda_1 + \lambda_2 + j}{j} B(j+1, \lambda_1 + \lambda_2) - \binom{\lambda_2 + j}{j} B(j+1, \lambda_2)$$

This concludes the proof.

2.2.3. Maximum Likelihood Estimation

Consider X_1, X_2, \dots, X_n as a set of independent and identically distributed samples which are drawn from the $EG - UEHL(\theta, \lambda)$ distribution. The log-likelihood function of the parameters of the distribution is formulated as

$$\ell(\theta, \lambda) = n \log 2 + n \log \lambda + n \log \theta + \lambda \sum_{i=1}^n \log \left(\frac{1 - e^{-\theta x_i}}{1 + e^{-\theta x_i}} \right) - \sum_{i=1}^n \log(e^{\theta x_i} - e^{-\theta x_i}) \quad (10)$$

By taking the derivative of the log-likelihood function presented in Equation (10) concerning the parameters θ and λ , the log-likelihood equations are written, respectively, as

$$\frac{\partial \ell}{\partial \theta} = \frac{n}{\theta} + \lambda \sum_{i=1}^n \left(\frac{2x_i e^{\theta x_i}}{e^{2\theta x_i} - 1} \right) - \sum_{i=1}^n \left(\frac{x_i (e^{2\theta x_i} + 1)}{e^{2\theta x_i} - 1} \right) = 0, \quad (11)$$

and

$$\frac{\partial \ell}{\partial \lambda} = \frac{n}{\lambda} + \sum_{i=1}^n \log \left(\frac{1 - e^{-\theta x_i}}{1 + e^{-\theta x_i}} \right) = 0. \quad (12)$$

Given that the likelihood equations (11) and (12) lack a closed-form solution, we must employ some iterative methods to obtain the maximum likelihood estimates (MLE) for the parameters of the $EG - UEHL(\theta, \lambda)$ distribution. In this study, the 'optim' function in R is utilized to compute these likelihood estimates.

3. Results

This section delves into the properties and efficacy of the proposed $EG - UEHL(\theta, \lambda)$ distribution, utilizing both a computer experiment and an analysis of real-world data.

3.1. Simulation Experiment

A simulation experiment was performed to examine the properties of the Maximum Likelihood Estimators (MLEs), which are discussed in detail in Section 2. Table 1 presents the sample size, n , along with different values of the distribution parameters θ and λ . It also includes the biases and Mean Squared Errors (MSE) of the parameter estimates, derived from 5000 repeated experiments. The data in Table 1 suggests that the MLEs display a positive bias. However, the MLEs of the parameters are asymptotically unbiased. Moreover, as anticipated, the MSEs of the MLEs of the parameters converge to zero as the sample size increases.

3.2. Real - World Dataset Application

In this section, we compare the performance of the $EG - UEHL(\theta, \lambda)$ distribution with the performance of some well-known distributions using a real-world dataset. The data for this study focuses on the maximum flood level of the Susquehanna River in Harrisburg, Pennsylvania. These levels are measured in millions of cubic feet per second (cfs) [45, 46], and it is called the flood data. The performance of the proposed distribution was compared with the Weibull, Beta, Kumaraswamy [35], $UEHL$ and $DUS - UEHL$ [41] distributions. The PDFs for the examined distributions are presented below:

Table 1. Bias and MSEs of MLEs for selected parameter values for the $EG - UEHL(\theta, \lambda)$ distribution.

			Bias		MSE	
θ	λ	n	θ	λ	θ	λ
2	2	50	0.05055	0.13872	0.07496	0.26700
		100	0.02098	0.05780	0.03504	0.10325
		200	0.01128	0.02667	0.01705	0.04482
		300	0.00687	0.01722	0.01108	0.02959
		500	0.00385	0.00889	0.00665	0.01745
0.5	2	50	0.01262	0.13861	0.00468	0.26697
		100	0.00525	0.05781	0.00219	0.10324
		200	0.00283	0.02674	0.00107	0.04481
		300	0.00169	0.01702	0.00069	0.02962
		500	0.00096	0.00891	0.00042	0.01746
2	1.5	50	0.05294	0.09102	0.08372	0.12490
		100	0.02197	0.03793	0.03916	0.04963
		200	0.01185	0.01738	0.01906	0.02184
		300	0.00715	0.01119	0.01237	0.01446
		500	0.00400	0.00567	0.00740	0.00854

Table 2. Parameter estimates, comparison criteria values and AD test results for the flood data.

	θ	λ	AIC	BIC	-2ℓ	AD (stat)	AD (p-value)
Weibull	3.5259	0.4689	-22.5280	-20.5365	-26.5280	0.8213	0.4643
Beta	6.7565	9.1110	-24.1245	-22.1330	-28.1245	0.7327	0.5302
Kumaraswamy	3.3632	11.7888	-21.7324	-19.7409	-25.7324	0.9321	0.3936
UEHL	3.5050	7.0242	-22.4045	-20.4131	-26.4045	0.8471	0.4467
DUS-UEHL	3.0336	6.6478	-21.7484	-19.7569	-25.7484	0.8648	0.4351
EG-UEHL	11.1194	30.2369	-28.2789	-26.2874	-32.2789	0.2941	0.9420

- Weibull distribution

$$f_{Weibull}(x; \theta, \lambda) = \frac{\theta}{\lambda} \left(\frac{x}{\lambda}\right)^{\theta-1} e^{-(x/\lambda)^\theta}, \theta, \lambda > 0$$

- Beta distribution

$$f_{Beta}(x; \theta, \lambda) = \frac{1}{B(\theta, \lambda)} x^{\theta-1} (1-x)^{\lambda-1}, \theta, \lambda > 0$$

- Kumaraswamy distribution

$$f_{Kw}(x; \theta, \lambda) = \theta \lambda x^{\theta-1} (1-x^\theta)^{\lambda-1}, \theta, \lambda > 0$$

- DUS - UEHL distribution

$$f_{DUS-UEHL}(x) = \frac{1}{e-1} 2\lambda \theta x^{\theta-1} \frac{(1-x^\theta)^{\lambda-1}}{(1+x^\theta)^{\lambda+1}} e^{1-\left(\frac{1-x^\theta}{1+x^\theta}\right)^\lambda}, \theta, \lambda > 0.$$

We use the maximum likelihood method to estimate the parameters of all compared distributions. The goodness-of-fit for each model is evaluated using the Anderson-Darling test statistic (A-D (stat)) and its corresponding p-value (A-D (p-value)). To assess the models' relative performance, we consider the log-likelihood, Akaike information criterion (AIC), and Bayesian information criterion (BIC). The formulas for calculating AIC and BIC are presented below:

$$AIC = 2m - 2\ell(\theta, \lambda) \quad \text{and} \quad BIC = m \log n - 2\ell(\theta, \lambda)$$

Here, m represents the number of parameters, n is the sample size of the dataset, and ℓ is the maximum value of the likelihood function for the respective distribution.

The maximum likelihood estimates, information criteria and goodness-of-fit results for all the models for flood data are given in Table 2. According to the A-D (stat) and A-D (p-value) in Table 2, the compared distributions

offer a good fit for modeling the flood data. Table 2 shows that the $EG - UEHL(\theta, \lambda)$ model gives the smallest -2ℓ , AIC and BIC values. The $EG - UEHL(\theta, \lambda)$ is followed by the beta and Weibull distributions in terms of these criteria. Hence, the $EG - UEHL(\theta, \lambda)$ model stands out among its competitors due to its exceptional performance in modeling the flood data. Also, Figure 2 visually presents the empirical and fitted curves derived from the flood data.

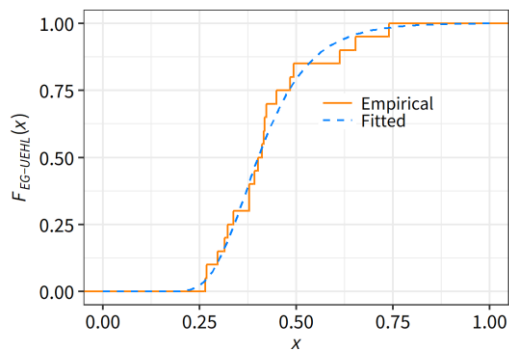


Figure 3. The distribution functions for the flood dataset (smooth: empirical, dashed: fitted)

4. Conclusion

This paper is based on the principle of enhancing the performance of a unit distribution through a G-family transformation. Particularly, the paper introduces a novel statistical distribution, the $EG - UEHL(\theta, \lambda)$, built upon the G-family transformation. This new distribution exhibits enhanced functional capabilities and a strengthened mathematical structure. We delve into the distribution's key characteristics, including moments, the moment-generating function, the quantile function, and its relevance to stress-strength reliability analysis. These explorations offer a thorough understanding of the $EG - UEHL(\theta, \lambda)$ distribution, opening doors for both theoretical advancements and applications in various practical settings.

To investigate the behavior of the proposed distribution's parameter estimates, we conducted a computer simulation. Additionally, we compared the performance of the EG-UEHL model against established models using real-world data. The real-data analysis revealed that the EG-UEHL model outperforms the other models according to the AIC and BIC criteria.

Author's Contributions

Murat Genç presented the research idea, authored the manuscript, established the theoretical framework, and conducted the data analysis.

Ömer Özbilen analytically examined the structure, conducted a supporting role in data analysis, interpreted findings, and facilitated manuscript preparation.

Ethics


The authors have ensured that the manuscript adheres to all ethical considerations.

References

- [1]. Al-Babtain, AA, Elbatal, I, Chesneau, C, Elgarhy, M. 2020. Sine Topp-Leone-G family of distributions: Theory and applications. *Open Physics*; 18(1): 574-593.
- [2]. Hussein, M, Cordeiro, GM, De Santana, LH, Rodrigues, GM, Ortega, EM. 2022. Odd Pareto-G Family: Properties, Regression, Simulations and Applications. *Contemporary Mathematics*; 4(1): 49-74.
- [3]. Gabanakgosi, M, Oluyede, B. 2023. The Topp-Leone type II exponentiated half logistic-G family of distributions with applications. *International Journal of Mathematics in Operational Research*; 25(1): 85-117.
- [4]. Carrasco, JM, Ortega, EM, Cordeiro, GM. 2008. A generalized modified Weibull distribution for lifetime modeling. *Computational Statistics & Data Analysis*; 53(2): 450-462.
- [5]. Almalki, SJ, Nadarajah, S. 2014. Modifications of the Weibull distribution: A review. *Reliability Engineering & System Safety*; 124: 32-55.
- [6]. Johnson, NL. 1949. Systems of frequency curves generated by methods of translation. *Biometrika*; 36: 149-176.
- [7]. Tadikamalla, PR, Johnson, NL, 1982. Systems of frequency curves generated by transformations of logistic variables, *Biometrika*; 69: 461-465.
- [8]. Korkmaz, MÇ. 2020. A new heavy-tailed distribution defined on the bounded interval: The logit slash distribution and its application, *Journal of Applied Statistics*; 47: 2097-2119.
- [9]. Gündüz, S, Korkmaz, MÇ. 2020. A new unit distribution based on the unbounded johnson distribution rule: The unit johnson su distribution, *Pakistan Journal of Statistics and Operation Research*; 16: 471-490.
- [10]. Altun, E, Hamedani, G. 2018. The log-xgamma distribution with inference and application, *Journal of the French Statistical Society*; 159: 40-55.
- [11]. Mazucheli, J, Menezes, AFB, Ghitany, ME. 2018. The unit-Weibull distribution and associated inference. *Journal of Applied Probability and Statistics*; 13(2): 1-22.
- [12]. Mazucheli, J, Menezes, AF, Dey, S. 2018. The unit-Birnbaum-Saunders distribution with applications. *Chilean Journal of Statistics*; 9(1): 47-57.
- [13]. Ghitany, ME, Mazucheli, J, Menezes, AFB, Alqallaf, F. 2019. The unit-inverse Gaussian distribution: A new alternative to two-parameter distributions on the unit interval. *Communications in Statistics-Theory and methods*; 48(14): 3423-3438.
- [14]. Altun, E. 2021. The log-weighted exponential regression model: alternative to the beta regression model. *Communications in Statistics-Theory and Methods*; 50(10): 2306-2321.
- [15]. Sindhu, TN, Shafiq, A, Huassian, Z. 2024. Generalized exponentiated unit Gompertz distribution for modeling arthritic pain relief times data: classical approach to statistical inference. *Journal of Biopharmaceutical Statistics*; 34(3): 323-348.

- [16]. Dombi, J, Jonas, T, Toth, ZE, Arva, G. 2019. The omega probability distribution and its applications in reliability theory. *Quality and Reliability Engineering International*; 35(2): 600-626.
- [17]. Özbilen, Ö, Genç, Aİ. 2022. A bivariate extension of the omega distribution for two-dimensional proportional data. *Mathematica Slovaca*; 72(6): 1605-1622.
- [18]. Seo, JI, Kang, SB. 2015. Notes on the exponentiated half logistic distribution. *Applied Mathematical Modelling*; 39(21): 6491-6500.
- [19]. Gui, W. 2017. Exponentiated half logistic distribution: Different estimation methods and joint confidence regions. *Communications in Statistics-Simulation and Computation*; 46(6): 4600-4617.
- [20]. Kang, SB, Seo, JI. 2011. Estimation in an Exponentiated Half Logistic Distribution under Progressively Type-2 Censoring. *Communications for Statistical Applications and Methods*; 18(5): 657-666.
- [21]. Rastogi, MK, Tripathi, YM. 2014. Parameter and reliability estimation for an exponentiated half-logistic distribution under progressive type II censoring. *Journal of Statistical Computation and Simulation*; 84(8): 1711-1727.
- [22]. Ali, MM, Ali, I, Yousof, HM, Ahmed, MIM. 2023. *G Families of Probability Distributions: Theory and Practices*. CRC Press.
- [23]. Tahir, MH, Nadarajah, S. 2015. Parameter induction in continuous univariate distributions: Well-established G families. *Anais da Academia Brasileira de Ciências*; 87: 539-568.
- [24]. Bourguignon, M, Silva, RB, Cordeiro, GM. 2014. The Weibull-G family of probability distributions. *Journal of Data Science*; 12(1): 53-68.
- [25]. Shukla, AK, Soni, S, Kumar, K. 2023. An inferential analysis for the Weibull-G family of distributions under progressively censored data. *OPSEARCH*; 60: 1488-1524.
- [26]. Tahir, M, Zubair, M, Mansoor, M, Cordeiro, GM, Alizadeh M, GG, H. 2016. A new Weibull-G family of distributions. *Hacetatepe Journal of Mathematics and statistics*; 45(2): 629-647.
- [27]. Korkmaz, MÇ. 2018. A new family of the continuous distributions: the extended Weibull-G family. *Communications Faculty of Sciences University of Ankara Series A1 Mathematics and Statistics*; 68(1): 248-270.
- [28]. Alizadeh, M, Cordeiro, GM, Pinho, LGB, Ghosh, I. 2017. The Gompertz-G family of distributions. *Journal of statistical theory and practice*; 11: 179-207.
- [29]. Badr, MM, Elbatal, I, Jamal, F, Chesneau, C, Elgarhy, M. 2020. The transmuted odd Fréchet-G family of distributions: Theory and applications. *Mathematics*; 8(6): 958.
- [30]. Ul Haq, MA, Elgarhy, M. 2018. The Odd Fréchet-G family of probability distributions. *Journal of Statistics Applications & Probability*; 7(1): 189-203.
- [31]. Eghwerido, JT, Efe-Eyefia, E, Zelibe, SC. 2021. The transmuted alpha power-G family of distributions. *Journal of Statistics and Management Systems*; 24(5): 965-1002.
- [32]. Chakraborty, S, Handique, L, Jamal, F. 2022. The Kumaraswamy Poisson-G family of distribution: its properties and applications. *Annals of Data Science*; 9(2): 229-247.
- [33]. Alnssyan, B, Hussein, EA, Alizadeh, M, Afify, AZ, Abdellatif, AD. 2023. The weighted Lindley-G family of probabilistic models: properties, inference, and applications to real-life data. *Journal of Intelligent & Fuzzy Systems*; 44(5): 8071-8089.
- [34]. Mazucheli, J, Menezes, AFB, Fernandes, LB, De Oliveira, RP, Ghitany, ME. 2020. The unit-Weibull distribution as an alternative to the Kumaraswamy distribution for the modeling of quantiles conditional on covariates. *Journal of Applied Statistics*; 47(6): 954-974.
- [35]. Kumaraswamy, P. 1980. A generalized probability density function for double-bounded random processes. *Journal of hydrology*; 46(1-2): 79-88.
- [36]. Guerra, RR, Peña-Ramírez, FA, Bourguignon, M. 2021. The unit extended Weibull families of distributions and its applications. *Journal of Applied Statistics*; 48(16): 3174-3192.
- [37]. Chakraborty, S, Ong, SH, Ng, CM. 2023. A new probability model with support on unit interval: Structural properties, regression of bounded response and applications. *Journal of Statistical Theory and Practice*; 17(4): 1-32.
- [38]. Masood, B, Bashir, S, Masood, N. 2023. Unit Interval Exponentiated Exponential Distribution and Quantile Regression Model: Applications for the COVID-19 Data and Bounded Responses Data. *Annals of Human and Social Sciences*; 4(4): 51-66.
- [39]. Korkmaz, MÇ, Korkmaz, ZS. 2023. The unit log-log distribution: A new unit distribution with alternative quantile regression modeling and educational measurements applications. *Journal of Applied Statistics*; 50(4): 889-908.
- [40]. Akata, IU, Opone FC, Osagiede, FEU. 2023. The Kumaraswamy Unit-Gompertz Distribution and its Application to Lifetime Datasets. *Earthline Journal of Mathematical Sciences*; 11(1): 1-22.
- [41]. Genç, M, Özbilen, Ö. 2023. An Extension of the UEHL Distribution Based on the DUS Transformation. *Journal of New Theory*; 44: 20-30.
- [42]. Genç, M, Özbilen, Ö. 2023. Exponentiated UEHL Distribution: Properties and Applications. *Recep Tayyip Erdoğan Üniversitesi Fen Ve Mühendislik Bilimleri Dergisi*; 4(2): 232-241.
- [43]. Nadarajah, S. 2005. Exponentiated beta distributions. *Computers & Mathematics with Applications*; 49(7-8): 1029-1035.
- [44]. Gradshteyn, IS, Ryzhik, IM. 2007. *Table of integrals, series, and products*, 7th edition dü.. San Diego: Academic press.
- [45]. Dumonceaux, R, Antle, CE. 1973. Discrimination between the log-normal and the Weibull distributions. *Technometrics*; 15(3): 923-926.
- [46]. Bantan, RAR, Chesneau, C, Jamal, F, Elgarhy, M, Almutiry, W, Alahmadi, AA. 2021. Study of a Modified Kumaraswamy Distribution. *Mathematics*; 9(21): 2836.

The Impact of Image Reconstruction Parameters on TARE Treatment Dosimetric Calculation

Bilal Kovan^{1*} , Emine Gökür Işık¹ 

¹ Istanbul University, Istanbul Faculty of Medicine, Department of Nuclear Medicine, Istanbul, Türkiye

*bkovan@istanbul.edu.tr

* Orcid No: 0000-0002-4431-8358

Received: 4 May 2024

Accepted: 7 June 2024

DOI: 10.18466/cbayarfb.1478468

Abstract

Accurate dosimetric calculations are essential to enhance therapeutic efficacy in Yttrium-90 (Y-90) microsphere therapy, which rely significantly on the three-dimensional imaging parameters used. This study aims to evaluate the reconstruction parameters used to generate three-dimensional images from SPECT data obtained for dosimetric calculations, and to determine the optimal reconstruction parameters. This retrospective study evaluated Single Photon Emission Computed Tomography/Computed Tomography (SPECT/CT) images of 30 patients (8 women and 22 men) who underwent Transarterial Radioembolization (TARE) treatment at our clinic between 2018 and 2019 using Technetium 99mTc-labeled macroaggregated albumin (99mTc-MAA). The SPECT images were reconstructed using 20 different iterations and subset values. The perfused areas were identified using 5% and 10% threshold values. At the 5% threshold, the maximum difference from the average was 20.7% at 2 iterations and 2 subsets. For other parameters, the difference from the average was less than 2.8%. At the 10% threshold, the maximum difference from the average was 14.8% at 2 iterations and 2 subsets, with other parameters again showing a difference of less than 2.8%. For effective TARE treatment, it is recommended to set the SPECT image reconstruction parameters to higher than 5 iterations and 5 subsets following the administration of 99mTc-MAA.

Keywords: Dosimetry, Iteration, Subset, Radioembolization, SPECT

1. Introduction

Selective Internal Radiation Therapy (SIRT), also known as Yttrium-90 (Y-90) microsphere transarterial radioembolization (TARE), is an established and promising treatment modality for primary liver tumors and liver metastases [1, 2]. The objective of TARE treatment is to deliver the maximum radiation dose to the tumors while minimizing exposure to the healthy parenchymal tissue [3]. In TARE treatment, radioactive microspheres are injected into the tumor region through the arteries that feed the tumor [4]. A pre-treatment evaluation is conducted to determine the patient's suitability for the treatment. Due to 90Y being a pure beta emitter, the treatment evaluation utilizes Technetium 99mTc-labeled macroaggregated albumin (99mTc-MAA) which mimics the microspheres [4]. This evaluation is crucial for determining the risk of lung shunting, controlling gastric leakage, and, most importantly, for dose planning [5-7]. After the

administration of 99mTc-MAA, whole-body and Single Photon Emission Computed Tomography/Computed Tomography (SPECT/CT) imaging of the patient should be performed as soon as possible [8]. Using the obtained images, patient suitability is assessed and the dose to be administered is calculated. Scientific studies have shown that personalized dosimetry calculations significantly affect TARE treatment's effectiveness [1, 9]. In the international multicenter study conducted by Lam et al. and the European Association of Nuclear Medicine (EANM) treatment guideline, it was stated that dosimetric calculation should be made in TARE treatment and that dosimetry increases the effectiveness of treatment.

Despite not being fully standardized, dosimetric calculation protocols in Nuclear Medicine therapeutic applications are continually being refined through numerous scientific studies. Recently, international bodies have published dosimetry guidelines for nuclear medicine treatments [10-12]. All guidelines advocate

using the Medical Internal Radiation Dose (MIRD) formula for calculations [12, 13]. Data derived from patient imaging are used in the MIRD formula. For error-free dosimetry, imaging protocols and image formation parameters must be tailored to the specific application. The EANM guidelines offer recommendations for SPECT/CT and Positron Emission Tomography (PET)/CT imaging post-procedure and treatment [12]. These guidelines specify parameters that should be used during imaging: low-energy collimators, matrix sizes of 256×256 or 128×128 , an energy window centered at 140 keV with a 15% width for the main peak, adjacent scatter energy windows, 30-degree projection angles, and a minimum of 15 seconds per projection. Detailed information regarding the parameters necessary for three-dimensional image reconstruction is not provided. The EANM guidelines emphasize the need for optimization in voxel dosimetry, suggesting that the number of iterations and subsets typically used for diagnostic purposes should be higher.

The aim of this study is to determine how different iteration and subset values used in image reconstruction of TARE treatment evaluation images affect dosimetric calculations and to establish the optimal reconstruction parameters for TARE treatment evaluations.

2. Materials and Methods

2.1 Patients and Sample Collection

The collection of human samples for this study was approved by the Ethics Committee of the Istanbul Medical Faculty (Protocol number: 2024/918).

This retrospective study included 30 patients treated with ^{99m}Tc -MAA and underwent Hepatic Artery Perfusion Scintigraphy (HAPS) at our clinic during the years 2018-2019, consisting of 8 women and 22 men. The inclusion criteria were patients older than 18 years, suitable for TARE treatment without any contraindications in mapping scintigraphy.

2.2 Hepatic Artery Perfusion Scintigraphy Data Acquisition

An hour after administering 185-222 MBq/5 ml of ^{99m}Tc -labeled macro aggregated albumin (MAA) for simulation angiography ahead of Transarterial Radioembolization (TARE) treatment with Therasphere from BTG International Ltd., Ottawa, Canada, whole-body anterior and posterior planar imaging was conducted using a GE Discovery NM 670 SPECT/CT system (General Electric Healthcare, Waukesha, WI, USA). Equipped with a low-energy high-resolution (LEHR) collimator and a primary energy peak of 140.5 keV ($\pm 10\%$), the system utilized a window gap set to a 128×128 matrix, with imaging parameters established at 13 cm/min. Subsequently, SPECT imaging was performed on both lung and abdominal regions,

employing a primary energy peak of 140.5 keV ($\pm 10\%$) and a scatter peak of 120 keV ($\pm 5\%$), comprising 60 frames captured over 20 seconds each. Following SPECT imaging, a CT scan of the same regions ensued, facilitating anatomical correlation and attenuation correction, with settings at 120 keV and 100 mAs.

2.3 Image Reconstruction

The acquired SPECT and CT data were processed using the ordered-subset expectation maximization (OSEM) method, using the Butterworth filter and CT-based attenuation correction. Image processing has been reconstructed using iteration-subset values are respectively; 2-2 (C1), 2-5 (C2), 2-10 (C3), 2-20 (C4), 5-5 (C5), 5-10 (C6), 5-15 (C7), 5-20 (C8), 10-5 (C9), 10-10 (C10), 10-15 (C11), 10-20 (C12), 15-5 (C13), 15-10 (C14), 15-15 (C15), 15-20 (C16), 20-5 (C17), 20-10 (C18), 20-15 (C19) and 20-20 (C20).

2.4 Data Analysis

All image analyses were conducted using the Mirada DBx 1.2.0 and Simlicit90Y dosimetry software. The volume and count values of the perfused areas were determined using threshold values of 5% and 10%. The changes in these values according to different iteration and subset changes were analyzed.

2. Results and Discussion

The volumes of perfused areas at the 5% threshold were presented in Table 1, and at the 10% threshold in Table 2. The counts of perfused areas at the 5% threshold were presented in Table 3, and at the 10% threshold in Table 4. Considering these values, the average perfused area volumes at 5% threshold for the thirty patients according to configurations C1 through C20 were as follows: 1043.3, 884.1, 860.7, 844.6, 860.6, 856.5, 863.4, 846.6, 858.4, 851.9, 858.8, 841.9, 858.3, 850.1, 856.4, 840.3, 858.3, 852.7, 858.8, and 841.5 cm^3 , respectively. The greatest variance from the average was 20.7% observed in C1, while other configurations showed differences of less than 2.8%. The counts were as follows: 5,082,759, 5,658,949, 5,664,377, 5,595,932, 5,710,880, 5,680,083, 5,554,952, 5,597,601, 5,717,349, 5,683,208, 5,559,058, 5,601,691, 5,718,115, 5,682,599, 5,557,861, 5,599,595, 5,725,705, 5,686,537, 5,561,944, and 5,628,692. The highest variance from the average count was 9.5% in C1, with other configurations showing less than 2%.

For the 10% threshold, the perfused area volumes for C1 through C20 were as follows: 722, 648, 630, 615, 634, 624, 624, 609, 632, 626, 622, 611, 631, 623, 622, 611, 630, 623, 622, and 612 cm^3 , respectively. The greatest difference from the average was 14.8% for C1, with other configurations showing differences of less than 2.8%. The counts were as follows: 4,566,302, 5,050,578, 5,058,360, 4,991,871, 4,983,310, 5,037,283, 5,086,541,

4,989,636, 5,109,255, 5,077,754, 4,937,672, 4,991,870, 5,109,296, 5,078,857, 5,071,626, 4,994,661, 5,114,986, 5,077,171, 5,057,384, and 4,991,746. The highest difference from the average count was 9% in C1, with other configurations showing differences of less than 1.9%.

Regarding the distribution of perfused area sizes for the 10% threshold: 12 patients had areas under 500 cm³, 11 patients between 500 cm³ and 1000 cm³, and 7 patients had areas over 1000 cm³. The greatest difference from the average volume for areas under 500 cm³ was 4.7% at C8 for the 10% threshold, with other configurations showing differences of less than 4.6%. At the 5% threshold, the greatest difference was 10.7% in C1, with other configurations showing differences of less than 3.8%. Count variances were 9.2% at the 5% threshold and 10.2% at the 10% threshold for C1.

For patients with perfused areas between 500 and 1000 cm³, the greatest difference from the average volume was 11.5% at C1 for the 10% threshold, with other configurations showing differences of less than 3.6%. At the 5% threshold, the greatest difference was 17.8% at C1, with other configurations showing differences of less than 3.7%. Count variances were 10.4% at the 5% threshold and 18.2% at the 10% threshold for C1.

For patients with perfused areas over 1000 cm³, the greatest difference from the average volume was 18.9% at C1 for the 10% threshold, with other configurations showing differences of less than 4%. At the 5% threshold, the greatest difference was 25.3% at C1, with other configurations showing differences of less than 3.1%. Count variances were 8.4% at the 5% threshold and 8.9% at the 10% threshold for C1.

Recent years have seen an acceleration in research focusing on the importance of dosimetry and its contribution to the efficacy of TARE treatment. The acquisition parameters for SPECT imaging and reconstruction, particularly for voxel-based dosimetry, are crucial. International authorities emphasize the need for well-defined imaging acquisition and reconstruction parameters, which directly affect treatment effectiveness.

In this study, following the administration of 99mTc-MAA for TARE treatment, the impact of image reconstruction parameters on perfused areas and counts was investigated. Variations were observed with different iteration and subset values. The highest deviation from the average in perfused areas was found in images with 2 iterations and 2 subsets at both 5% and 10% threshold values, where the perfused area values were calculated to be 20.7% and 14.8% higher than average, respectively. This suggests a potential increase of up to 20.7% in the treatment dose applied to patients. For images with 2 iterations and 5 subsets, the increase was 2.3% at a 5% threshold and 3.1% at a 10% threshold. Other iteration and subset values calculated perfused areas closely together. It was found that while the number

of iterations did not change the perfused area, increasing the subset value tended to decrease the perfused area by approximately 3%.

When examining changes between iteration and subset values in counts, a 9.5% and 9% decrease from the average was detected in images with 2 iterations and 2 subsets at 5% and 10% thresholds, respectively. The counts in other values were closely aligned. These results indicate that settings below 5 iterations and 5 subsets tend to provide a high perfused area with a low count.

The relationship between the size of the perfused area and the changes in the perfused area and count ratios was also examined. Among the patients, 12 had a perfused area smaller than 500 cm³ (Group 1), 11 had between 500 cm³ and 1000 cm³ (Group 2), and 7 had more than 1000 cm³ (Group 3). The findings indicate minor deviations in Group 1, while deviations increased in Groups 2 and 3, particularly in configurations C1 and C2, correlating the size of the perfused area with the deviation observed.

No similar studies exist for imaging post 99mTc-MAA application in TARE treatment. However, several studies are available on imaging acquisition parameters and image reconstruction for scattering and attenuation correction. Research evaluating iteration and subset values in post-treatment imaging with 90Y has been conducted [14, 15]. A study by Linder et al. explored post-treatment PET imaging parameters with 90Y, reporting the best results with 2 iterations and 5 subsets, a 4 mm filter, and a 20-minute scanning time [14]. Considering 90Y's pure beta emission and the imaging being conducted with bremsstrahlung radiation, our study results differ. Costa and colleagues also performed phantom and patient imaging with 90Y using two different PET machines [15], utilizing OSEM, 4 iterations, and 20 subsets, which were deemed suitable for dosimetry.

In a phantom study by Cheenu Kappadath, diagnostic imaging reconstruction parameters with 99mTc were evaluated. Images obtained with different iteration and subset values were compared, finding that high-background images performed best with 20 iterations and 18 subsets, while no-background images were optimal with 10 iterations and 18 subsets [16]. He also emphasized that the specificity of iterative reconstruction parameters (iterations, subsets, and filtering) affects the quantitative outcome in SPECT, dependent on the nature of activity distribution within the SPECT field of view. His study, parallel to ours, recommended high iteration and subset values.

Our study shows that low iteration and subset values increase perfused area while decreasing counts, dependent on the size of the perfused area. It was determined that volume and count values do not change when iteration and subset values are above 5.

Recent studies emphasize the benefits of voxel-based dosimetric calculation for TARE treatments [17-19]. In voxel-based dosimetry, calculations are made based on activity distribution. Activity distribution is determined by the counts in SPECT images. In the study conducted by Coskun et al., treatment response was evaluated with voxel-based dosimetry and dose-volume histograms, and they emphasized that treatment response could be predicted with voxel-based dosimetry [20]. This shows that count and distribution are important in SPECT data in voxel-based dosimetry. It was observed that the counting rates decreased especially in low iteration and low subset values, and this rate increased especially in large volumes. It was observed that background decreased as the iteration and subset value increased. These results show that iteration and subset values will affect voxel-based dosimetry.

3. Conclusion

In the conclusion, the effect of reconstruction on dosimetry calculations is significant. We recommend setting SPECT image reconstruction parameters higher than 5 iterations and 5 subsets following the administration of ^{99m}Tc -MAA for TARE treatment.

Author's Contributions

Bilal Kovan: Drafted and wrote the manuscript, performed the experiment and result analysis.

Emine Göknuş Işık: Performed the experiment and result analysis.

Acknowledgement

There are no financial declarations. This work is not grant funded.

Ethics

The collection of human samples for this study was approved by the Ethics Committee of the Istanbul Medical Faculty (Protocol number: 2024/918).

References

- [1] Lam M, Garin E, et al. A global evaluation of advanced dosimetry in transarterial radioembolization of hepatocellular carcinoma with Yttrium-90: the TARGET study. *European Journal of Nuclear Medicine and Molecular Imaging*. 2022;49:3340-52.
- [2] Ramdhani K, Braat A. The Evolving Role of Radioembolization in the Treatment of Neuroendocrine Liver Metastases. *Cancers*. 2022;14.
- [3] Mikell JK, Dewaraja YK, et al. Transarterial Radioembolization for Hepatocellular Carcinoma and Hepatic Metastases: Clinical Aspects and Dosimetry Models. *Seminars in radiation oncology*. 2020;30:68-76.
- [4] Weber M, Lam M, et al. EANM procedure guideline for the treatment of liver cancer and liver metastases with intra-arterial

radioactive compounds. *European Journal of Nuclear Medicine and Molecular Imaging*. 2022;49:1682-99.

[5] Kovan B, Civan C, et al. Influencing factors of lung shunt fraction in transarterial radioembolization treatment. *Clinical and Translational Imaging*. 2024, 12.2: 205-211.

[6] Yilmaz E, Engin MN, et al. Y90 selective internal radiation therapy and peptide receptor radionuclide therapy for the treatment of metastatic neuroendocrine tumors: combination or not? *Nuclear Medicine Communications*. 2020;41:1242-9.

[7] Abuqbeith M, Demir M. Effect of predicted lung mass versus fixed mass regimes on lung dose in SIRT (90Y). *International Journal of Computational and Experimental Science and Engineering*. 2024;10.

[8] Kovan B, Denizmen D, et al. Influence of Early Versus Delayed Hepatic Artery Perfusion Scan on (90Y) Selective Internal Radiation Therapy Planning. *Cancer Biotherapy and Radiopharmaceuticals*. 2024.

[9] Guiu B, Garin E, et al. TARE in Hepatocellular Carcinoma: From the Right to the Left of BCLC. *Cardiovascular Interventional Radiology*. 2022;45:1599-607.

[10] Busse NC, Al-Ghazi MS, et al. AAPM Medical Physics Practice Guideline 14. a: Yttrium-90 microsphere radioembolization. *Journal of Applied Clinical Medical Physics*. 2024;25:e14157.

[11] Dezar WA, Cessna JT, et al. Recommendations of the American Association of Physicists in Medicine on dosimetry, imaging, and quality assurance procedures for 90Y microsphere brachytherapy in the treatment of hepatic malignancies. *Medical Physics*. 2011;38:4824-45.

[12] Chiesa C, Sjogreen-Gleisner K, et al. EANM dosimetry committee series on standard operational procedures: a unified methodology for (99m)Tc-MAA pre- and (90Y) peri-therapy dosimetry in liver radioembolization with (90Y) microspheres. *EJNMMI Physics*. 2021;8:77.

[13] Marquis H, Ocampo Ramos JC, et al. MIRD Pamphlet No. 29: MIRDy90-A (90Y) Research Microsphere Dosimetry Tool. *Journal of Nuclear Medicine*. 2024.

[14] Linder PM, Lan W, et al. Optimization of Y-90 Radioembolization Imaging for Post-Treatment Dosimetry on a Long Axial Field-of-View PET/CT Scanner. *Diagnostics*. 2023;13.

[15] Costa G, Spencer B, et al. Radioembolization Dosimetry with Total-Body (90Y) PET. *Journal of Nuclear Medicine*. 2022;63:1101-7.

[16] Kappadath SC. Effects of voxel size and iterative reconstruction parameters on the spatial resolution of ^{99m}Tc SPECT/CT. *Journal of Applied Clinical Medical Physics*. 2011;12:3459.

[17] Orcajo Rincón J, Regi AR, et al., "Maximum tumor-absorbed dose measured by voxel-based multicompartamental dosimetry as a response predictor in yttrium-90 radiation segmentectomy for hepatocellular carcinoma," (in eng), *EJNMMI Physics*, vol. 10, no. 1, p. 7, Feb 6 2023, doi: 10.1186/s40658-022-00520-9.

[18] Villalobos A, Arndt L, et al., "Yttrium-90 Radiation Segmentectomy of Hepatocellular Carcinoma: A Comparative Study of the Effectiveness, Safety, and Dosimetry of Glass-Based versus Resin-Based Microspheres," (in eng), *Journal of Vascular and Interventional Radiology*, vol. 34, no. 7, pp. 1226-1234, Jul 2023, doi: 10.1016/j.jvir.2023.02.030.

[19] Yoo M. Y., Paeng JC, et al., "Efficacy of voxel-based dosimetry map for predicting response to trans-arterial radioembolization therapy for hepatocellular carcinoma: a pilot study," (in eng), *Nuclear Medicine Communications*, vol. 42, no. 12, pp. 1396-1403, Dec 1 2021, doi: 10.1097/mnm.0000000000001471.



[20] Coskun N, Kartal MO, et al., "Use of dose-volume histograms for metabolic response prediction in hepatocellular carcinoma patients undergoing transarterial radioembolization with Y-90 resin microspheres," (in eng), *Annals of Nuclear Medicine*, Apr 22 2024, doi: 10.1007/s12149-024-01926-4.



Appendix

Table 1. Volumes (cm³) with 5% threshold in all configurations.

Patient No	C1	C2	C3	C4	C5	C6	C7	C8	C9	C10	C11	C12	C13	C14	C15	C16	C17	C18	C19	C20
1	357	315	312	335	312	312	301	314	306	325	303	324	309	315	303	324	311	312	316	315
2	213	205	209	200	207	210	214	200	207	211	214	200	207	211	214	200	207	211	214	200
3	234	209	221	195	206	221	206	195	206	222	206	196	207	223	206	196	207	223	206	195
4	137	120	117	117	120	117	119	117	120	117	119	117	120	116	119	117	120	117	119	117
5	97	89	101	91	90	91	90	101	91	91	90	101	90	91	90	98	90	91	90	97
6	194	162	160	158	159	160	158	158	159	160	159	159	159	160	158	159	159	160	159	159
7	334	301	279	247	311	283	323	244	314	285	326	244	315	287	326	244	316	287	326	244
8	270	225	214	217	219	214	216	217	218	214	216	217	219	215	217	216	219	215	217	216
9	68	63	61	57	64	61	61	57	65	62	61	57	64	62	61	57	64	62	61	57
10	471	463	455	454	479	459	493	453	480	460	494	454	480	460	494	455	480	461	493	456
11	441	398	395	387	398	397	398	388	399	397	398	388	400	396	400	387	400	397	400	387
12	227	207	204	201	205	204	201	202	205	205	202	202	205	205	202	202	206	205	202	202
13	1115	943	894	834	876	867	993	833	860	867	998	833	859	870	996	833	860	870	996	822
14	951	847	807	760	816	806	828	764	816	807	804	761	817	807	804	764	796	808	803	763
15	815	695	689	660	682	691	695	645	678	688	694	662	685	691	698	663	688	697	699	664
16	977	862	847	845	842	844	837	850	839	844	837	851	839	845	837	850	840	846	835	851
17	763	667	658	678	559	662	667	676	663	662	667	673	671	661	667	674	672	660	667	674
18	1147	943	893	834	876	867	993	833	860	867	998	833	859	870	996	833	860	870	996	833
19	1285	1114	1083	1065	1081	1062	1065	1056	1069	1061	1061	1056	1066	1061	1061	1056	1067	1058	1061	1056
20	1154	1022	1014	1009	1021	1016	1034	1008	1022	1015	1035	1008	1022	1015	1034	1008	1024	1016	1035	1003
21	1095	941	906	883	930	901	880	881	932	902	881	877	933	901	881	878	934	897	882	878
22	2072	1727	1680	1683	1684	1667	1668	1678	1674	1667	1668	1678	1672	1664	1666	1678	1670	1664	1665	1681
23	2458	1952	1861	1879	1897	1862	1866	1873	1893	1861	1850	1856	1874	1860	1834	1856	1874	1844	1833	1855
24	1834	1565	1484	1516	1521	1482	1441	1515	1517	1483	1446	1514	1516	1483	1446	1514	1516	1483	1446	1518
25	1859	1575	1546	1537	1536	1539	1547	1533	1534	1541	1548	1536	1536	1540	1547	1532	1536	1541	1543	1533
26	1411	1268	1230	1214	1245	1220	1210	1211	1234	1217	1214	1210	1232	1217	1214	1204	1232	1218	1214	1203
27	2952	2503	2428	2388	2410	2382	2349	2354	2404	2381	2310	2362	2404	2382	2310	2353	2404	2383	2313	2377
28	2949	2168	2056	2040	2075	2049	2041	2019	2085	2049	2046	2016	2088	2054	2041	2015	2088	2059	2045	2016
29	1387	1229	1214	1114	1217	1211	1207	1201	1213	1210	1206	1201	1205	1209	1206	1162	1204	1210	1207	1193
30	2032	1747	1804	1742	1783	1839	1800	1822	1689	1686	1716	1673	1695	1634	1665	1684	1707	1720	1723	1683
Mean	1043	884	861	845	861	857	863	847	858	852	859	842	858	850	856	840	858	853	859	842

C: Configuration



Table 2. Volumes (cm³) with 10% threshold in all configurations.

Patient No	C1	C2	C3	C4	C5	C6	C7	C8	C9	C10	C11	C12	C13	C14	C15	C16	C17	C18	C19	C20
1	237	217	215	218	215	215	200	211	214	212	202	215	214	222	202	227	216	214	210	227
2	121	118	124	116	121	126	129	116	122	127	130	117	123	127	130	116	123	127	130	116
3	159	150	164	146	152	164	152	147	153	164	152	147	153	165	152	147	152	165	152	147
4	96	89	87	88	90	87	88	88	90	87	88	88	90	87	88	88	90	88	88	88
5	63	61	70	64	63	64	63	71	63	64	63	71	63	64	64	69	63	64	64	68
6	134	120	120	120	120	121	118	120	120	121	119	120	120	121	119	120	120	121	119	120
7	164	143	135	111	143	136	154	111	144	136	155	111	145	137	155	111	145	137	155	111
8	183	170	166	170	169	166	164	169	166	166	163	169	168	166	163	169	168	166	163	169
9	45	44	43	41	44	43	43	41	44	43	43	41	44	43	43	41	44	43	43	40
10	188	187	189	192	196	192	209	194	199	193	210	194	199	193	210	193	199	193	210	193
11	264	251	250	241	250	251	252	242	252	252	252	241	252	251	253	241	253	251	252	241
12	149	142	141	141	143	142	140	142	144	143	141	142	144	143	141	142	144	143	141	142
13	720	624	593	537	579	572	647	531	566	570	648	533	564	571	647	533	564	570	647	533
14	606	557	529	478	545	519	540	476	531	519	528	474	531	519	527	475	520	520	528	475
15	570	529	530	512	526	528	532	508	525	530	533	513	525	530	534	514	525	531	535	514
16	664	604	599	594	592	599	599	600	592	598	598	600	593	599	599	600	593	599	598	601
17	543	504	499	514	510	499	506	511	509	498	507	511	510	497	508	511	510	497	508	511
18	720	624	593	538	579	572	647	532	566	570	648	533	564	571	647	533	564	570	647	533
19	942	892	890	883	889	884	880	878	885	883	878	875	883	883	878	875	883	882	878	875
20	804	758	754	747	764	757	775	745	765	757	777	744	765	758	776	744	766	758	776	744
21	706	627	593	571	625	591	574	568	627	592	575	566	626	593	572	563	627	589	572	563
22	1546	1339	1302	1307	1303	1285	1284	1300	1292	1278	1278	1297	1286	1274	1275	1296	1282	1272	1274	1297
23	1741	1426	1367	1388	1394	1366	1362	1383	1387	1367	1347	1375	1379	1359	1341	1368	1371	1351	1340	1368
24	1360	1223	1149	1188	1205	1151	1111	1092	1206	1153	1114	1191	1207	1153	1113	1190	1208	1156	1115	1192
25	1408	1296	1295	1279	1278	1290	1289	1277	1280	1289	1289	1274	1274	1288	1287	1272	1279	1288	1284	1272
26	939	884	850	842	860	841	833	837	856	840	836	837	857	840	839	833	858	840	839	833
27	2063	1947	1864	1738	1883	1833	1733	1705	1878	1828	1710	1705	1874	1806	1710	1705	1847	1805	1710	1711
28	2040	1643	1539	1497	1564	1515	1487	1481	1553	1514	1484	1482	1552	1512	1483	1481	1551	1511	1483	1481
29	1034	997	990	920	990	982	973	956	986	981	966	955	979	982	966	935	978	981	966	948
30	1448	1271	1247	1263	1232	1241	1246	1242	1229	1291	1241	1221	1251	1247	1245	1239	1250	1266	1250	1240
Mean	722	648	630	615	634	624	624	609	632	626	622	611	631	623	622	611	630	623	622	612

C: Configuration



Table 3. Counts with 5% threshold in all configurations.

Patient No	C1	C2	C3	C4	C5	C6	C7	C8	C9	C10	C11	C12	C13	C14	C15	C16	C17	C18	C19	C20
1	5709444	6213757	6245399	6202018	6258549	6262030	6195192	6183866	6245058	6319060	6203690	6221820	6257946	6278391	6205659	6221199	6270220	6266000	6259788	6187308
2	5933652	6683319	6735070	6940234	6809696	6771455	6707650	6942021	6829010	6779550	6708804	6940794	6830380	6783747	6712714	6943597	6832780	6784342	6712336	6942793
3	2623428	2882474	2865983	2776991	2908121	2875822	2842757	2778683	2912408	2880247	2843441	2780865	2916348	2881733	2842684	2780472	2917272	2881915	2842951	2780251
4	4118512	4477931	4441838	4580624	4508699	4448080	4450214	4585026	4514132	4450482	4450211	4583933	4514016	4449236	4449865	4585346	4514156	4451159	4449669	4584852
5	647087	708895	749869	720056	718065	722125	727919	755556	719148	722754	727957	757643	719166	722854	728432	743024	719479	722546	728137	734318
6	3815546	4134746	4154899	4076060	4158883	4162025	4129047	4079225	4164056	4164813	4130980	4081123	4164849	4164367	4130415	4080040	4166278	4164212	4130965	4081123
7	4426761	4383675	4451215	3230242	4486877	4495272	5885056	3220899	4515732	4511654	5900376	3221426	4526896	4518505	5901526	3220571	4530548	4522090	5903815	3220147
8	1862074	2021630	2054923	1978425	2039369	2061243	2045323	1983252	2043242	2063782	2045720	1980246	2046012	2064265	2045917	1979123	2046852	2064565	2046608	1979025
9	4454448	4828652	4869154	4706963	4872536	4875677	4844999	4714409	4878319	4882331	4843052	4709585	4877915	4882654	4842915	4709789	4878546	4881344	4844228	4709852
10	8174582	9417541	9539452	9523654	9695241	9623541	9785214	9524569	9736214	9635547	9790854	9535625	9747852	9645879	9791325	9547852	9753652	9658541	9788745	9549236
11	5582897	6093425	6161556	5996461	6150416	6192635	6114798	6006785	6174325	6199854	6117854	6008125	6180254	6198745	6123654	6007145	6182456	6200652	6123562	6007545
12	5586398	6264999	6330842	6173155	6321359	6349521	6186025	6182563	6335680	6356048	6198547	6188063	6345896	6359052	6198874	6188095	6345214	6362541	6198797	6183652
13	9616032	10354736	9995623	10124578	10317854	9955602	7414215	10129654	10300306	9966325	7429778	10139547	10302547	9977458	7425412	10132547	10311145	9987632	7425645	10132546
14	670765	731125	737261	750754	734535	740025	747458	751421	736852	741021	742565	750325	737785	741956	742789	750896	733632	741445	742635	750752
15	6988130	7678099	7732654	7666965	7759856	7765645	7809152	7608090	7764125	7767075	7809654	7678109	7785748	7776625	7822415	7681034	7795748	7792013	7823698	7682785
16	4622356	4990125	5043215	4975825	5036251	5063215	5094754	4985632	5042154	5069125	5096325	4985632	5047545	5071021	5096452	4985625	5050565	5073652	5093256	4988965
17	4587676	4931093	4975785	5119232	4985214	4993939	5096541	5112962	4978965	4999965	5098365	5178960	4998965	4997854	5098854	5110454	5001545	4997898	5099797	5110452
18	9616017	10354736	9995623	10122441	10318702	9955602	7414277	10129773	10300306	9966601	7429778	10132382	10305969	9977760	7427381	10123203	10311452	9978637	7427457	10134579
19	5468974	5998874	6059673	6037584	6078654	6082854	6090025	6040452	6095745	6090845	6089254	6041452	6100125	6095841	6090145	6041578	6103025	6091542	6090033	6041525
20	10704512	11578965	11529564	11535326	11690631	11563728	11784855	11540854	11716854	11567654	11790021	11544475	11721546	11570354	11790054	11545302	11726988	11572525	11795846	11527799
21	30579	3341563	3261953	3348558	3362356	3268565	3145326	3351125	3372965	3273562	3146025	3348256	3373652	3274125	3146852	3349521	3378011	3269984	3147589	3349587
22	9511521	10481545	10568400	10528652	10573785	10585562	10560745	10528652	10585005	10591825	10563541	10530325	10588452	10588452	10560214	10530452	10586154	10589265	10560000	10537045
23	4163325	4512454	4521546	4512541	4533214	4539505	4500001	4519563	4543326	4544854	4494541	4512415	4538365	4545581	4486855	4512536	4540273	4538254	4486594	5413125
24	8348156	9146003	9107854	8600854	9200214	9138546	9367854	8615241	9220632	9145874	9378546	8611523	9226262	9148985	9379845	8611785	9227854	9151062	9385214	8618054
25	8302541	9065021	9095263	9002787	9128654	9117325	9203965	9009785	9146254	9125478	9208254	9016521	9016521	9126654	9208254	9013025	9156235	9128365	9204025	9015412
26	4454896	4947111	5005321	4958712	4986014	5013425	4848652	4958852	4988443	5015412	4954969	4949062	4990095	5015965	4954955	4958741	4991517	5017452	4955214	4953652
27	2049107	2305789	2335589	2402456	2321758	2339451	2313254	2388974	2331546	2345698	2305124	2392582	2334215	2344864	2305689	2390152	2335621	2345698	2306954	2403214
28	3241658	3442651	3449365	3426325	3456932	3464356	3432565	3421958	3475896	3468475	3436521	3421935	3481722	3471978	3433220	3425621	3483465	3475231	3435421	3422451
29	20867	23210	23107	22527	23521	23177	22526	23522	23569	23187	22528	23525	23544	23184	22530	23195	23546	23191	22533	23493
30	7150819	7774335	7893315	7836973	7890438	7952548	7888201	7854652	7830190	7827149	7814459	7784454	7842847	7779879	7769922	7795933	7856926	7862343	7826793	7795218
Mean	5082759	5658949	5664377	5595932	5710880	5680083	5554952	5597601	5717349	5683208	5559058	5601691	5718115	5682599	5557861	5599595	5725705	5686537	5561944	5628692

C: Configuration



Table 4. Counts with 10% threshold in all configurations.

Patient No	C1	C2	C3	C4	C5	C6	C7	C8	C9	C10	C11	C12	C13	C14	C15	C16	C17	C18	C19	C20
1	5709444	6213757	6245399	6202018	6258549	6262030	6195192	6183866	6245058	6319060	6203690	6221820	6257946	6278391	6205659	6221199	6270220	6266000	6259788	6187308
2	5933652	6683319	6735070	6940234	6809696	6771455	6707650	6942021	6829010	6779550	6708804	6940794	6830380	6783747	6712714	6943597	6832780	6784342	6712336	6942793
3	2623428	2882474	2865983	2776991	2908121	2875822	2842757	2778683	2912408	2880247	2843441	2780865	2916348	2881733	2842684	2780472	2917272	2881915	2842951	2780251
4	4118512	4477931	4441838	4580624	4508699	4448080	4450214	4585026	4514132	4450482	4450211	4583933	4514016	4449236	4449865	4585346	4514156	4451159	4449669	4584852
5	647087	708895	749869	720056	718065	722125	727919	755556	719148	722754	727957	757643	719166	722854	728432	743024	719479	722546	728137	734318
6	3815546	4134746	4154899	4076060	4158883	4162025	4129047	4079225	4164056	4164813	4130980	4081123	4164849	4164367	4130415	4080040	4166278	4164212	4130965	4081123
7	4426761	4383675	4451215	3230242	4486877	4495272	5885056	3220899	4515732	4511654	5900376	3221426	4526896	4518505	5901526	3220571	4530548	4522090	5903815	3220147
8	1862074	2021630	2054923	1978425	2039369	2061243	2045323	1983252	2043242	2063782	2045720	1980246	2046012	2064265	2045917	1979123	2046852	2064565	2046608	1979025
9	4454448	4828652	4869154	4706963	4872536	4875677	4844999	4714409	4878319	4882331	4843052	4709585	4877915	4882654	4842915	4709789	4878546	4881344	4844228	4709852
10	8174582	9417541	9539452	9523654	9695241	9623541	9785214	9524569	9736214	9635547	9790854	9535625	9747852	9645879	9791325	9547852	9753652	9658541	9788745	9549236
11	5582897	6093425	6161556	5996461	6150416	6192635	6114798	6006785	6174325	6199854	6117854	6008125	6180254	6198745	6123654	6007145	6182456	6200652	6123562	6007545
12	5586398	6264999	6330842	6173155	6321359	6349521	6186025	6182563	6335680	6356048	6198547	6188063	6345896	6359052	6198874	6188095	6345214	6362541	6198797	6183652
13	9616032	10354736	9995623	10124578	10317854	9955602	7414215	10129654	10300306	9966325	7429778	10139547	10302547	9977458	7425412	10132547	10311145	9987632	7425645	10132546
14	670765	731125	737261	750754	734535	740025	747458	751421	736852	741021	742565	750325	737785	741956	742789	750896	733632	741445	742635	750752
15	6988130	7678099	7732654	7666965	7759856	7765645	7809152	7608090	7764125	7767075	7809654	7678109	7785748	7776625	7822415	7681034	7795748	7792013	7823698	7682785
16	4622356	4990125	5043215	4975825	5036251	5063215	5094754	4985632	5042154	5069125	5096325	4985632	5047545	5071021	5096452	4985625	5050565	5073652	5093256	4988965
17	4587676	4931093	4975785	5119232	4985214	4993939	5096541	5112962	4978965	4999965	5098365	5178960	4998965	4997854	5098854	5110454	5001545	4997898	5099797	5110452
18	9616017	10354736	9995623	10122441	10318702	9955602	7414277	10129773	10300306	9966601	7429778	10132382	10305969	9977760	7427381	10123203	10311452	9978637	7427457	10134579
19	5468974	5998874	6059673	6037584	6078654	6082854	6090025	6040452	6095745	6090845	6089254	6041452	6100125	6095841	6090145	6041578	6103025	6091542	6090033	6041525
20	10704512	11578965	11529564	11535326	11690631	11563728	11784855	11540854	11716854	11567654	11790021	11544475	11721546	11570354	11790054	11545302	11726988	11572525	11795846	11527799
21	30579	3341563	3261953	3348558	3362356	3268565	3145326	3351125	3372965	3273562	3146025	3348256	3373652	3274125	3146852	3349521	3378011	3269984	3147589	3349587
22	9511521	10481545	10568400	10528652	10573785	10585562	10560745	10528652	10585005	10591825	10563541	10530325	10588452	10588452	10560214	10530452	10586154	10589265	10560000	10537045
23	4163325	4512454	4521546	4512541	4533214	4539505	4500001	4519563	4543326	4544854	4494541	4512415	4538365	4545581	4486855	4512536	4540273	4538254	4486594	5413125
24	8348156	9146003	9107854	8600854	9200214	9138546	9367854	8615241	9220632	9145874	9378546	8611523	9226262	9148985	9379845	8611785	9227854	9151062	9385214	8618054
25	8302541	9065021	9095263	9002787	9128654	9117325	9203965	9009785	9146254	9125478	9208254	9016521	9016521	9126654	9208254	9013025	9156235	9128365	9204025	9015412
26	4454896	4947111	5005321	4958712	4986014	5013425	4848652	4958852	4988443	5015412	4954969	4949062	4990095	5015965	4954955	4958741	4991517	5017452	4955214	4953652
27	2049107	2305789	2335589	2402456	2321758	2339451	2313254	2388974	2331546	2345698	2305124	2392582	2334215	2344864	2305689	2390152	2335621	2345698	2306954	2403214
28	3241658	3442651	3449365	3426325	3456932	3464356	3432565	3421958	3475896	3468475	3436521	3421935	3481722	3471978	3433220	3425621	3483465	3475231	3435421	3422451
29	20867	23210	23107	22527	23521	23177	22526	23522	23569	23187	22528	23525	23544	23184	22530	23195	23546	23191	22533	23493
30	7150819	7774335	7893315	7836973	7890438	7952548	7888201	7854652	7830190	7827149	7814459	7784454	7842847	7779879	7769922	7795933	7856926	7862343	7826793	7795218
Mean	5082759	5658949	5664377	5595932	5710880	5680083	5554952	5597601	5717349	5683208	5559058	5601691	5718115	5682599	5557861	5599595	5725705	5686537	5561944	5628692

C: Configuration

An Alternative Approach to Find the Position Vector of a General Helix

Gizem Güzelkardeşler¹ , Burak Şahiner^{2*} 

¹ Department of Mathematics, Karadeniz Technical University, Trabzon, Türkiye

² Department of Mathematics, Manisa Celal Bayar University, Manisa, Türkiye

* burak.sahiner@cbu.edu.tr

* Orcid No: 0000-0003-1471-1754

Received: 6 May 2024

Accepted: 14 June 2024

DOI: 10.18466/cbayarfbe.1479066

Abstract

In this paper, we introduce an alternative approach centered around an alternative moving frame for finding the position vector of a general helix given its curvature and torsion. Our methodology begins by formulating a vector differential equation, leveraging the unit principal normal vector of a general helix with the assistance of the alternative moving frame. Then, by solving this differential equation, we obtain the position vector of the general helix. This innovative technique is then applied to ascertain the position vector of a circular helix. To illustrate the effectiveness of our method, we showcase parametric representations of various general helices, each defined by unique curvature and torsion functions.

Keywords: Alternative moving frame, curvatures, general helix, position vector

1. Introduction

The fundamental theorem for curves states that a space curve can be uniquely determined up to rigid motions by its curvature and torsion [1,2]. The problem of determining the position vector of this curve is known as *solving natural or intrinsic equations* and is usually achieved by solving a certain complex Riccati equation [3]. However, the solution usually cannot be obtained explicitly. Explicit solutions have only been found for some special curves. First known example is an explicit integral formula by Euler for a planar curve, which is one of these special curves [4]. Recently, Ali constructed a vector differential equation according to the Frenet vectors by the aid of Frenet formulae to find the position vector of a space curve. Since this vector differential equation has variable coefficients, he did not find a general solution for an arbitrary curve. For the special cases of general helices and slant helices, he solved the vector differential equations and obtained the parametric representations of these curves in Euclidean 3-space [5,6]. After that, this problem has been investigated for different types of curves such as general helices, circular helices, slant helices, k -slant helices, relatively normal-slant helices, and isophote curves. These studies that constitute a vast literature on this subject include the handling of the curves in Euclidean, Minkowski, and Galilean spaces with the help of different moving frames

such as Frenet frame, Darboux frame, type-2 Bishop frame, and alternative moving frame [7-16].

There are two important reasons why the problem of finding the position vector of a curve still attracts researchers. Firstly, in Galilean space, this problem has been resolved by Ali in [7], however in Euclidean and Minkowski spaces, it remains unresolved for any curve. Secondly, since the trajectory followed by a particle moving in space can be thought of as a curve, examining the position vector of the curve is an important goal for determining the behavior of the particle.

This paper presents an approach utilizing an alternative moving frame to ascertain the position vector of a general helix given its curvature and torsion. Initially, we delve into the fundamentals of Frenet and alternative moving frames for space curves. Leveraging the derivative formulae of alternative moving frame, we formulate a vector differential equation based on the principal normal vector of the general helix. Solving this equation yields the position vector expressed in terms of the first alternative curvature. Subsequently, we extend this method to find the position vector of a circular helix. Finally, through practical application, we derive parametric representations of various examples of general helices, considering some certain functions for curvature and torsion.

With the method presented in this paper, the problem of determining the position vector of a curve, one of the important problems in the theory of curves, has been solved for both general helices and circular helices. The method presented in this paper is simpler and more practical than the method which is based on the use of Frenet frame in the literature. Moreover, the helix examples obtained by using the method in this paper add diversity to the helix examples in the literature.

2. The Frenet and Alternative Moving Frame

In this section, we briefly introduce the Frenet and alternative moving frames of a space curve in Euclidean 3-space denoted by E^3 and give some basic concepts of these frames.

Let $\alpha = \alpha(s)$ be a curve in E^3 . $\alpha(s)$ is said to be a unit speed curve if $\|\alpha'(s)\| = 1$, where s is the arc-length parameter of α . The Frenet frame of the curve α consists of three mutually orthonormal vectors $\mathbf{T}(s), \mathbf{N}(s), \mathbf{B}(s)$ defined by

$$\mathbf{T}(s) = \alpha'(s), \mathbf{N}(s) = \frac{1}{\|\mathbf{T}'(s)\|} \mathbf{T}'(s), \mathbf{B}(s) = \mathbf{T}(s) \times \mathbf{N}(s).$$

The vector fields $\mathbf{T}, \mathbf{N}, \mathbf{B}$ are called unit tangent vector field, unit principal normal vector field and unit binormal vector field, respectively [3]. The derivatives of the Frenet vectors are known as Frenet formulae and can be given as

$$\mathbf{T}'(s) = \kappa(s)\mathbf{N}(s),$$

$$\mathbf{N}'(s) = -\kappa(s)\mathbf{T}(s) + \tau(s)\mathbf{B}(s),$$

$$\mathbf{B}'(s) = -\tau(s)\mathbf{N}(s),$$

where $\kappa(s)$ and $\tau(s)$ are called the curvature and the torsion of the curve α , respectively. They can be found as $\kappa(s) = \|\mathbf{T}'(s)\|$ and $\tau(s) = -\langle \mathbf{B}'(s), \mathbf{N}(s) \rangle$ [3].

With the help of curvature and torsion of a curve, some geometric properties of the curve can be revealed. The curve is a straight line, for instance, if $\kappa = 0$, and the curve is a planar curve if $\tau = 0$ [17,18]. Moreover, thanks to curvature and torsion functions, it can be determined whether a curve is one of the special curves such as general helix, slant helix or spherical curve. For example, if the function τ/κ is a constant, then the curve is a general helix which is defined by the property that tangent vectors along the curve make a constant angle with a fixed vector [3]. The curve is referred to as a circular helix or a W-curve if the curvature and torsion are both non-zero constants [17,19].

The Frenet frame is an important tool for studying differential geometric properties of curves. However, there are other frames besides the Frenet frame that can

be used to examine differential geometric properties of a curve. Recently, there has been established a novel frame known as alternative moving frame and started to be used in many areas. Three vectors that are orthonormal to one another make up the alternative moving frame. These vectors are the principal normal vector $\mathbf{N}(s)$ that also exists in Frenet frame, the vector $\mathbf{C}(s)$ defined by $\mathbf{C}(s) = \mathbf{N}'(s)/\|\mathbf{N}'(s)\|$, and the vector $\mathbf{W}(s)$ which is in the direction of the instantaneous rotation vector of the Frenet frame and can be written as $\mathbf{W}(s) = \mathbf{N}(s) \times \mathbf{C}(s)$ [20,21]. The derivative formulae of the alternative moving frame $\{\mathbf{N}(s), \mathbf{C}(s), \mathbf{W}(s)\}$ can be given in matrix form as

$$\begin{bmatrix} \mathbf{N}'(s) \\ \mathbf{C}'(s) \\ \mathbf{W}'(s) \end{bmatrix} = \begin{bmatrix} 0 & f(s) & 0 \\ -f(s) & 0 & g(s) \\ 0 & -g(s) & 0 \end{bmatrix} \begin{bmatrix} \mathbf{N}(s) \\ \mathbf{C}(s) \\ \mathbf{W}(s) \end{bmatrix} \quad (1)$$

where f and g are referred to as first and second alternative curvatures, respectively [21]. By applying relations between Frenet and alternative moving frames, it is possible to derive the alternative curvatures as follows [21]:

$$f = \sqrt{\kappa^2 + \tau^2}, \quad (2)$$

and

$$g = \frac{\kappa^2}{\kappa^2 + \tau^2} \left(\frac{\tau}{\kappa} \right)'. \quad (3)$$

On the other hand, the alternative curvatures may be used to express the curvatures $\kappa(s)$ and $\tau(s)$ as follows [22]:

$$\kappa(s) = f(s) \cos \left(\int g(s) ds \right), \quad (4)$$

and

$$\tau(s) = f(s) \sin \left(\int g(s) ds \right). \quad (5)$$

Remark 2.1. In many studies examining curves with the help of alternative moving frame, it has been observed that some mathematical expressions cannot be produced only in terms of alternative moving frame apparatus and that both Frenet frame apparatus and alternative moving frame apparatus are combined improperly. This problem can be overcome with the help of the relations between the curvatures given by Eq. (4) and Eq. (5).

The alternative curvatures have a significant impact on the characterization of curves. This notion is supported by the following theorems.

Theorem 2.1. ([22]) Let α be a curve in E^3 , provided $f \neq 0$. The curve α is a general helix if and only if $g = 0$.

Theorem 2.2. Let α be a curve in E^3 , provided $f \neq 0$. The curve α is a circular helix if and only if $g = 0$ and f is a constant.

Proof. Let α be a circular helix. The curvature and torsion of this curve are both non-zero constants. From Eqs. (2) and (3), we have $g = 0$ and f is a constant.

Conversely, let $g = 0$ and f be a constant. From Eqs. (4) and (5), it can be seen that κ and τ are both constant. So, the curve α is a circular helix which completes the proof.

3. Finding the Position Vector of a General Helix

This section commences with the formulation of a vector differential equation, employing the principal normal vector of a general helix through the utilization of alternative moving frame. Subsequently, solving this equation yields the determination of the position vector of the general helix uniquely up to translation and rotation in E^3 . In this section, we initially use the derivative formulae of alternative moving frame to help us develop a vector differential equation in terms of the principal normal vector of a general helix. Since the principal normal vector is in Euclidean 3-space, this vector differential equation leads to a system of differential equation consisting of three differential equations. The position vector of the general helix is then obtained uniquely up to translation and rotation in E^3 by solving this system. Furthermore, we apply this technique to solve the problem of determining the position vector of a circular helix.

Let $\alpha = \alpha(s)$ be a unit speed curve in E^3 . Since the unit tangent vector of the curve α is defined by

$$\mathbf{T}(s) = \alpha'(s),$$

the curve α can be written as

$$\alpha(s) = \int \mathbf{T}(s) ds$$

or can be rewritten by using the Frenet formula as

$$\alpha(s) = \int \left(\int \kappa(s) \mathbf{N}(s) ds \right) ds. \quad (6)$$

Substituting Eq. (4) into Eq. (6), we have

$$\alpha(s) = \int \left(\int f(s) \cos \left(\int g(s) ds \right) \mathbf{N}(s) ds \right) ds. \quad (7)$$

If curvature and torsion functions of a curve are given, alternative curvatures f and g can be found with the help of Eqs. (2) and (3). The only thing required to determine the position vector of the curve is to find the vector $\mathbf{N}(s)$ in Eq. (7).

The subsequent theorem establishes a vector differential equation concerning the vector $\mathbf{N}(s)$ for a general helix.

Theorem 3.1. Let $\alpha = \alpha(s)$ be a unit speed curve in E^3 . If α is a general helix, then the principal normal vector $\mathbf{N}(s)$ of the curve α satisfies the following vector differential equation

$$\mathbf{N}''(s) = f'(s) \frac{1}{f(s)} \mathbf{N}'(s) - f^2(s) \mathbf{N}(s), \quad (8)$$

where f is the first alternative curvature of α .

Proof. Let $\alpha = \alpha(s)$ be a unit speed general helix in E^3 . Differentiating the first equation of Eq. (1) and using the second equation of Eq. (1), we have

$$\mathbf{N}''(s) = f'(s) \mathbf{C}(s) + f(s) (-f(s) \mathbf{N}(s) + g(s) \mathbf{W}(s)). \quad (9)$$

We get $g = 0$ from Theorem 2.1 because the curve α is a general helix. Thus the Eq. (9) becomes

$$\mathbf{N}''(s) = f'(s) \mathbf{C}(s) - f^2(s) \mathbf{N}(s). \quad (10)$$

Substituting the first equation in Eq. (1) into Eq. (10), Eq. (8) is obtained which completes the proof.

If the vector $\mathbf{N}(s)$ obtained by solving Eq. (8) is substituted into Eq. (7), the position vector of the general helix can be determined. The following theorem provides the position vector of a general helix in terms of first alternative curvature.

Theorem 3.2. Let $\alpha = \alpha(s)$ be a unit speed curve in E^3 . If α is a general helix, then the position vector $\alpha(s) = (\alpha_1(s), \alpha_2(s), \alpha_3(s))$ can be given in terms of first alternative curvature as follows:

$$\begin{cases} \alpha_1(s) = \int \left(\int f(s) \cos(c_1) \cos \left(\int f(s) ds \right) ds \right) ds, \\ \alpha_2(s) = \int \left(\int f(s) \cos(c_1) \sin \left(\int f(s) ds \right) ds \right) ds, \\ \alpha_3(s) = \int c_2 ds, \end{cases} \quad (11)$$

where c_1 and c_2 are real constants.

Proof. Given that α is a general helix, it follows that

$$\langle \mathbf{T}(s), \mathbf{U} \rangle = \cos \theta, \quad (12)$$

where \mathbf{U} is a constant vector parallel to the axis of the curve α and θ is a constant angle between \mathbf{T} and \mathbf{U} . Differentiating Eq. (12) and using the first equation of Frenet formulae, we have

$$\langle \mathbf{N}(s), \mathbf{U} \rangle = 0.$$

The unit principal normal vector can be written with the standard basis of E^3 as $N(s) = N_1e_1 + N_2e_2 + N_3e_3$. We can select e_3 as the axis of the curve α without losing generality. So, we have

$$\langle N(s), e_3 \rangle = N_3 = 0.$$

Since $N(s)$ is a unit vector, we have the following relation between the components of $N(s)$:

$$N_1^2 + N_2^2 = 1. \quad (13)$$

From Eq. (13), the components N_1 and N_2 can be written as

$$N_1(s) = \cos[t(s)] \text{ and } N_2(s) = \sin[t(s)],$$

where t is a function of the arc-length parameter s . Thus, the vector $N(s)$ can be written according to the function of $t(s)$ as

$$N(s) = (\cos[t(s)], \sin[t(s)], 0).$$

Each component of the vector $N(s)$ must meet Eq. (8). It is easy to see that $N_3 = 0$ satisfies Eq. (8). When the components N_1 and N_2 are substituted into Eq. (8), we obtain the following differential equations of $t(s)$:

$$(-(t')^2 + f^2)\cos t + \left(-t'' + \frac{f'}{f}t'\right)\sin t = 0, \quad (14)$$

$$\left(t'' - \frac{f'}{f}t'\right)\cos t + (-(t')^2 + f^2)\sin t = 0. \quad (15)$$

From Eqs. (14) and (15), we have the following differential equations

$$-(t')^2 + f^2 = 0, \quad (16)$$

$$-t'' + \frac{f'}{f}t' = 0. \quad (17)$$

From Eq. (16), we get

$$t' = f,$$

or

$$t' = -f.$$

Since the above equations satisfy Eq. (17), we have

$$t = \int f(s)ds,$$

or

$$t = -\int f(s)ds.$$

Consequently, the principal normal vector $N(s)$ of the general helix α can be found as

$$N(s) = \left(\cos\left(\int f(s)ds\right), \sin\left(\int f(s)ds\right), 0 \right) \quad (18)$$

or

$$N(s) = \left(\cos\left(\int f(s)ds\right), -\sin\left(\int f(s)ds\right), 0 \right). \quad (19)$$

Then by substituting Eq. (18) or Eq. (19) into Eq. (7) and by using Theorem 2.1, we have Eq. (11) which completes the proof.

Substituting Eq. (2) and Eq. (4) into Eq. (11), the position vector of a general helix can be given in terms of curvatures of Frenet frame as in the following corollary.

Corollary 3.1. Let $\alpha = \alpha(s)$ be a unit speed curve in E^3 . If α is a general helix, then the position vector $\alpha(s) = (\alpha_1(s), \alpha_2(s), \alpha_3(s))$ is expressed as

$$\begin{cases} \alpha_1(s) = \int \left(\int \kappa(s) \cos\left(\int \sqrt{\kappa^2(s) + \tau^2(s)} ds\right) ds \right) ds, \\ \alpha_2(s) = \int \left(\int \kappa(s) \sin\left(\int \sqrt{\kappa^2(s) + \tau^2(s)} ds\right) ds \right) ds, \\ \alpha_3(s) = \int c_2 ds, \end{cases} \quad (20)$$

where c_2 is a constant.

From Theorem 2.2 and Theorem 3.2, the position vector of a circular helix can be given in terms of first alternative curvature as in the following corollary.

Corollary 3.2. Let $\alpha = \alpha(s)$ be a unit speed curve in E^3 . If α is a circular helix, then the position vector $\alpha(s) = (\alpha_1(s), \alpha_2(s), \alpha_3(s))$ can be computed as

$$\begin{cases} \alpha_1(s) = -\frac{1}{f} \cos(c_1) \cos(fs), \\ \alpha_2(s) = -\frac{1}{f} \cos(c_1) \sin(fs), \\ \alpha_3(s) = f \cos(c_1) c_2 s, \end{cases}$$

where c_1 and c_2 are real constants.

Since the curvature κ and torsion τ of a circular helix are both non-zero constants, Eq. (20) which gives the position vector of a general helix in terms of curvatures of Frenet frame can be adapted for the position vector of a circular helix as in the following corollary.

Corollary 3.3. Let $\alpha = \alpha(s)$ be a unit speed curve in E^3 . If α is a circular helix, then the position vector $\alpha(s) = (\alpha_1(s), \alpha_2(s), \alpha_3(s))$ can be given as

$$\begin{cases} \alpha_1(s) = -\frac{\kappa}{\kappa^2 + \tau^2} \cos(\sqrt{\kappa^2 + \tau^2} s), \\ \alpha_2(s) = -\frac{\kappa}{\kappa^2 + \tau^2} \sin(\sqrt{\kappa^2 + \tau^2} s), \\ \alpha_3(s) = \kappa c_2 s, \end{cases}$$

where c_2 is a real constant.

4. Examples

In this section, we obtain position vectors for some examples of general helices given some special functions for curvature and torsion with the help of the alternative approach described in the previous section. In the process of finding the parametric representations, we choose the integral constants in Eq. (11) or Eq. (20) as some real numbers so that the general helices are curves with unit speed. The axes of all the general helices in the following examples are chosen as parallel to e_3 .

Example 4.1. Let curvature and torsion functions be given as $\kappa = 1/s$ and $\tau = 1/s$, respectively. From Eqs. (2) and (3), we have the alternative curvatures as $f = \sqrt{2}/s$ and $g = 0$. By using Eq. (11), the position vector of the general helix can be obtained in the parametric representation as

$$\alpha(s) = \left(\frac{1}{3\sqrt{2}} (s \sin(\sqrt{2} \ln s) - \sqrt{2} s \cos(\sqrt{2} \ln s)), \right. \\ \left. -\frac{1}{3\sqrt{2}} (s \cos(\sqrt{2} \ln s) + \sqrt{2} s \sin(\sqrt{2} \ln s)), \frac{1}{\sqrt{2}} s \right).$$

An illustration of the curve α is given in Figure 4.1.

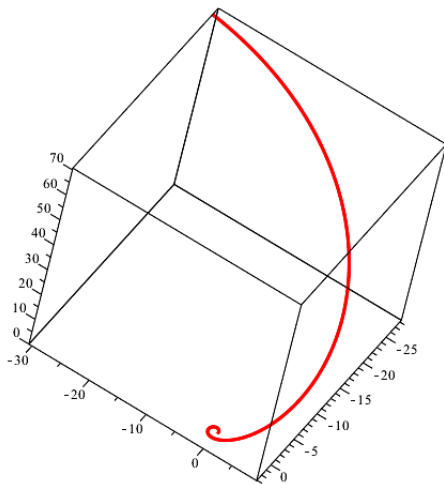


Figure 4.1. The general helix with $\kappa = 1/s$ and $\tau = 1/s$

Example 4.2. If we take $\kappa = \frac{1}{2\sqrt{2}s}$ and $\tau = \frac{1}{2\sqrt{2}s}$, then we get $f = \frac{1}{2\sqrt{5}}$ and $g = 0$. By using Eq. (11), the position vector $\alpha(s)$ of the general helix is expressed as

$$\alpha(s) = \left(\sqrt{2} (\sin(\sqrt{s}) - \sqrt{s} \cos(\sqrt{s})), \right. \\ \left. -\sqrt{2} (\sqrt{s} \sin(\sqrt{s}) + \cos(\sqrt{s})), \frac{1}{\sqrt{2}} s \right).$$

The shape of the curve α is given in Figure 4.2.

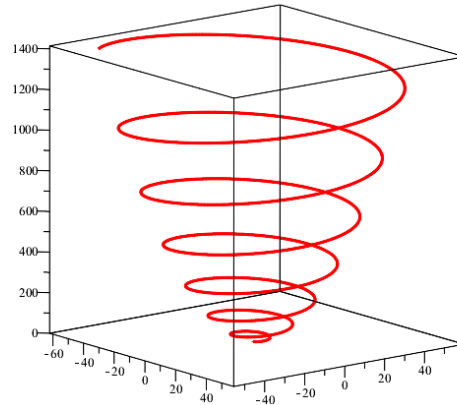


Figure 4.2. The general helix with $\kappa = \frac{1}{2\sqrt{2}s}$ and $\tau = \frac{1}{2\sqrt{2}s}$

Example 4.3. Let consider the general helix $\alpha(s)$ with curvature $\kappa = \frac{1}{\sqrt{2-2s^2}}$ and torsion $\tau = \frac{1}{\sqrt{2-2s^2}}$. Without finding the alternative curvatures, by using Eq. (20), the position vector of the general helix is obtained as follows:

$$\alpha(s) = \left(\frac{s^2}{2\sqrt{2}}, -\frac{s \sqrt{1-s^2} + \sin^{-1}(s)}{2\sqrt{2}}, \frac{1}{\sqrt{2}} s \right).$$

One can see the shape of the curve α in Figure 4.3.

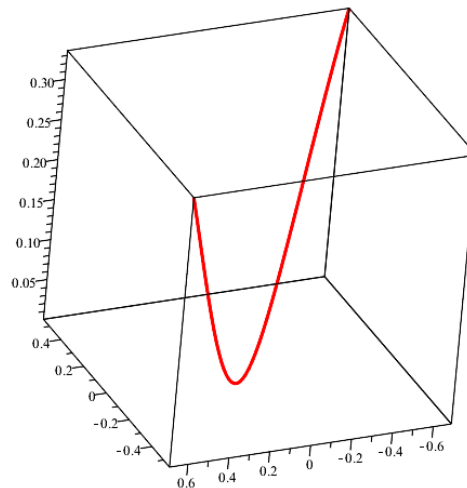


Figure 4.3. The general helix with $\kappa = \frac{1}{\sqrt{2-2s^2}}$ and $\tau = \frac{1}{\sqrt{2-2s^2}}$

Example 4.4. The position vector $\alpha(s)$ of the general helix with $\kappa = \frac{1}{\sqrt{2}(s^2+1)}$ and $\tau = \frac{1}{\sqrt{2}(s^2+1)}$ can be found in parametric form as

$$\alpha(s) = \left(\frac{\sqrt{1+s^2}}{\sqrt{2}}, -\frac{\sinh^{-1}(s)}{\sqrt{2}}, \frac{1}{\sqrt{2}}s \right).$$

The shape of the curve α is given in Figure 4.4.

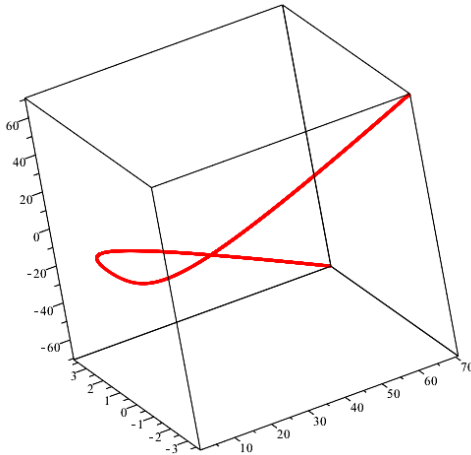


Figure 4.4. The general helix with $\kappa = \frac{1}{\sqrt{2}(s^2+1)}$ and $\tau = \frac{1}{\sqrt{2}(s^2+1)}$

5. Conclusions

The problem of determining the position vector of an arbitrary curve given its curvature and torsion, known as solving natural or intrinsic equations, is still an open problem in Euclidean 3-space. In this study, we proposed a method based on alternative moving frame to solve this problem for general helices. Using the derivative formulae of alternating moving frame, we first built a vector differential equation correspond to a system of three differential equations in terms of the principal normal vector of a general helix. Then, by solving this system, we found the principal normal vector of the general helix, which allows us to find the position vector of the general helix. We gave the position vector of the general helix, which depends only on the first alternative curvature, in parametric form as in Eq. (11). By using the relation between the first alternative curvature and curvatures of Frenet frame as given in Eq. (2), we also gave the parametric representation of the general helix in terms of curvatures of Frenet frame as in Eq. (20). So, we have two ways to find the position vector of a general helix given its curvature and torsion. The first is to use Eq. (20) directly, and the second is to use Eq. (11) after finding the first alternative curvature with the help of Eq. (2). Moreover, we adapted these two ways to find the position vector of a circular helix.

The problem discussed in the present paper was solved by a method based on the use of the Frenet frame in [5]. In that paper, a vector differential equation was constructed in terms of unit tangent vector by the aid of Frenet formulae and solved to find the position vector of a general helix. It can be said that the method based on the alternative moving frame used in the present paper

for determining the position vector of a general helix is simpler and more practical compared to the method in [5]. While parameter change is required to obtain the vector differential equation for finding the position vector of a general helix in [5], it is another advantage of the present paper that this vector differential equation can be constructed according to the arc-length parameter of the curve without any parameter change.

Since helices are used in many different fields such as biology, chemistry, mechanical engineering, and computer-aided geometric design, we hope that this study will contribute scientifically to the relevant fields. Furthermore, we expect that the examples of general helices obtained in the previous section can add variety to the examples of general helices in the literature.

Author's Contributions

This paper is derived from the first author's master's thesis supervised by the second author. Both authors contributed to the writing of the manuscript.

Gizem Güzelkardeşler: conducted the literature review, performed mathematical operations, and found the results.

Burak Şahiner: guided and supervised the whole process and interpreted the results.

Ethics

There are no ethical issues after the publication of this manuscript.

References

- [1]. Eisenhart, LP. A Treatise on Differential Geometry of Curves and Surfaces; Dover, New York, 1960.
- [2]. Hartman, P., Wintner, A. 1950. On the fundamental equations of differential geometry. *American Journal of Mathematics*; 72(4): 757-774.
- [3]. Struik, DJ. Lectures on Classical Differential Geometry, 2nd edn.; Dover, New York, 1961.
- [4]. Euler, L. 1736. De constructione aequationum ope motus tractorii aliusque ad methodum tangentium inversam pertinentibus. *Commentarii Academie Scientiarum Petropolitane*; 8: 66-85.
- [5]. Ali, AT. 2011. Position vectors of general helices in Euclidean 3-space. *Bulletin of Mathematical Analysis and Applications*; 3(2): 198-205.
- [6]. Ali, AT. 2012. Position vectors of slant helices in Euclidean 3-space. *Journal of the Egyptian Mathematical Society*; 20(1): 1-6.
- [7]. Ali, AT. 2012. Position vectors of curves in the Galilean space G_3 . *Matematički Vesnik*; 64(3): 200-210.
- [8]. Ali, AT, Mahmoud, SR. 2014. Position vector of spacelike slant helices in Minkowski 3-space. *Honam Mathematical Journal*; 36(2): 233-251.



- [9]. Ali, AT, Turgut, M. 2010. Position vector of a time-like slant helix in Minkowski 3-space. *Journal of Mathematical Analysis and Applications*; 365(2): 559-569.
- [10]. Bozok, HG, Sepet, SA, Ergüt, M. 2018. Position vectors of general helices according to type-2 Bishop frame in E^3 . *Mathematical Sciences and Applications E-Notes*; 6(1): 64-69.
- [11]. El Haimi, A, Chahdi, AO. 2021. Parametric equations of special curves lying on a regular surface in Euclidean 3-space. *Nonlinear Functional Analysis and Applications*; 26(2): 225-236.
- [12]. El Haimi, A, Izid, M, Chahdi, AO. 2021. Position vectors of curves generalizing general helices and slant helices in Euclidean 3-space. *Tamkang Journal of Mathematics*; 52(4): 467-478.
- [13]. Öztekin, H, Tatlıpınar, S. 2014. Determination of the position vectors of curves from intrinsic equations in G_3 . *Walailak Journal of Science and Technology*; 11(12): 1011-1018.
- [14]. Şahin, T, Dirişen, BC. 2019. Position vectors of curves with respect to Darboux frame in the Galilean space G^3 . *Communications Faculty of Sciences University of Ankara Series A1: Mathematics and Statistics*; 68(2): 2079-2093.
- [15]. Yılmaz, B, Has, A. 2019. New approach to slant helix. *International Electronic Journal of Geometry*; 12(1): 111-115.
- [16]. Güzelkardeşler, G, Şahiner, B. 2023. An alternative method for determination of the position vector of a slant helix. *Journal of New Theory*; 4: 97-105.
- [17]. O'Neill, B. *Elementary Differential Geometry*; Academic Press, New York, 1966.
- [18]. Do Carmo, MP. *Differential Geometry of Curves and Surfaces*; Dover Publications, Mineola, USA, 2016.
- [19]. Chen, BY, Dillen, F, Verstraelen, L. 1986. Finite type space curves. *Soochow Journal of Mathematics*; 12: 1-10.
- [20]. Scofield, PD. 1995. Curves of constant precession. *American Mathematical Monthly*; 102(6): 531-537.
- [21]. Uzunoğlu, B, Gök, İ, Yaylı, Y. 2016. A new approach on curves of constant precession. *Applied Mathematics and Computations*; 275: 317-323.
- [22]. Şahiner, B. 2019. Ruled surfaces according to alternative moving frame. *arXiv preprint arXiv:1910.06589*.

Influence of Sintering Time on Electrical Properties, Densification, and Microstructure of PMN-PT-PMS Piezoelectric Ceramics

Volkan Kalem^{1*} , Osman Düzen^{2,3} 

¹ Department of Metallurgical and Materials Engineering, Faculty of Engineering and Natural Sciences, Konya Technical University, Konya, Türkiye

² Department of Metallurgical and Materials Engineering, Institute of Sciences, Selçuk University, Konya, Türkiye

³ Vesuvius Istanbul Refractory, Kocaeli, Türkiye

*vkalem@ktun.edu.tr

*Orcid No: 0000-0001-9128-5686

Received: 15 March 2024

Accepted: 24 June 2024

DOI: 10.18466/cbayarfbe.1452081

Abstract

The effect of sintering soaking time on the dielectric, piezoelectric, and structural properties of PMN-PT-PMS [Pb(Mg_{1/3}Nb_{2/3})O₃-PbTiO₃-Pb(Mn_{1/3}Sb_{2/3})O₃] ceramics was systematically investigated. High density samples were prepared using solid-state sintering technique with different soaking times (60-150 min). Rhombohedral perovskite structure was the dominant phase for all soaking times, confirmed by XRD analysis. However, the pure perovskite structure could not be preserved at sintering times over 120 min. SEM micrographs indicated that homogeneous microstructures were obtained for all soaking times and the grain and pore sizes increased slightly with longer sintering time. Dielectric and piezoelectric test results showed that the optimum value of dielectric constant, electromechanical coupling factor, and piezoelectric strain coefficient was obtained for PMN-PT-PMS when sintered for 90 min. Ceramic samples with high density and perovskite structure prepared by proper sintering condition yielded high dielectric and piezoelectric response.

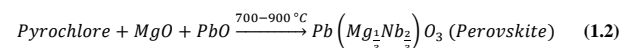
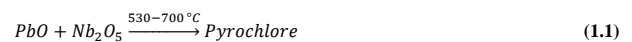
Keywords: Ceramic, Dielectric, Piezoelectric, PMN-PT, Sintering

1. Introduction

Electronic ceramics have been used for a wide range of applications since the 20th century with the discovery of high dielectric constant materials. Ferroelectrics, a subgroup of electronic ceramics, are preferred in many important applications such as underwater imaging, communication, and medical imaging devices, owing to their different functional properties [1].

The relaxor Pb(Mg_{1/3}Nb_{2/3})O₃ (PMN) is a ferroelectric material with good voltage stability, low sintering temperatures (<1000 °C), and high dielectric characteristic at Curie temperature (T_c). However, the Curie temperature of this material is around -15 °C, which limits its use [2]. With the addition of PbTiO₃ (PT), which has normal ferroelectric properties and a high Curie temperature (~ 490 °C), the phase transformation temperature of PMN reaches higher values, thus increasing its usage areas.

(1-x)PMN-(x)PT solid solution, with perovskite crystal structure, forms a morphotropic phase boundary (MPB) between the tetragonal and rhombohedral phases at approximately x=0.325 at room temperature. Compositions in the vicinity of MPB exhibit optimum dielectric, ferroelectric, and piezoelectric properties [3]. Unlike other ferroelectric ceramics, compositions containing lead and niobium (such as PMN-PT) cannot be easily obtained in the perovskite structure by conventional calcining of the oxide raw material mixture. The reactions that occur during the calcination process used for PMN production are as follows [4, 5]:



Since reaction-2 is not exactly balanced, the unwanted pyrochlore phase cannot completely transform into the perovskite phase. While the Pb/Nb ratio is 1.5 in the perovskite phase, this ratio is generally less than 1.5 in the pyrochlore phase [6-9]. Hence, the product obtained

as a result of the abovementioned reactions is a mixture of perovskite and pyrochlore phases. The pyrochlore phase, which has a very low Curie temperature ($-70\text{ }^{\circ}\text{C}$) and low dielectric constant, negatively affects the dielectric and electromechanical properties of ferroelectric ceramics containing pyrochlore [5]. Although $(1-x)\text{PMN}-(x)\text{PT}$ ($x=0.30-0.40$) compositions close to the morphotropic phase boundary have high piezoelectric and dielectric parameters, their mechanical quality factors (Q_m) are low and dielectric and mechanical losses are quite high. One of the effective methods for improving the electrical properties, preventing the formation of undesired pyrochlore phase, and obtaining a pure perovskite structure is appropriate doping of the basic PMN-PT composition. An example of these doping agents is $\text{Pb}(\text{Mn}_{1/3}\text{Sb}_{2/3})\text{O}_3$ (PMS). In previous studies, it was determined that Mn and Sb doping increased the properties of PMN-PT piezoelectric ceramics such as dielectric constant (K^T) and Q_m [10]. In another study conducted by Takahashi et al. [11], the electrical properties and the densities of PMN-PT-PMS systems were examined. They demonstrated that the electrical properties of PMN-PT ceramics can be modified in a wide range with changing amount of PMS additive. Increasing amount of PMS caused the resulting ceramic to transform from a soft material to a hard one (low piezoelectric constant (d_{31}) and high mechanical quality factor (Q_m)). In a previous study conducted by Aydın and Kalem [12], the effect of PMS addition in 67PMN-33PT composition was examined. 6 mol% PMS addition yielded the optimum dielectric and piezoelectric properties ($K^T=4652$, $\tan\delta=2.6\%$, $d_{33}=255\text{ pC/N}$, $k_p=0.422$, $Q_m=210$, and $T_C=146\text{ }^{\circ}\text{C}$). Sintering parameters, along with the doping process, are also known to have a significant effect on the structural and electrical properties of both lead-based and lead-free piezoelectric compositions. This effect is greater in compositions containing volatile elements such as potassium, sodium, lead, and bismuth [13-18]. In this study, to examine the effect of sintering time, 67PMN-33PT piezoelectric ceramics with 6 mol% PMS additives were sintered for different soaking times between 60-150 minutes. In order to obtain samples with high density and perovskite structure, excess MgO and a single calcination step were used. It was previously demonstrated that this method successfully prevented the formation of the pyrochlore phase [12]. Ceramic samples obtained were characterized in terms of structural and electrical properties to reveal the relationship between sintering time and microstructure, physical and electrical properties.

2. Materials and Methods

2.1. Preparation of Ceramic Powders

Within the scope of this study, polycrystalline PMN-PT-PMS piezoelectric ceramic samples were produced using the solid-state synthesis method. Excess MgO was

added to the composition to prevent the formation of undesired pyrochlore phases in the structure. For each $0.94[0.67\text{Pb}(\text{Mg}_{1/3}\text{Nb}_{2/3})\text{O}_3-0.33\text{PbTiO}_3]-0.06[\text{Pb}(\text{Mn}_{1/3}\text{Sb}_{2/3})\text{O}_3]$ composition prepared, an extra 5% MgO per mole was added. PbO (Alfa Aesar, 99.9%), MgO (Sigma-Aldrich, 99%), Nb_2O_5 (Alfa Aesar, 99.5%), TiO_2 (Sigma-Aldrich, 99%), MnO (Sigma-Aldrich, 99%) and Sb_2O_3 (Alfa Aesar, 99%) powders were used as raw materials.

Oxide powders weighed for the selected PMN-PT-PMS composition were milled in a ball mill for 10 h to reduce the powder size and provide a homogeneous mixture. Grinding process was carried out at a mixing speed of 200 rpm in a polyethylene container containing ZrO_2 balls with 5 mm diameter and 99% purity ethanol. The ground powders were left to dry at $90\text{ }^{\circ}\text{C}$ for 24 h, and the resulting homogeneous powder mixture was pressed into pellets in a uniaxial dry press at 90 MPa pressure. Samples were calcined in a muffle furnace at $850\text{ }^{\circ}\text{C}$ for 2 h. After the calcination, pellets were crushed to powder form in an agate mortar and ground in the ball mill for further 24 h. 5 wt% PVA ($[\text{CH}_2\text{CH}(\text{OH})]_n$, $M_n=6000$) was added as a binder to the ground powders. Green ceramic discs, each measuring 16 mm in diameter were prepared using the plasticized powders. Compaction of the disc samples were done by uniaxial pressing under a load of 100 MPa. Binder in the disc samples was burnout by firing them at $600\text{ }^{\circ}\text{C}$ for 1 h in ambient atmosphere without any gas flow. Samples were sintered in a muffle furnace by soaking them at $1175\text{ }^{\circ}\text{C}$ for different time (60, 90, 120, and 150 min). Sintering temperature of $1175\text{ }^{\circ}\text{C}$ was selected since it provided the best piezoelectric and dielectric performance for the PMN-PT-PMS composition in this study [13]. A closed crucible assembly was used which contained the base powder bedding to inhibit Pb evaporation during sintering.

2.2. Characterization

The densities of the sintered samples were determined using the Archimedes' principle. The liquid medium used for this purpose was Xylene ($\rho = 0.88\text{ g/cm}^3$). Bruker D8 Advance model X-ray diffractometer (XRD) was used to examine the phase formations of sintered samples. Measurements were carried out with a scanning speed of $2^{\circ}/\text{min}$, in the range of $2\theta=20-60^{\circ}$ and using $\text{Cu-K}\alpha$ radiation. Microstructural examination of the produced samples was carried out using FEI Nova Nano 430 FEG scanning electron microscope on thermally etched surfaces. The samples were given a thermal etch at $1000\text{ }^{\circ}\text{C}$ for 1 h in air atmosphere. During etching, samples were enclosed using alumina crucibles to compensate for Pb loss.

For electromechanical characterization, the parallel surfaces of the sintered samples were first sanded with 1000 grit SiC sandpaper, then the sample surfaces were

electroded with silver paste and fired at 700 °C for 1 h. Electroded samples were placed in 120 °C silicone oil and poled under a 2 kV/mm electric field for 15 min. Dielectric properties such as free dielectric constant (K^T) and loss tangent ($\tan \delta$) were determined by measuring capacitance and loss factors under 1 kHz frequency by impedance analysis method (Hioki IM-3570 LCR meter). Planar electromechanical coupling (k_p) and mechanical quality (Q_m) factors were calculated through resonance-antiresonance characteristics determined via impedance analyzer (HP 4194A impedance analyzer). Piezoelectric constant (d_{33}) measurement was carried out using a Berlincourt d33-piezometer.

3. Results and Discussion

Density results of PMN-PT-PMS samples produced using different sintering times are given in Table 1. Density calculation was made by taking the average of the density values of 3 samples for each sintering time. Theoretical density value, calculated via the XRD data of the PMN-PT-PMS composition, was 8.18 g/cm³. High density samples with more than 96% of the theoretical density (T.D.) were obtained at all sintering times. These high-density values are adequate for electrical measurements to be made. However, with the increase of sintering time, the density first increased, reached its highest value for 90 minutes of sintering time, and then decreased. Too long sintering times can result in PbO losses and growth of large grains which in turn lead to formation of porosity. Thus, the density decreases. The results revealed that sintering time significantly affected the densification of PMN-PT-PMS ceramics. Lowering of densification at longer soaking times can negatively alter the piezoelectric and dielectric performance.

Table 1. Density and average grain size values of PMN-PT-PMS samples sintered at 1175 °C.

Soaking time (min.)	ρ_{measured} (g/cm ³)	ρ_{relative} (%T.D.)	Average Grain Size (μm)
60	7.89	96.5	3.8
90	8.03	98.2	4.3
120	8.01	97.9	4.5
150	7.98	97.5	5.1

XRD patterns of PMN-PT-PMS ceramics sintered at different times are given in Figure 1. Experimental diffraction lines of a PMN-PT ceramic with MPB composition consist of three separate peaks between 44° and 46° (2 θ). Two of these peaks - one of which is approximately half the intensity of the other - belong to the tetragonal phase, and the central peak between these two peaks belongs to the rhombohedral phase. To clearly understand the effect of sintering time on the phase structure, XRD pattern with the range of 44–46° was magnified and given as an inset of Figure 1. Since

all the patterns in Figure 1 have single peak in the mentioned 2 θ range, it was concluded that the perovskite structure in all samples had rhombohedral symmetry. It was previously reported that the transformation to rhombohedral symmetry occurred in PMN-PT ceramics with the addition of PMS [12]. No secondary phase was observed in the XRD patterns of the samples sintered at 1175 °C up to 120 min soaking time. However, when the time is increased to 150 minutes, the pyrochlore phase emerges as a secondary phase. Formation of the pyrochlore may be due to the increase in the volatility of lead oxide during long sintering times and, as a result, the deterioration of the stoichiometry of the composition with perovskite structure. The emergence of the secondary phase upon longer sintering has also been reported for other lead-based piezoelectric ceramic compositions [19]. XRD analyzes revealed that long sintering times have a negative effect on the phase structure of PMN-PT-PMS ceramics and cause the formation of the undesired pyrochlore phase.

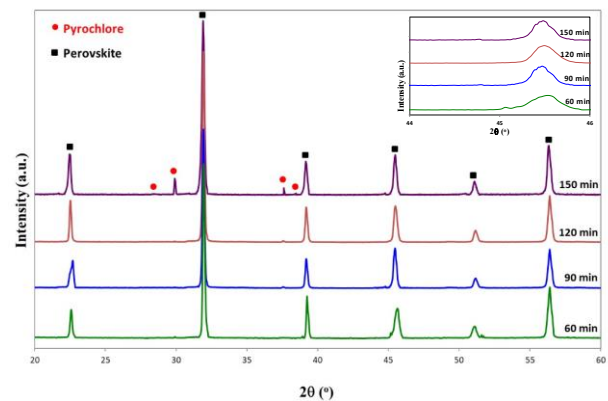


Figure 1. XRD patterns of the sintered samples with different soaking times.

The sintering process affects not only the density values and the crystal structure, but also the microstructure of the ceramics. SEM images of samples sintered at 1175 °C for different periods of time are given in Figure 2. A dense structure is observed in all samples. Increasing sintering time causes a slight increase in average grain size (Table 1). However, as shown in Figure 1, the increase of the amount and size of pores in long sintering times cause the density values to decrease in sintering conditions over 90 minutes. The grain size distribution, especially for the samples sintered for 90 and 120 minutes, is rather wide. Small grains fill the spaces between the larger ones, which resulted in high density values (Table 1).

Variation of density, crystal structure, and microstructure depending on the sintering time also significantly affected the electrical properties of the samples. Dielectric and piezoelectric properties of samples produced at different soaking times are given in Table 2. Values in Table 2 were the average values of

the electrical parameters of 3 samples for each sintering time. Dielectric constant (K^T), piezoelectric strain coefficient (d_{33}), and electromechanical coupling factor (k_p) values reached their highest values within 90 min of sintering time. The high density as well as homogeneous and pyrochlore-free microstructure obtained during this sintering period enabled high electrical properties to be obtained. Another reason for the high dielectric constant value is the presence of the rhombohedral structure alone. In PMN-PT based ceramics, PMN-rich (rhombohedral dominant) compositions exhibit higher dielectric constant values compared to PT-rich compositions (tetragonal dominant) [20]. Since 60 min-sintering resulted in a lower density value compared to longer times, the electrical properties obtained during this period were lower than others. The high density and pure perovskite structure obtained at sintering times of 90 and 120 min appeared as a positive effect on electrical properties. Although high density was also achieved in the 150 min sintering time, the existence of the pyrochlore phase during this sintering time negatively affected the mentioned electrical properties.

One of the most important factors affecting the dielectric and piezoelectric behavior of a piezoelectric ceramic is grain size. Increasing grain size is generally accompanied by an increase in the domain size and, as a result, the domain boundaries per unit volume of the sample decrease [21]. These boundaries restrict domain wall movement, and as the grain size decreases, domain wall movement becomes more inhibited. Mechanical quality factor (Q_m) and loss tangent ($\tan \delta$) values were not directly affected by the density change, unlike other parameters given in Table 2. In the change of these parameters, the effect of grain size is more dominant. The slight increase in grain size with increasing

sintering time facilitated the domain boundary movement, which in turn caused an increase in dielectric losses and a slight decrease in mechanical quality factor values. All experimental results in this study revealed that electrical parameters in piezoelectric ceramics and in general in all ceramic materials used in electronic applications can be improved by sintering conditions, in addition to effects such as doping and sintering additives. The electrical parameters obtained in this study are competitive or better than those of similar compositions reported in the literature, as shown in Table 3.

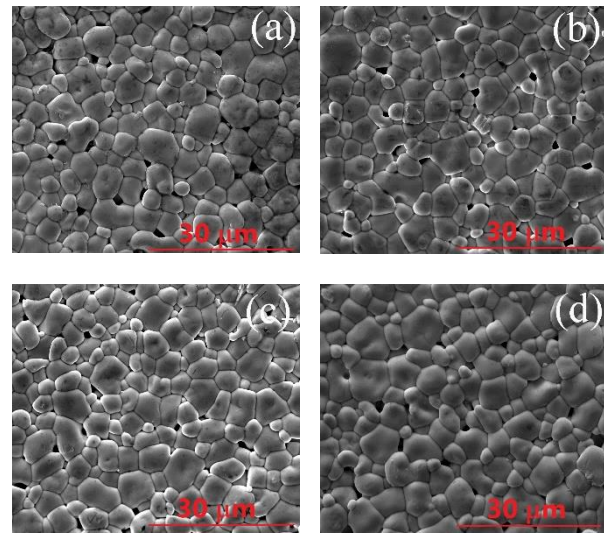


Figure 2. SEM micrographs of PMN-PT-PMS samples sintered for different soaking time: (a) 60, (b) 90, (c) 120, and (d) 150 min.

Table 2. Dielectric and piezoelectric properties of PMN-PT-PMS samples.

Soaking time (min.)	K^T	$\tan \delta$ (%)	d_{33} (pC/N)	Q_m	k_p
60	4422±19	2.4±0.05	257±9	230.1±1.1	0.409±0.004
90	4800±22	2.5±0.04	270±10	229.7±2.2	0.418±0.004
120	4745±18	2.5±0.05	265±7	222.0±2.1	0.417±0.003
150	4588±27	2.7±0.03	245±7	210.5±2.2	0.417±0.003

Table 3. Comparison of the optimum electrical properties in this study with similar compositions reported in the literature.

Reference	Composition	K^T	$\tan \delta$ (%)	d_{33} (pC/N)	Q_m	k_p
Takahashi et al. [11]	62PMN-38PT	2930	-	-	~90	-
Takahashi et al. [10]	65.25PMN-33.5PT-1.25PMS	~4000	-	-	~300	-
Takahashi et al. [11]	57PMN-38PT-5PMS	2260	-	-	~725	-
Nadoliisky et al. [22]	46PZ*-47PT-7PMS (2 mole Sr doped)	~1600	0.4	-	~1000	~0.420
Aydin [12]	60PMN-30PT-10PMS	~3389	2.2	195	400	0.367
This Study	63PMN-31PT-6PMS	4800	2.5	270	229.7	0.418

*PZ: PbZrO₃

4. Conclusion

In this study, firstly, the physical and electrical properties of PMN-PT-PMS ceramics sintered at 1175 °C for different periods of time were examined. In characterization studies conducted on sintered samples, it was observed that a sintering time of 60 min resulted in lower density values compared to longer periods. The density values obtained for sintering times of 90, 120, and 150 min were around 97.5-98.0%. However, when the sintering time was 150 min, an undesired pyrochlore phase was formed in addition to perovskite structure. The reason for the formation of the pyrochlore phase may be the increase in the volatility of PbO during long sintering time. The fact that the density decreased slightly when sintered for 150 min also supported this idea. XRD analyzes showed that the rhombohedral phase was dominant compared to the tetragonal phase in all samples sintered for different times.

Experimental results revealed that the density, formation of crystalline phases, piezoelectric and dielectric properties of ceramics are sensitive to sintering time. Optimum electrical properties ($d_{33}=270$ pC/N, $K^T=4800$, $k_p=0.418$, $\tan \delta=2.5\%$ and $Q_m=229.7$) were obtained for the samples sintered at 1175 °C for 90 min. This result is a reflection of the high density, low tetragonality and decrease in the amount of pyrochlore phase.

Acknowledgement

This study was derived from the M.Sc. thesis titled "Determination of Optimal Sintering Regime for PMN-PT-PMS [Pb(Mg,Nb)O₃-PbTiO₃-Pb(Mn,Sb)O₃] Piezoelectric Ceramics" prepared by Osman Düzen under the supervision of Prof. Dr. Volkan Kalem.

Author's Contributions

Osman Düzen: Drafted the manuscript, performed the experiments and result analyses.

Volkan Kalem: Supervised the experiments' progress, result interpretation and wrote the final manuscript.

Ethics

There are no ethical issues after the publication of this manuscript.

References

[1]. Damjanovic, D, Muralt, P, Setter, N. 2001. Ferroelectric Sensors. *IEEE Sensors Journal*; 1(3): 191-206.

[2]. Swartz, SL and Shrout, TR. 1982. Fabrication of perovskite lead magnesium niobate. *Materials Research Bulletin*; 17(10): 1245-1250.

[3]. Choi, SW, Shrout, TR., Jang, SJ, Bhalla, A.S. 1989. Dielectric and pyroelectric properties in the Pb(Mg_{1/3}Nb_{2/3})O₃-PbTiO₃ system. *Ferroelectrics*; 100: 29-38.

[4]. Inada, M. 1977. Analysis of the formation process of the piezoelectric PCM ceramics. *National Technical Report (Matsushita Elect. Ind. Co.)*; 27(1): 95-102.

[5]. Bouquin, O, Lejeune, M, Boilot, JP. 1991. Formation of the perovskite phase in the PbMg_{1/3}Nb_{2/3}O₃-PbTiO₃ system. *Journal of the American Ceramic Society*; 74(5): 1152-1156.

[6]. Guha, JP. 1999. Reaction chemistry and subsolidus phase equilibria in lead-based relaxor systems: Part I - Formation and stability of the perovskite and pyrochlore compounds in the system PbO-MgO-Nb₂O₅. *Journal of Materials Science*; 34(20): 4985-4994.

[7]. Shrout, TR, Swartz, SL. 1983. Dielectric-properties of pyrochlore lead magnesium niobate. *Materials Research Bulletin*; 18(6): 663-667.

[8]. Wakiya, N, Saiki, A, Ishizawa, N, Shinozaki, K, Mizutani, N. 1993. Crystal-growth, crystal-structure and chemical-composition of a pyrochlore type compound in lead-magnesium-niobium-oxygen system. *Materials Research Bulletin*; 28(2): 137-143.

[9]. Wakiya, N, Kim, B.H, Shinozaki, K, Mizutani, N. 1994. Composition range of cubic pyrochlore type compound in lead magnesium niobium oxygen system. *Nippon Seramikusu Kyokai Gakujutsu Ronbunshi-Journal of the Ceramic Society of Japan*; 102(6): 612-615.

[10]. Takahashi, S, Sasaki, Y, Kawai, H, Hirose, S. 1996. High-power piezoelectric characteristics in Pb(Mn_{1/3}Sb_{2/3})O₃-Pb(Mg_{1/3}Nb_{2/3})O₃-PbTiO₃ solid solution system. *Isaf '96 - Proceedings of the Tenth IEEE International Symposium on Applications of Ferroelectric*; 1: 2309-2312.

[11]. Takahashi, S, Yamamoto, M, Sasaki, Y. 1998. Nonlinear piezoelectric effect in ferroelectric ceramics. *Japanese Journal of Applied Physics Part 1-Regular Papers Short Notes & Review Papers*; 37(9B): 5292-5296.

[12]. Aydın HS., 2016. Production and Characterization of PMN-PT [Pb(Mg_{1/3}Nb_{2/3})O₃-PbTiO₃] Based Piezoelectric Ceramics (in Turkish), MSc Thesis (Advisor: Kalem, V.), Selçuk University, Graduate School of Natural And Applied Science, Konya.

[13]. Düzen, O, Kalem, V. 2017. Optimizing Structural and Electrical Properties of PMN-PT-PMS Ceramics via Sintering Temperature, *Selcuk University Journal of Engineering, Science and Technology*; 5(2): 144-152.

[14]. Mahdi, RI, Al-Bahnam, NJ, Abbo, AI, Hmood, JK, Majid, WH Abd. 2016. Optimization of sintering temperature for the enhancement of pyroelectric properties of lead-free 0.88(Na_{0.5}Bi_{0.5})TiO₃-0.084(K_{0.5}Bi_{0.5})TiO₃-0.036BaTiO₃ piezoelectric ceramics. *Journal of Alloys and Compounds*; 688: 77-87.

[15]. Zhu, R, Yin, Y, Fang, B, Chen, Z, Zhang, S, Ding, J, Zhao, X, Luo, H. 2016. Optimizing structure and electrical properties of high-Curie temperature PMN-PHT piezoelectric ceramics via tailoring sintering process. *The European Physical Journal-Applied Physics*; 74(3): 30101.

[16]. Liu, L, Fan, H, Ke, S, Chen, X. 2008. Effect of sintering temperature on the structure and properties of cerium-doped 0.94(Bi_{0.5}Na_{0.5})TiO₃-0.06BaTiO₃ piezoelectric ceramics. *Journal of Alloys and Compounds*; 458: 504-508.

[17]. Naceur, H, Megrache, A, El Maaoui, M. 2014. Effect of sintering temperature on microstructure and electrical properties of Sr_{1-x}(Na_{0.5}Bi_{0.5})_xBi₂Nb₂O₉ solid solutions. *Journal of Advanced Ceramics*; 3(1): 17-30.

[18]. Ketsuwan, P, Ngamjarrojana, A, Laosiritaworn, Y, Ananta, S, Yimnirun, R. 2007. Effect of Sintering Temperature on Phase



Formation, Dielectric, Piezoelectric, and Ferroelectric Properties of Nb-Doped $\text{Pb}(\text{Zr}_{0.52}\text{Ti}_{0.48})\text{O}_3$ Ceramics. *Ferroelectrics*; 358: 35-41.

[19]. Wang, CH, Chang, SJ, Chang, PC. 2004. Effect of sintering conditions on characteristics of PbTiO_3 - PbZrO_3 - $\text{Pb}(\text{Mg}_{1/3}\text{Nb}_{2/3})\text{O}_3$ - $\text{Pb}(\text{Zn}_{1/3}\text{Nb}_{2/3})\text{O}_3$. *Materials Science and Engineering B*; 111: 124-130.

[20]. Lente MH, Zanin AL, Vasiljevic J, Dos Santos IA, Eiras JA, Garcia D. 2004. Temperature Coefficient of Piezoelectric Constants in $\text{Pb}(\text{Mg}_{1/3}\text{Nb}_{2/3})\text{O}_3$ - PbTiO_3 Ceramics. *Materials Research*; 7(2): 369-372.

[21]. Hoffmann, MJ., Hammer M, Endriss A, Lupascu DC. 2001. Correlation between microstructure, strain behavior, and acoustic emission of soft PZT ceramics. *Acta Materialia*; 49: 1301-1310.

[22]. Nadoliisky, MM., Vassileva, TK., Vitkov, PB. 1992. Dielectric, Piezoelectric and Pyroelectric Properties of PbZrO_3 - PbTiO_3 - $\text{Pb}(\text{Mn}_{1/3}\text{Sb}_{2/3})\text{O}_3$ Ferroelectric System. *Ferroelectrics*; 129: 141-146.

Comparative Analysis of Alkaline Phosphatase Activity and Aerobic Spore-Forming Bacteria in Pasteurized Milk

Mustafa Oskay^{1*} 

¹ Section of Basic and Industrial Microbiology, Department of Biology, Faculty of Engineering and Natural Sciences, Manisa Celal Bayar University, 45030, Manisa, Türkiye

* mustafa.oskay@cbu.edu.tr

* Orcid No: 0000-0001-8693-5621

Received: 29 April 2024

Accepted: 25 June 2024

DOI: 10.18466/cbayarfbe.1475459

Abstract

The remaining amounts of alkaline phosphatase (ALP) enzyme in pasteurized milk should be within certain limits. High ALP enzyme level may indicate that the milk has not been pasteurized sufficiently or may be due to excessive growth of spore-forming bacteria in the milk. For this purpose, pasteurized milk samples (n=50) taken from local markets of Manisa were screened for ALP activity and spore-forming bacteria. The ALP activity of most pasteurized milk was below the 350 mU/L limit and ranged from 0 to 500 mU/L. ALP activity was found to be high in only 4% of the 50 milk samples analyzed. The presence of spore-forming bacteria was investigated in suspicious and high ALP activity samples and representative colonies of bacteria that were selected and identified based on biochemical tests. All of the isolates were *Bacillus* spp. and *Bacillus cereus* was detected in only one sample. As a result, a positive correlation between ALP activity and the existence of *Bacillus* spp. was observed for pasteurized milk.

Keywords: Alkaline phosphatase, *Bacillus* sp., colourimetric method, quality control, pasteurized milk, spore-forming bacteria.

1. Introduction

The microorganism load of raw milk is quite high, so it may contain pathogens and spoil in a short time. Therefore, consumption of raw milk may cause health problems. Pasteurization is the most widely adopted and effective method that ensures the destruction of all spoilage and pathogenic microorganisms. One of the most important factors that shorten the shelf life of pasteurized milk is the contamination of spore-forming or non-spore-forming bacteria into the product after heat treatments [1]. Such contaminations generally occur during advanced pasteurisation processes, and, the shelf life of the milk is shortened. These pasteurized products offered for consumption directly concern public health and are very important. The shelf life of pasteurized milk is generally linked to raw milk quality and post-pasteurization contamination control [2].

One of the most important quality measures of the milk to be pasteurized is its hygienic quality. In this case, the number of bacteria, bacterial types, and toxins should be considered. During the pasteurisation process, 1% of the bacteria remain alive, meaning that if the conditions

applied to milk are adequately observed, approximately 99% bacterial reduction can be achieved. [3]. Therefore, the type of bacteria is as important as the number of bacteria in raw milk. If the number of thermophile and heat-resistant (thermoduric) bacteria is high, their reduction in the pasteurization norm is quite difficult [1,2]. To increase the microbiological safety of pasteurized milk, it is necessary to remove all pathogens that may be present in it and pasteurization is recommended for this. Thermoduric bacteria isolated from processed dairy products include *Micrococcus*, *Microbacterium*, *Enterococcus*, *Arthrobacter*, *Lactobacillus*, *Streptococcus*; as well as spore formers such as *Paenibacillus*, *Bacillus*, and *Clostridium* [4,5]. The most common *Bacillus* species in fresh pasteurized milk are generally *B. cereus*, *B. licheniformis*, *B. subtilis* and *B. circulans* [6]. *B. cereus* strains and related organisms have been found to cause milk-sweet curdling and creaminess. Other milk spoilage associated with *Bacillus* and other psychrotrophic spore formers is the coagulation of milk proteins as well as the formation of a bitter taste [7,8].

Alkaline phosphatase (ALP) is an enzyme, which is normally present in raw milk. Once milk is pasteurized, this enzyme becomes completely inactive. Therefore, the high amount of ALP remaining in pasteurized milk will indicate that the milk has not been pasteurized under appropriate conditions [9]. ALP shows a slightly higher temperature resistance than pathogenic bacteria, which die at pasteurization time and temperature. According to the European Union (EU) and the Food and Drug Administration (FDA), the recommended ALP level should be below 350 mU/L to ensure the safety of pasteurized milk and extend its shelf life [10,11]. Values higher than this ALP level may result from insufficient pasteurization or contamination with raw milk. Therefore, measuring ALP activity in pasteurized milk is recognized as a method for rapidly determining the quality of milk pasteurization.

The present study aimed to report the investigation of ALP activity and aerobic spore-forming bacteria in pasteurized milk. In addition, within the scope of the study, aerobic spore-forming bacteria analysis of pasteurized milk with cultural methods will be performed to reveal whether there is a correlation with the results obtained with the highest ALP measurement. Thus, it will be revealed whether the appropriate pasteurization conditions are followed in pasteurized milk and whether the high amounts of ALP are of microbial origin or not.

2. Materials and Methods

2.1. Sampling of Pasteurized Milk

Commercially pasteurized cow's milk samples (n=50) were collected from local markets in Manisa province at different time intervals for approximately 2 years (December 2015-August 2017). Each sample consists of approximately 1 L of pasteurized, fat (approximately 3.5%), homogenized cow's milk in plastic, tetrapak or glass bottles. After sampling, each milk sample was placed in an insulated cooler box (approximately 6 °C) and transported to the laboratory no later than 90 minutes (min) after the first sample was taken. Care was taken to ensure that the samples were taken before the expiration date of the pasteurized milk.

2.2. Analysing the Alkaline Phosphatase Activity

ALP hydrolyses colourless substrate *p*-nitrophenyl phosphate (*p*-NPP) to *p*-nitrophenol (*p*-NP) and inorganic phosphate. For the determining ALP activity, a modified method by Chu *et al.* [12] was applied. Briefly; the buffer-substrate solution was prepared with carbonate buffer (10 mM, pH 10.2), containing 1 mM MgCl₂ with 0.2 mM of *p*-NPP in a total of 1.5 mL. Then, 200 µL of well-mixed pasteurized milk was added to 1.5 ml of buffer-substrate solution and this reaction mixture was incubated at 37 °C for 120 min. At

the end of the incubation, 0.5 ml of stopper buffer (0.1 mol NaOH and 5 mmol EDTA) were added and it was rested for 3 min, centrifuged at 1400 rpm for 10 min. The supernatant was transferred to clean cuvettes and without waiting, the absorbance was measured on a 410 nm spectrophotometer. For the comparison, the negative control and positive control, boiled pasteurized milk and raw milk samples were used respectively, in the same amount and reaction conditions. ALP activity was calculated with the formula given below;

$$\text{ALP activity (unite/mL)} = \frac{(A_{410\text{nm test}} - A_{410\text{nm Blank}}) \times B}{C \times D \times E}$$

A= Absorbance read at 410 nm

B= Total reaction volume (mL)

C= Extinction coefficient of *p*-NP (mM), according to standard curve

D=Volume of pasteurised milk sample used (mL)

E= Reaction time (min)

The results obtained were converted to milliunits per litre (mU/L).

2.3. Determination of Aerobic Spore-Forming Bacteria

To determine whether the ALP activity was caused by aerobic spore-forming bacteria (ASFB) in the pasteurized milk samples with higher ALP levels, therefore, laboratory pasteurisation at 63 °C, 40 min (LAB pasteurisation) was performed according to the method of Rankin *et al.* [9] and the results were discussed. In this experiment, ASFB screening was performed on the samples that gave positive ALP results. 1 mL of milk sample (10⁻¹ dilution) in 0.8% physiological saline was transferred in Plate Count Agar (PCA) medium by the pour plate cultivation method and incubated at 30 °C for 48 h. At the end of incubation, bacteria that could grow in the PCA medium were evaluated as ASFB and representative colonies were selected for identification by cultural and biochemical tests.

2.4. Identification of Selected Microorganisms

The liquid cultures (incubated for 48 h at 30 °C) of representative bacteria were subjected to gram staining to determine the gram reaction. API biochemical test kits (BioMérieux, France) are accepted as a reference for identifying bacterial and fungal species. API 20E biochemical tests were applied to selected bacteria. Bacterial cultures transferred to test strips were prepared fresh and applied according to the manufacturer's instructions. At the end of the incubation period, the bacterial genus/species of the isolates were identified using the numerical identification calculation method recommended by the API, through APIWEB-based software.

2.5. Statistical Analysis

All the data was represented as mean \pm standard deviation of the mean (SD) using the statistical software (Minitab® 19).

3. Results and Discussion

Pasteurization is the most widely used method that ensures the destruction of all pathogenic microorganisms in milk and makes it safe for consumption. Milk is ideal for the growth and reproduction of various microorganisms that cause it to spoil prematurely. Since raw milk contains many pathogens, direct consumption is not recommended. Various factors affect the microbiological quality of pasteurized milk, such as the origin of raw milk, the heat treatment used, storage conditions, and the degree

of contamination after pasteurization [3]. The purpose of milk pasteurization is to make milk safe and increase its shelf life to several weeks. However, pasteurized milk is perishable and assessing its quality is one of the most important concerns.

There are several methods for detecting microbial spoilage in dairy products after pasteurization. ALP test method in the dairy industry; can be used in pasteurized milk quality [13]. Since ALP activity is affected by different reaction conditions, it is very important to perform the process under stable reaction conditions and compare the results with the standard curve (Figure 1). In the present study, the measurement values of 50 different pasteurized milk samples analysed with the ALP activity ranged between 0-500 mU/L. ALP activity of the most pasteurised milk was below the limits of 350 mU/L (Figure 2).

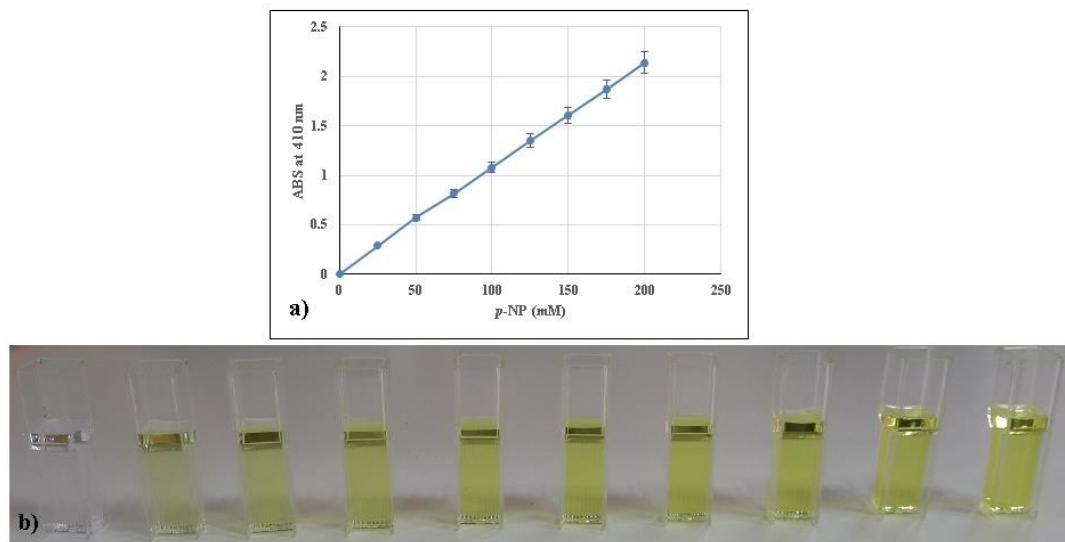


Figure 1. *p*-NP (mM) standard curve (a) and (b); the amounts of *p*-NP seen in the cuvette were 0, 25, 50, 75, 100, 125, 150, 175, 200 and 225 mM, from left to right, respectively.

When the obtained results compared the standard values, it was concluded that 2 of the 50 pasteurized milk samples were above this limit (4%, poor quality), 3 were almost at the upper limit (6%) and the rest were of good quality (90%). The results of ALP activity in pasteurised milk are presented in Figure 2. A study conducted by Rola *et al.* [10], obtained the highest ALP activity in two of 65 samples of pasteurised goat milk about 500 and 700 mU/L. Also, they found that one sample had an activity equal to 350 mU/L. Peng *et al.* [14], explained that the ALP of 451 pasteurized milk was 9.71% contained >350 mU/L. ALP activity by colourimetric method was similar to those studies and supported the present results.

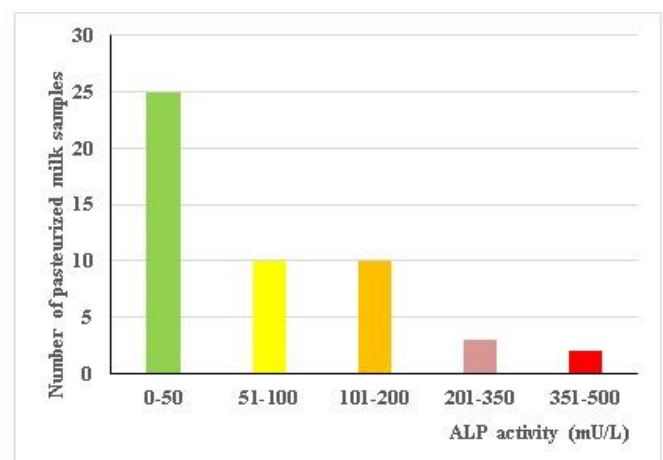


Figure 2. ALP activity of pasteurized milk samples.

To determine whether the ALP activity was caused by ASFB in the pasteurized milk samples with higher ALP

levels, therefore, laboratory pasteurisation at 63 °C, 40 min was applied. Five samples with high ALP activity were selected and subjected to LAB pasteurization, and then ASFB bacteria were isolated using a PCA medium. After laboratory pasteurization, firstly, ALP activities were measured again for the five samples and the value was found negative for 3 samples. According to the ALP activity results of these 3 samples, it was estimated that high ALP activity may be due to inadequate pasteurization or storage conditions. Spore counts from the remaining 2 ALP positive samples were determined to be approximately between 1.0×10^1 and 4.0×10^2 cfu/mL. Therefore, it was concluded that the high ALP

activity in these 2 samples may be caused by spore-forming bacteria. As a result of all isolations, 30 different isolates were obtained from the two samples and those that were similar to each other were separated and 5 strains that were assumed to represent all were selected and identified by biochemical tests. All bacteria selected for identification were gram-positive and according to the API test, the selected 5 isolates showed similarity rates ranging from 90 to 99.9%, 4 were *Bacillus* sp. the other was evaluated as *Bacillus cereus* (Table 1.).

Table 1. API 20E biochemical test results of the selected isolates.

Isolate	ONPG	ADH	LDC	ODC	CIT	H2S	URE	TDA	IND	VP	GEL	GLU	MAN	INO	SOR	RHA	SAC	MEL	AMY	ARA	Possible genus/species
PALP1	-	+	-	-	-	-	-	-	-	-	+	+	-	+	-	-	+	-	+	-	<i>Bacillus cereus</i>
PALP2	+	-	-	-	-	-	-	-	-	+	-	+	-	-	-	-	-	-	-	-	<i>Bacillus</i> sp.
PALP3	-	+	-	-	V	-	-	-	-	-	+	-	-	-	-	-	+	-	-	-	<i>Bacillus</i> sp.
PALP4	+	-	-	-	-	-	+	-	-	+	-	+	-	-	-	-	-	-	-	-	<i>Bacillus</i> sp.
PALP5	+	-	-	-	+	-	+	-	-	+	+	-	-	-	-	-	-	-	-	-	<i>Bacillus</i> sp.

* (+): positive, (-): negative, (V): variable.

Peng *et al.* [14] determined a positive correlation between ALP activity and aerobic plate count, *Bacillus* and thermophilic *Bacillus* abundance, for pasteurized milk. These results confirm the current study. In another study, *Bacillus* spp. *Pseudomonas* spp. and *Acinetobacter* spp. have been identified from pasteurized milk samples [15]. In a microbiological study conducted to determine the quality of cooled raw milk, processed milk and dairy products; *Lactococcus lactis* (27.3%), *Enterobacter kobei* (14.8%), *Serratia ureilytica* (8%), *Aerococcus urinaeequi* (6.8%) and *Bacillus licheniformis* (6.8%) were detected [7]. A comprehensive microbiological analysis of 39 pasteurized milk samples, it was noted that the number of TASS was found below the spoilage limit of 10^7 cfu/mL, which is higher than the present study [16].

In this study, isolated aerobic spore-forming bacteria had higher ALP activity of pasteurized milk at a rate of 4% (2 samples). It was concluded that the other 96% (48 samples) complied with the standards. It is thought that the spore contamination in samples may result from inadequate adherence to pasteurization temperature and time or post-pasteurization processes. According to a previously reported study [17]; by contaminating pasteurized milk with various portions of raw milk from 0.001% to 0.1%, an ALP concentration gradient ranging from 3.5-350 mU/L was obtained. Therefore, to ensure that pasteurized milk is safe, it is important to perform pasteurization correctly and prevent post-pasteurization contamination. Additionally, more importance should be given to ensuring personnel hygiene in pasteurized milk facilities.

While foodborne pathogens always pose a threat to public health, determining microbial viability with

traditional detection approaches has many drawbacks. Application of the ALP assay is a reliable, rapid detection technique that monitors the quality of pasteurized milk. Moreover, this method does not require as much sampling compared to traditional approaches and allows us to obtain results in a short time. Therefore, the data obtained within the scope of this study is very valuable, as it will make significant contributions to the literature in this field.

4. Conclusion

Overall, the ALP activity of pasteurized cow's milk was determined and from the positive samples, aerobic spore-forming bacteria were identified. A positive correlation between ALP activity and the existence of *Bacillus* sp. was observed for pasteurized milk. As a result, compared to the colony counting technique, the ALP method significantly reduces the analysis time and provides very useful information in researching the quality control of pasteurized milk. However, a combination of techniques is required to validate the desired sensitivity and specificity in the determination of ALP activity. Additionally, identification of *Bacillus* sp. at the species level should be supported by molecular studies.

Author's Contributions

Mustafa Oskay: Designed and performed the experiments, analysed the results, and wrote the article.

Ethics

There are no ethical issues after the publication of this paper.

Declaration of Competing Interest

The author declares that he has no conflict of interest regarding the content of this manuscript.

Data Availability

The supporting data will be made available on reasonable request.

References

- [1]. Mahari, T, Gashe, BA. 1990. A survey of the microflora of raw and pasteurized milk and the sources of contamination in a milk processing plant in Addis Ababa, Ethiopia. *Journal of Dairy Research*; 57(2):233–238.
- [2]. Meunier-Goddik, L, Sandra, S. 2016. Liquid milk products: pasteurized milk *Encyclopedia of Dairy Sciences*; pp 274-280. doi.org/10.1016/b978-0-08-100596-5.00876-3.
- [3]. Sarkar, S. 2015. Microbiological considerations: pasteurized milk. *International Journal of Dairy Science*; 10(5):206–218.
- [4]. Cousin, MA. 1982. Presence and activity of psychrotrophic microorganisms in milk and dairy products: a review. *Journal of Food Protection*; 45(2):172–207.
- [5]. Ralyea, RD, Wiedmann, M, Boor, KJ. 1998. Bacterial tracking in a dairy production system using phenotypic and ribotyping methods. *Journal of Food Protection*; 61(10):1336–1340.
- [6]. Crielly, EM, Logan, NA, Anderton, A. 1994. Studies on the *Bacillus* flora of milk and milk products. *Journal of Applied Bacteriology*; 77(3):256–263.
- [7]. Ribeiro Júnior, JC, de Oliveira, AM, Silva, RFG, Tamanini, ALM, de Oliveira, VB. 2018. The main spoilage-related psychrotrophic bacteria in refrigerated raw milk. *Journal of Dairy Science*; 101(1):75–83.
- [8]. Boor, KJ, Brown, DP, Murphy, SC, Kozłowski, SM, Bandler, DK. 1998. Microbiological and chemical quality of raw milk in New York State. *Journal of Dairy Science*; 81(6):1743–1748.
- [9]. Rankin, SA, Christiansen, A, Lee, W, Banavara, DS, Lopez-Hernandez, A. 2010. Invited review: the application of alkaline phosphatase assays for the validation of milk product pasteurization. *Journal of Dairy Science*; 93(12):5538–5551.
- [10]. Rola, JG, Sosnowski, M. 2010. Determination of alkaline phosphatase activity in milk and milk products by fluorimetric method. *Bulletin of the Veterinary Institute in Pulawy*; 54(4):537–542.
- [11]. Albillos, SM, Reddy, R, Salter, R. 2011. Evaluation of alkaline phosphatase detection in dairy products using a modified rapid chemiluminescent method and official methods. *Journal of Food Protection*; 74(7):1144–1154.
- [12]. Chu, YH, Yu, XX, Jin, X, Wang, YT, Zhao, DJ, Zhang, P, Sun, GM, Zhang, YH. 2019. Purification and characterization of alkaline phosphatase from lactic acid bacteria. *RSC Advances*; 9(1):354–360.
- [13]. Payne, C, Wilbey, RA. 2009. Alkaline phosphatase activity in pasteurized milk: A quantitative comparison of Fluorophos and colourimetric procedures. *International Journal of Dairy Technology*; 62(3):308–314.
- [14]. Peng, Z, Li, Y, Yan, L, Yang, S, Yang, D. 2023. Correlation analysis of microbial contamination and alkaline phosphatase activity in raw milk and dairy products. *International Journal of Environmental Research and Public Health*; 20(3). doi: 10.3390/ijerph20031825.
- [15]. Ternström, A, Lindberg, AM, Molin, G. 1993. Classification of the spoilage flora of raw and pasteurized bovine milk, with special reference to *Pseudomonas* and *Bacillus*. *Journal of Applied Bacteriology*; 75(1):25–34.
- [16]. Angelidis, AS, Tsiota, S, Pexara, A, Govaris, A. 2016. The microbiological quality of pasteurized milk sold by automatic vending machines. *Letters in Applied Microbiology*; 62(6) 472–479.
- [17]. Gerokomou, V, Rozos, G, Demertzis, P, Akrida-Demertzi, K. 2022. Assessment of seasonal and diurnal variations of alkaline phosphatase activity in pasteurized milk. *Applied Sciences (Switzerland)*; 12(10). doi: 10.3390/app12104833.

Coffee Active Ingredient Loaded Biopolymer Nanoparticles: Synthesis and Characterization

Özge Vardar¹ , Ayça Mehmetoğlu Al² , Yeliz Yıldırım^{1,3*} 

¹ Department of Chemistry, Faculty of Science, Ege University, Izmir, Türkiye

² Department of Biotechnology, Graduate School of Natural and Applied Science, Ege University, Izmir, Türkiye

³ Center for Drug R&D and Pharmacokinetic Applications (ARGEFAR), Ege University, Izmir, Türkiye

* yeliz.yildirim@ege.edu.tr

* Orcid No: 0000-0002-3014-4510

Received: 6 March 2024

Accepted: 27 June 2024

DOI: 10.18466/cbayarfb.1448091

Abstract

Cafestol (CFS) is present in unfiltered coffee types and exhibits antidiabetic, anti-inflammatory and anticarcinogenic properties. The ionic gelation method was used to synthesise CFS-loaded chitosan (CS), and alginate (ALG) nanoparticles with high loading efficiency. The characterization, thermal properties and surface morphology of CFS-loaded biopolymer nanoparticles were carried out by FTIR, TGA and SEM, respectively. The encapsulation efficiency of the synthesised CFS-loaded biopolymer nanoparticles was found to be as 53% (CFS-loaded ALGNPs) and 92% (CFS-loaded CSNPs) by high-pressure liquid chromatography. The particle sizes determined using Malvern Zeta Sizer Ultra were 97 ± 4.04 (CFS-loaded CSNPs) and 81 ± 6.51 (CFS-loaded ALGNPs).

Keywords: Alginate, Cafestol, Chitosan, Drug Delivery Systems, Nanoparticle

1. Introduction

Coffee, a beverage widely consumed worldwide, is a complex substance that consists of various compounds. The structure of coffee indicates the presence of bioactive diterpene cafestol (CFS)/kahweol (CWL), which is one of the terpene species, as well as nearly 30 acids, such as chlorogenic and citric acids [1]. The biological properties of these compounds have been studied as a mixture of both because of the difficulty of isolating and separating CFS and CWL diterpenes from coffee as well as the unstable nature of CWL when purified [2]. Studies have focused on the antidiabetic, anti-inflammatory, and anticarcinogenic properties of CFS (Fig. 1).

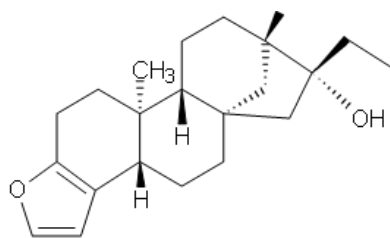


Figure 1. Chemical structure of CFS [2].

The anti-angiogenic effects of CFS palmitate and CWL palmitate (KP) were evaluated in an in-vitro animal model of angiogenesis. The results appeared that inhibited both compounds angiogenesis steps on human microvascular endothelial cells (HMVECs) [3]. In another study, INS-E1 rat insulin cells were used to investigate whether CFS increased insulin secretion from β cells in the short and long term. Insulin secretion increased by 12%–16% depending on the concentration in a 1-h exposure to CFS, and secretion increased by 34%–68% in a 72-h exposure. The results revealed that CFS may prevent Type-2 diabetes (T2D) in coffee drinkers [4]. Mellbye et al. investigated glucose uptake in cells and its effect on T2D by feeding male rats with a daily meal supplemented with 1.1 (high), 0.4 (low) or 0 (control) mg CFS for 10 weeks. At the end of the 10-week period, fasting plasma glucose was 28%–30% lower in the CFS groups than that in the control group, and insulin secretion increased by 75%–87% compared with the control group. CFS exhibits antidiabetic properties and can be used as a potential antidiabetic drug [5]. Studies have revealed that CFS exhibits antidiabetic properties [6] as well as anticarcinogenic effects [7].

The head and neck cancer cells were treated with CFS and cisplatin to investigate whether CFS would increase the effectiveness of the chemotherapeutic agent cisplatin. Three cell lines, namely SCC25, CAL27 and FaDu, were used in the experiments, and depending on the dose, CFS inhibited carcinoma cell viability in all cell lines. Furthermore, in combination experiments using radiation, cells were first treated with CFS and subsequently irradiated. Although the combined treatment was effective in SCC25 and CAL27 cell lines, successful results were not obtained in the FaDu cell line [8]. A study evaluated the antitumor properties of CFS by examining its effect on four leukaemia cell lines, namely NB4, K562, HL60, and KG1 and revealed that it showed the highest cytotoxicity against HL60 and KG1 cells. The results showed that they were close to those obtained after the exposure of the HL60 cell line to the antileukemic drug cytarabine (Ara-C). Additionally, the co-treatment of CFS and Ara-C reduced HL60 cell viability compared to when either drug was given alone [9].

Lee et al. investigated the effects of CWL and CFS on oxidative stress and DNA damage in NIH3T3 cells. When NIH3T3 cells were treated with CWL and CFS, cytotoxicity, lipid peroxidation and production of reactive oxygen species reduced considerably in a dose-dependent manner. The results indicated that CWL and CFS could effectively protect against oxidative stress and DNA damage, and diterpenes functioned as antioxidants [10]. To combine the antibacterial and anti-inflammatory properties of zinc oxide nanoparticles with the antimicrobial properties of CFS, a chitosan (CS)-coated nanosystem was developed. The antibacterial activity of this system was investigated in *Staphylococcus aureus*, *Bacillus cereus*, *Pseudomonas aeruginosa*, and *Escherichia coli* bacteria, and the results revealed that ZnO, CS-ZnO and CFS-CS-ZnO nanoparticles inhibited the growth of *S. aureus*, *B. cereus*, and *E. coli*. The antibacterial activity was improved by coating CFS and ZnO nanoparticles with CS [11].

CS, obtained by the deacetylation of chitin is a biopolymer that exhibits excellent antibacterial, biorenewable, biocompatible, biodegradable, antimicrobial and antitumor properties [12,13]. Various types and combinations of CS as a drug delivery system have been investigated in studies such as doxorubicin-loaded CS nanobubbles [14], 5-fluorouracil-loaded CS microspheres [15], N-acetylcysteine-loaded CS-coated liposome [16], amiodoran-loaded CS nanoparticles [17], and Docetaxel-loaded CS nanoparticles [18]. Nanoparticles have been preferred more than other carriers because of their high stability and high carrier capacity, facilitating the use of both hydrophilic and hydrophobic substances, and allowing controlled drug release [19].

Alginate (ALG) is a linear copolymer containing blocks of β -D-mannuronic acid and α -L-guluronic acid residues linearly linked by 1,4-glycosidic bonds and is a biocompatible polymer that is widely used in carrier systems as well as CS [20]. The presence of monomer units in ALG considerably influences drug release properties. The β -D-mannuronic acid groups provide excellent thickening, whereas the α -L-guluronic acid content contributes to superior gelling properties [20]. ALG nanoparticles also widely investigated for drug delivery systems as well, especially as anticarcinogenic drug carrier. One of the latest studies are, Docetaxel (DTX)-loaded sodium ALG nanoparticles used for target colon cancer cells [21], Exemestane (EXE) drug used in breast cancer treatment was loaded on ALG nanoparticles [22], Cabazitaxel (CAB)-loaded poly(alkyl cyanoacrylate) (PACA) nanoparticles were encapsulated in alginate microspheres prepared aiming to delay anticancer drug absorption and reduce toxic side effects [23], and Sunitinib (STB) loaded alginate nanoparticles studied for enhancing oral bioavailability of STB which used for gastrointestinal stromal tumor [24]. Chlorhexidine loaded ALG nanoparticles also studied in dentistry for throat infection [25].

Within the scope of the study, it was aimed to load CFS (Fig. 1), which has been proven to exhibit anticancer, anti-inflammatory and antidiabetic properties, onto biocompatible polymer nanoparticles CS (CSNPs) and ALG (ALGNPs) and to carry out optimization and characterization studies of these biopolymer nanoparticles.

2. Materials and Methods

2.1. Materials

Low-molecular-weight CS powder (molecular weight: 50–190 kDa, 75%–85% deacetylated) and sodium ALG powder were obtained from Sigma-Aldrich Chemical Co. Ltd. Sodium tripolyphosphate (TPP) was procured from Alfa Aesar by Thermo Fisher Scientific, and CFS a crystalline solid, purity $\geq 98.0\%$ obtained from Cayman Chemicals. All chemicals were analytical grade.

2.2. Equipments

A FTIR spectrometer (Spectrum Two, Pelkin Elmer, UK.) was used in the range $4000\text{--}500\text{ cm}^{-1}$, and 10 scans were performed at a resolution of 4 cm^{-1} to detect the functional groups of all formulations. The nanoparticle samples were prepared with KBr pellets to analyse the chemical interactions between CFS and polymer matrix.

Average particle sizes were measured with multiangle dynamic light scattering using a Zetasizer (Malvern Instruments, Herrenberg, Germany). Purified water used as a medium for nanoparticle solution during analysis.

For the zeta potential same conditions were conducted and all analysis measured three times at 25°C.

The shape and surface morphology of CFS-loaded CSNPs, and CFS-loaded ALGNPs, were determined through scanning electron microscopy (SEM, Thermo Scientific Apreo S).

Thermogravimetric (TG) curves were obtained using a Diamond TG/DTA analyser (Pelkin Elmer, UK) from 30°C to 600°C, under a N₂ atmosphere at a 10°C/min heating rate for CFS-loaded nanoparticles.

2.3. Preparation of Nanoparticles

2.3.1 Preparation of CS Nanoparticles and CFS-loaded CS Nanoparticles (CSNPs / CFS-loaded CSNPs)

CSNPs were synthesized as described by Calvo et al. [26, 27]. CS (50 mg) was dissolved in the CH₃COOH (1% v/v, 25 ml) at room temperature under magnetic stirring until the formation of an opalescent suspension. The pH of the resulting solution was adjusted to 4.6–4.8 using the NaOH solution. CS nanoparticles were spontaneously obtained on the dropwise addition of TPP aqueous solution (CS to TPP weight ratio of 2:1 and TPP concentration is 7.5 mg/ml) to CS solution under constant magnetic stirring at room temperature. Nanoparticles were collected through centrifugation at 4°C before dried in a vacuum oven.

For preparing CFS-loaded CS nanoparticles, the CFS solution (100 µg/ml, 2 ml) was added before the TPP solution. The remaining processes were identical to the preparation of CS nanoparticles.

2.3.2 Preparation of ALG and CFS-loaded ALG Nanoparticles (ALGNPs/CFS-loaded ALG-NPs)

The method used to prepare ALG nanoparticles was modified from Rajaonarivony et al. [28]. Here, 2 mL of aqueous calcium chloride was added dropwise to 10 mL aqueous sodium ALG (3 mg/ml) with stirring at 1100 rpm. The nanoparticle solution stirred for 24h to obtain homogenous and uniform particle distribution. Nanoparticles were collected through centrifugation at 4°C before drying in a vacuum oven.

To prepare CFS-loaded alginate nanoparticles, the CFS solution (100 µg/ml, 2 ml) was added before the calcium chloride solution. The remaining processes were identical to the preparation of ALG nanoparticles.

2.4 HPLC

2.4.1 HPLC Conditions

The HPLC analysis method was modified from a previous study [29, 30]. The PDA detector HPLC system and the ACE C18 column (ACE; 250 × 4.6 mm, 5 µm) were used for the calibration curve of CFS. As the mobile

phase, a mixture of acetonitrile and water was prepared at a ratio of 55:45 (v/v). The system was run with an isocratic flow rate of 0.9 mL/min rate, the injection amount was 20 µL, and the detector was set at 230 nm. The temperature of the column was 25°C, while the temperature for the autosampler was 30°C. In accordance with ICH guidelines Q2(R1), the present method was validated and found to be suitable for its intended purpose[31].

2.4.2 Preparation of stock solutions and standard working solutions

The stock solution of CFS (100 µg/mL) was prepared by dissolving 5.0 mg of drug in 50.0 mL ethanol. The standard solutions were stored at 4°C ± 1°C in a clear glass volumetric flask and lightly protected with an aluminium foil. The calibration curves of CFS concentrations of 0.5, 1.0, 5.0, 10.0, 20.0, 40.0, 60.0, 80.0 and 100.0 µL/mL in the working solution were determined. In the dilute solution, the stock solution was further diluted to make these working solutions daily. All samples were filtered through a 0.2 µm pore size filter (PTFE) followed by injection.

2.4.3 Calibration curve/Linearity

Analytical methods are linear when their results are directly proportional to variations in analyte concentration within a given range of concentrations or through a well-defined mathematical transformation. Linearity was analysed by plotting a calibration curve between concentration and areas obtained from standard solutions at ten different CFS concentrations (0.5–100.0 µg/mL in ethanol). Moreover, linearity was evaluated using least-square regression analysis, which utilizes a linear regression model.

2.4.4 Encapsulation efficiency

The encapsulation efficiencies (EE) of CFS-loaded CS, and ALG nanoparticles were determined after analysis in the HPLC (in triplicate) and calculated using the following equation:

$$EE (\%) = \frac{\text{Total amount of drug} - \text{Amount of free drug}}{\text{Total amount of drug}} \times 100 \%$$

3. Results and Discussion

CFS is a diterpene found in the structure of coffee, whose biological activities have been shown in various studies [4,5,6]. It was successfully encapsulated into CS and ALG biopolymers nanoparticles for the first time to ensure the continuity of the effectiveness of CFS for a long time. CFS-loaded CSNPs and CFS-loaded ALGNPs were synthesised by using the ionic gelation method with 64%, and 60% reaction yields, respectively.

Particle size and zeta potential of the synthesized nanoparticles were determined in solution using the DLS method. The results are revealed in Table 1. The results

obtained showed that the sizes of CSNPs and ALGNPs were 62 ± 3.92 and 61 ± 6.03 nm, by loading CFS into their structures, they increased to 97 ± 4.04 nm (for CFS-loaded CSNPs) and 81 ± 6.51 nm (for CFS-loaded ALGNPs). In the synthesis of CSNPs and ALGNPs, were founded that the synthesis conditions affect the size and reaction efficiency of the nanoparticle [32]. Therefore, optimisation studies investigated parameters, such as polymer molecular weight (low and medium molecular weight) and concentration, polymer-crosslinker ratio, pH, and drop rate were investigated. The results revealed that the size of the nanoparticle increased with the increase in the molecular weight and concentration of CS. Similarly, the particle size increased in the pH:5.5–5.6 range compared with pH 4.6–4.8. Kush et al. examined CS and TPP concentrations, CS:TPP ratios, temperature, mixing speed, and pH parameters to optimise the size of CSNPs. The CSNPs size were optimised as 159.2 ± 3.31 nm [33]. Çakır et al. (2020) investigated the effect of CS, TPP, Timol, Tween 80 concentrations and temperature parameters on the nanoparticle size in the synthesis of nanoparticles loaded with Timol and Tween 80 and revealed that the particle size increased with the increase in CS and TPP concentrations [34]. The optimum conditions for the synthesis of CFS-loaded CSNPs were low-molecular-weight CS concentration at 0.2 mg/ml; TPP concentration at 0.75 mg/ml; the pH was determined as a working range of 4.6–4.8 and a drop rate of 20 s. The particle size was 62 ± 3.92 nm for CSNPs and 97 ± 4.04 nm for CFS-loaded CSNPs (Table 1).

Sagis et al. (2014) investigated the effect of CaCO_3 and CaCl_2 crosslinkers on the size of ALG nanoparticles. The results of the study revealed that CaCO_3 was more effective than CaCl_2 as a crosslinker in reducing the particle size to nanoscale [35]. Mokhtari et al. (2017) studied the effect of the CaCl_2 concentration on the particle size and encapsulation efficiency in mint-phenolic-extract-loaded ALG nanospheres. The results revealed that the mean particle size decreased, and the encapsulation efficiency increased with the increase in the CaCl_2 concentration [36]. The optimum conditions were determined as 3.0 mg/mL ALG concentration, 3.35 mg/mL CaCl_2 concentration and the use of dripping rate every 20 s in our synthesis of CFS-loaded ALGNPs. Although the particle size was 61 ± 6.03 nm for ALGNPs, this value increased to 81 ± 6.51 nm for CFS-loaded ALGNPs (Table 1).

The zeta potentials of CFS-loaded biopolymer nanoparticles are shown in Table 1. Zeta potential, a physicochemical parameter expressing the stability of nanoformulations, is used to indirectly report the surface net charge. While extreme negative or positive values of zeta potential cause large repulsive forces, repulsion between particles with similar electrical charge prevents agglomeration. Depending on the suspension type, the distribution is a stable distribution system because of

sufficient electrostatic repulsion between nanoparticles with a zeta potential of ± 30 mV [37]. The zeta potentials for CSNPs, ALGNPs, CFS-loaded CSNPs and CFS-loaded ALGNPs were -25.8 ± 5.97 mV, -9.6 ± 4.67 mV, -10.2 ± 3.14 mV and -25.9 ± 1.82 mV, respectively (Table 1). According to the zeta potential results, the stability order of the synthesised CFS-loaded polymer NPs in our study was ALGNPs < CFS-loaded CSNPs < CSNPs < CFS-loaded ALGNPs.

Table 1. Particle sizes, Zeta potentials, and encapsulation efficiencies of CSNPs, ALGNPs, ALG–CSNPs, and CFS-loaded nanoparticles.

Formulation Code	Particle Size (nm)	Zeta Potential (mV)	Encapsulation Efficiency (%)
CSNPs	62 ± 3.92	-25.8 ± 5.97	-
CFS-loaded CSNPs	97 ± 4.04	-10.2 ± 3.14	92 ± 2.1
ALGNPs	61 ± 6.03	-9.6 ± 4.67	-
CFS-loaded ALGNPs	81 ± 6.51	-25.9 ± 1.82	53 ± 1.8

Bakhshi et al. (2017) reported the zeta potentials of ALGNPs and immunoglobulin-loaded ALGNPs as -26.8 and -36.9 mV, respectively. They concluded that the negative surface charge of sodium ALGNPs can be attributed to the presence of carboxyl groups of ionised alginate molecules on the surface of nanoparticles. The zeta potential parameter represents the high surface charge of nanoparticles, which results in strong repulsive interactions between nanoparticles in dispersion [38]. Spadari et al. revealed that the zeta potential values of ALGNPs and miltefosine-loaded ALGNPs were measured to be -36.2 ± 6.8 and -39.7 ± 5.2 mV, respectively. They also reported that the uptake of negatively charged nanoparticles into the cell by the mucosa occurs through the nonspecific adsorption process of nanoparticles on the cell membrane and the formation of nanoparticle aggregates [39].

Consequently, according to the zeta potential results, the stability order of the synthesised CFS-loaded polymer NPs in our study was CFS-loaded CSNPs (-10.2 ± 3.14) < CFS-loaded ALGNPs (-25.9 ± 1.82).

3.1 Encapsulation Efficiency

The amount of free CFS from the reaction medium after synthesis was determined using the HPLC analysis method under PDA detector, the ACE C18 column (ACE; 250×4.6 mm, $5 \mu\text{m}$) the mobile phase which contains a mixture of acetonitrile and water at a ratio of 55:45 (v/v) conditions in order to determine the encapsulation efficiency. Figure 2 shows the calibration chart drawn in ethanol environment.

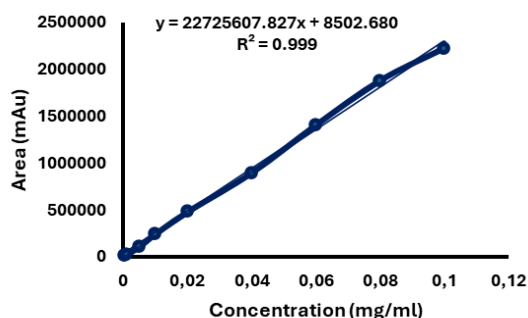


Figure 2. Calibration curve of CFS in ethanol.

The encapsulation efficiencies of CFS to CSNP and ALGNP were calculated by using free CFS amounts obtained the HPLC analyses results. The encapsulation efficiency of CFS-loaded CSNPs and CFS-loaded ALGNPs are found 92 ± 2.1 and 53 ± 1.8 , respectively. The obtained results are summarized in Table 1.

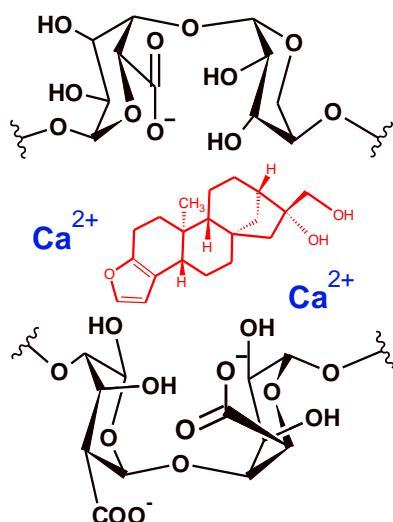


Figure 3. Probable interaction between ALG and CaCl_2 .

The encapsulation efficiency of CS nanoparticles is 1.75 times higher than that of ALG nanoparticles. When the molecular structures are examined, it is possible that the protonated amine groups in the structure of CS interact with the partial negative OH groups in the structure of CFS. On the other hand, the negative OH groups in the structure of the ALG polymer are expected to have a reducing effect on the encapsulation of CFS into the polymeric nanoparticle. There are some studies in the literature that predict the interaction between CS with TPP and ALG with CaCl_2 [40, 41]. In the light of these studies, the possible interactions between CFS to ALGNP or CSNP are shown in Figures 3 and 4, respectively.

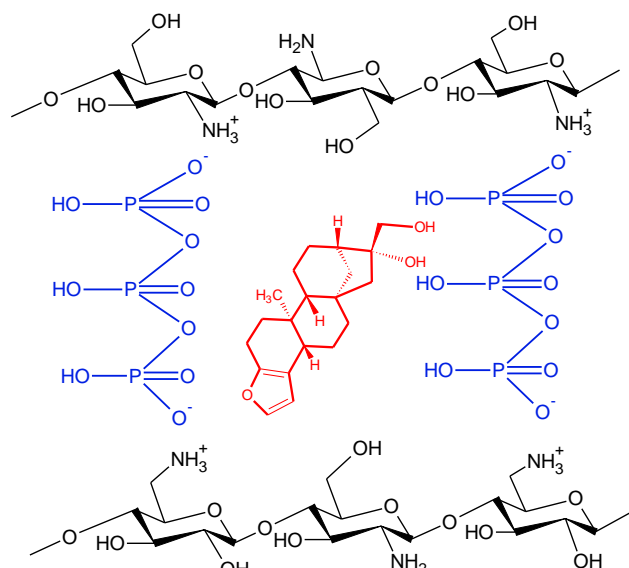


Figure 4. Probable interaction between Chitosan (CS) NPs and CFS.

3.1 FTIR analysis

The spectra of pure CFS, pure CS, pure ALG, CSNPs, ALGNPs, CFS-loaded CSNPs and CFS-loaded ALGNPs obtained by using FTIR spectroscopy to confirm CFS-loaded nanoparticles (Figures 5, and 6).

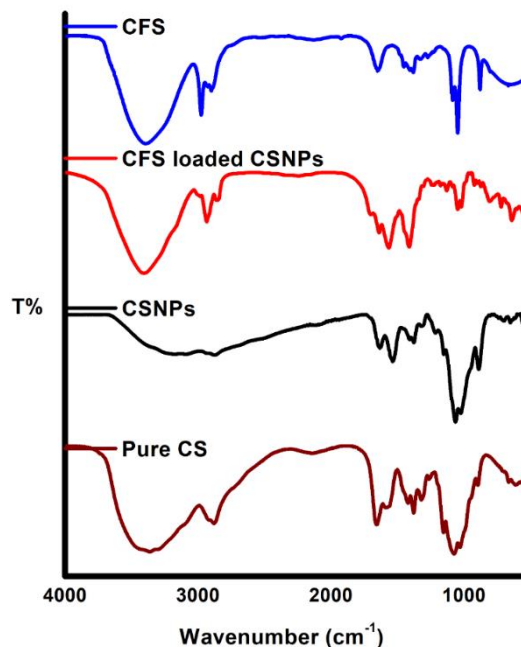


Figure 5. FTIR spectra of pure CS, pure CFS, CSNPs and CFS loaded CSNPs.

The FTIR spectra of pure CS, pure CFS, CSNPs and CFS loaded CSNPs are displayed in Figure 5. The peak at $3500\text{--}3200\text{ cm}^{-1}$ was attributed to $-\text{NH}_2$ and $-\text{OH}$ groups. This broad peak was attributed to the increased

hydrogen bonding in CSNPs resulting from the interaction between the NH_3 group of CS and the $\text{P}_2\text{O}_5^{-1}$ group of TPP (Figure 4). The peaks at 1624 and 1532 cm^{-1} can be interpreted as the N–H vibration of the $-\text{NH}_3^+$ group and the C–H vibration of the alkyl group, respectively. The absorption peaks approximately 1083 and 890 cm^{-1} may be attributed to C–O–C anti-symmetric stretching at the β -(1-4)-glycosidic linkages of CS [42].

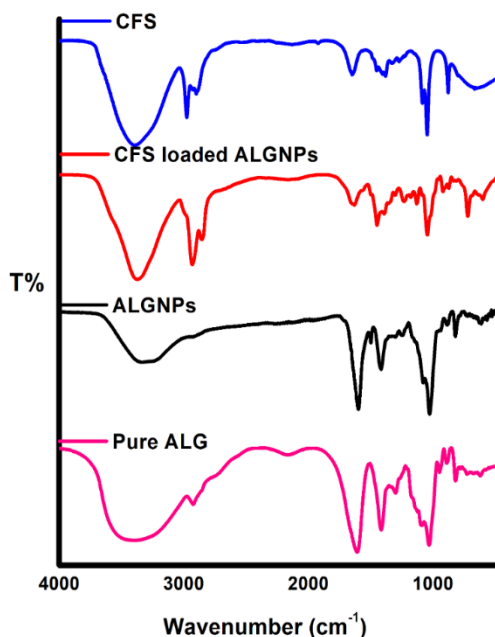


Figure 6. FTIR spectra of pure ALG, pure CFS, ALGNPs and CFS loaded ALGNPs.

The pure CFS spectrum displays the presence of the broad band $-\text{OH}$ group and H bonds in the range 3100–3500 cm^{-1} . In the spectra pure CFS, typical peaks were detected at 2974, 1650, 1381 cm^{-1} for $=\text{C}-\text{H}$ stretching, the C=C group, and the Aryl CH_3 group. The peaks at 1085, 1049 and 880 cm^{-1} was attributed to C–O–C and C–O stresses in the furan ring [11, 43]. The OH band between 3000–3700 cm^{-1} was intensified in the CFS-loaded CSNPs spectrum. The peak at 2974 cm^{-1} in the molecular spectrum in CFS shifted to 2937 cm^{-1} in the CFS-loaded CSNPs spectrum. The peaks of C–O–C and C–O stretching vibration at 1085 and 1049 cm^{-1} in CFS spectra shifted to 1047 and 1021 cm^{-1} in the CFS-loaded CSNPs spectrum. Compared with the pure CFS, absorption peaks at the fingerprint region (1600–400 cm^{-1}) were observed in CFS-loaded CSNPs, which indicated successful entrapment of CFS inside CSNPs. Figure 6 depicts the FTIR spectra of the pure ALG, pure CFS, ALGNPs and CFS loaded ALGNPs. The characteristic peak of the $-\text{OH}$ functional group in the structure of the ALG polymer and the stretching vibration band of the hydrogen bond between the $-\text{OH}$ and $-\text{COOH}$ groups exhibits a wide peak in the range 3000–3600 cm^{-1} . The bands at 1599, 1493 and 1416 cm^{-1} also

revealed asymmetric and symmetric stretching vibrations of the carboxyl group. The bands at 1080 and 1029 cm^{-1} were the tension vibration bands of the C–O band in the C–OH of the sugar group. The FTIR spectrum of ALGNPs revealed characteristic bands between 3000 and 3600 (OH stretching vibrations), 2924 (CH stretching vibrations), and 1080 cm^{-1} (COC stretching vibrations). FTIR spectra obtained for ALG and ALGNPs were compatible with those of literature values [44;45]. The OH band intensified in the spectrum of CFS-loaded ALGNPs, and the peaks at 2974 and 2901 cm^{-1} in CFS shifted to 2933 and 2860 cm^{-1} . The peak of C–O–C stresses shifted from 882 to 723 cm^{-1} wavelength. The peak CFS at 1047 cm^{-1} , which corresponds to the presence of the C–O peak in the furan ring, was loaded on ALGNPs.

3.2 TG analysis

The Perkin–Elmer Diamond TG/DTA analyser was used to investigate the thermal behaviours of the synthesised CFS-loaded CSNPs, and ALGNPs. TG analyses were obtained from 30°C to 600°C with a heating rate of 10°C min^{-1} under N_2 atmosphere with a flow rate of 20 ml/min. The TG and DTG of pure CS, CSNPs, and CFS-loaded CSNPs are displayed in Figures 7 and 8, respectively. The T_{onset} , T_{max} , and residual at 600°C are displayed in Table 2.

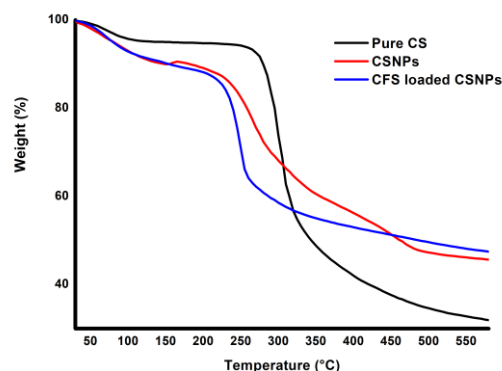


Figure 7. Thermogravimetric (TG) curves of pure CS, CSNPs, CFS-loaded CSNPs.

The TG curve of pure CS (Figure 7) revealed that the two stages of weight loss ranged from 60°C to 480°C. The first occurring weight loss in the range 60°C–120°C could be attributed to water desorption with a weight loss of approximately 6%. The primary degradation of pure CS started at 245°C and completely degraded at approximately 480°C with a weight loss of approximately 58%. Corazzari et al. examined the thermal behaviour of pure CS and obtained the thermogram similar to our study [46]. The main mass loss occurring between 245°C and 480°C could be attributed to the separation of H_2O , NH_3 , CO , CO_2 and CH_3COOH groups because of CS pyrolysis [47]. Comparisons of the

thermograms of pure CS and CSNPs revealed that their thermal behaviour changed (Figure 7 and Table 2).

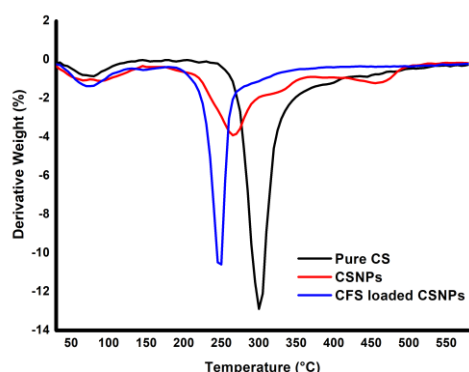


Figure 8. Derivative thermogravimetry (DTG) curves of Pure CS, CSNPs, and CFS-loaded CSNPs.

Table 2 Thermal parameters derived from TG (T_{onset} , T_{max} , and residual mass (%) at 600 °C) for pure CS, CSNPs, and CFS-loaded CSNPs.

Sample	T_{onset} (°C)	T_{max} (°C)	Residual (%) at 600°C
Pure CS	245	300	32
CSNPs	165	235	47
CFS-loaded CSNPs	165	245	48

Figure 7 revealed that approximately 10% water loss in CSNPs occurred in the range 60°C–120°C. The 40% mass loss in CSNPs between 165°C and 480 °C could be attributed to the dehydration of the saccharide rings, depolymerisation, and decomposition of acetylated and deacetylated units [48]. The thermograms of CFS-loaded CSNPs revealed a shift in the second degradation step of nanoparticles compared with CSNPs. This shift could be attributed to the interaction between CFS and the polymeric matrix as well as disturbances in the crystal structure of the nanoparticles. Michailidou et al. revealed a similar observation in the thermograms of Budesonide-loaded CSNPs [49]. The difference in the thermograms of CFS-loaded CSNPs and CSNPs indicated that CFS was loaded on CSNPs.

The TG and DTG of pure ALG, ALGNPs and CFS-loaded ALGNPs are displayed in Figures 9 and 10, respectively. Table 3 depicts the T_{onset} , T_{max} , and residual at 600°C.

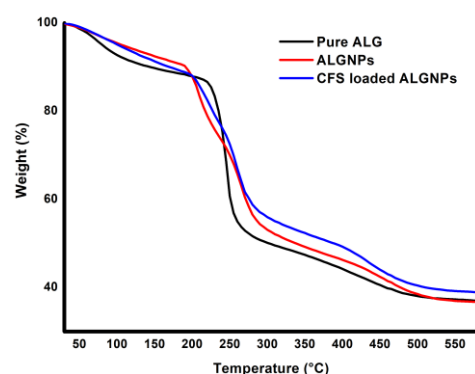


Figure 9. TG curves of pure ALG, ALGNPs and CFS-loaded ALGNPs.

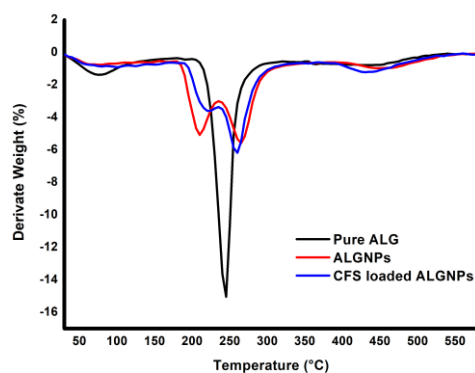


Figure 10. DTG curves of pure ALG, ALGNPs and CFS-loaded ALGNPs.

Table 3 Thermal parameters derived from TG (T_{onset} , T_{max} , and residual mass (%) at 600°C) for pure ALG, ALGNPs and CFS-loaded ALGNPs.

Sample	T_{onset} (°C)	T_{max} (°C)	Residual (%) at 600°C
Pure ALG	200	245	37
ALGNPs	170	210/265/465	37
CFS-loaded ALGNPs	185	225/260/440	39

Figure 9 displays the TG of pure ALG. The TG of pure ALG revealed a three-step weight loss. The initial weight loss of approximately 11% at 60°C–130°C was attributed to the evaporation of moisture and residual water present in the sample. The second degradation stage can be interpreted as crosslinking of polymer networks in the temperature range 200°C–280°C with 38% weight loss. The last decomposition step was interpreted as Na_2CO_3 char formation, which consisted of the structure of sodium ALG polymer [50]. Salisu et al. interpreted the second decomposition step occurring between 200°C–250°C in the thermogram for the ALG polymer to be the

formation of water, CH₄ and CO₂ gas [51]. Figure 10 displays four degradation stages occurring in ALG nanoparticles. The first decomposition stage between 60°C–130°C had 8% moisture loss, the second decomposition at 180°C–240°C had a mass loss of 16%, and the third decomposition at 240°C–280°C had a mass loss of 19%. The final decomposition occurred between the temperatures of 380°C–510°C with a mass loss of 9%. The thermogram results are similar to calcium ALGNPs thermograms obtained by Gokila et al. [52]. Figure 9 displays the TG thermogram of CFS-loaded ALGNPs. Four degradation steps occurred in the thermogram. The initial weight loss of approximately 8% exhibited at 60°C–130°C was attributed to the residual water in the sample. Comparison of the thermograms of ALGNPs and ALGNPs with CFS-loaded ALGNPs revealed that the second, third, and fourth steps slightly shifted to 190°C–235°C with 12% mass loss, to 235°C–280°C with 8% mass loss, and to 390°C–530°C with 9% mass loss, respectively. The shifts in the T_{max} values of CFS-loaded ALGNPs and ALGNPs in Table 3 are interpreted as the result of electrostatic interactions between ALGNPs and CFS. Güncüm et al. synthesised amoxicillin loaded PVA/NaAlg nanoparticles. The thermograms of these nanoparticles shifted with drug loading on ALGNPs as observed in our study [53]. Thus, differences in the thermal characterisation of CFS-loaded ALGNPs and ALGNPs thermograms indicated that CFS was loaded on ALGNPs.

3.3 SEM analysis

The SEM images of CSNPs, ALGNPs, CFS-loaded CSNPs, and ALGNPs are displayed in Figure 11 a-d. SEM analysis provides information of the morphology of the synthesised structures, and the sizes obtained were closer to reality than DLS measurements. DLS determines the apparent size (hydrodynamic radius) of a particle, including hydrodynamic layers formed around hydrophilic particles DLS analysis conducted in a solvent, which is mostly water, medium and as a result given particle size includes solvent molecules size as well. Which lead to an overestimation of the nanoparticle size [54].

When studies have investigated CFS-loaded and CSNPs, and ALGNPs as drug delivery systems, SEM images were obtained to examine the surface morphology. ALGNPs synthesised by various methods such as emulsification/internal gelation, spray dryer, polyelectrolyte complexation, emulsification/external gelation, and evaporation method had a spherical structure [32]. Sarei et al. (2013) reported that ALGNPs were synthesised as a vaccine carrier system for diphtheria with a high loading capacity of 70 ± 0.5 nm in size and spherical morphology [55]. Nallamuthu et al. (2015) revealed that chlorogenic-acid-loaded CSNPs synthesised by the ionic gelation method were homogeneous and spherical [56]. The SEM images of

CFS-loaded CSNPs, and ALGNPs revealed that they had similar spherical morphology and were smaller than 100 nm. Therefore, the morphologies of CFS-loaded CSNPs, and ALGNPs, were consistent with the studies in the literature investigating drug carrier systems, such as CSNPs, and ALGNPs.

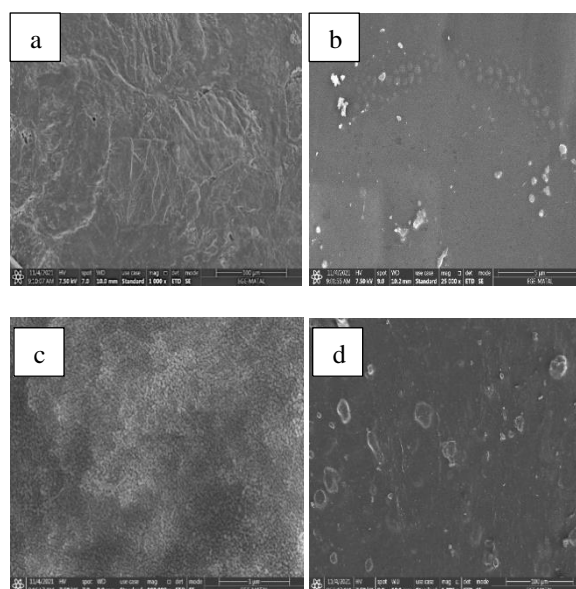


Figure 11. Scanning electron microscopy (SEM) images of a: CSNPs (x 1000), b: CFS-loaded CSNPs (x 25000), c: ALGNPs (x1000), d: CFS-loaded ALGNPs (x 1000).

4. Conclusion

CFS active ingredient found in coffee beans with antidiabetic, anticarcinogenic, and anti-inflammatory properties was loaded into biopolymer nanoparticles such as CS and ALG. CFS-loaded biopolymer nanoparticles were synthesized using the ionic gelation method in high reaction yield. FTIR, TG, SEM and HPLC analysis were performed to characterise CFS-loaded biopolymer nanoparticles. SEM analysis revealed that CFS-loaded CSNPs, and ALGNPs were spherical. Furthermore, FTIR and TG analysis disclosed that CFS was loaded into biopolymer nanoparticles. As a result of HPLC analysis, it is seen that the loading efficiency of CFS on CS nanoparticles is 1.75 times higher than that of ALG nanoparticles. When examined in terms of stability, it was concluded that ALGNPs were more stable in terms of zeta potential. As a continuation of the study, it is planned to conduct in vitro release and cell culture experiments of CFS-loaded polymeric nanoparticles to compare their antidiabetic and anticarcinogenic properties with free CFS.

Acknowledgement

This research is supported by grants from the Ege University Scientific Research Coordination Office (Project No. 21692).

Author's Contributions

Özge VARDAR and Ayça MEHMETOĞLU AL: investigation, conducted experiments, validation, writing-original draft.

Yeliz YILDIRIM: writing, review and editing-original draft, supervision, project administration, funding acquisition.

Ethics

There are no ethical issues after the publication of this manuscript.

References

- [1]. George S.E.; Ramalakshmi K.; Mohan Rao L.J. (2008) A perception on health benefits of coffee. *Crit Rev Food Sci Nutr* 48, 464-486.
- [2]. Ren Y.; Wang C.; Xu J.; Wang S. (2019) Cafestol and kahweol: A review on their bioactivities and pharmacological properties. *Int J Mol Sci* 20, 4238.
- [3]. Moeenfarid M.; Cortez A.; Machado V.; et al. (2016) Anti-angiogenic properties of Cafestol and Kahweol palmitate diterpene esters. *J Cell Biochem* 117, 2748-2756.
- [4]. Mellbye F.B.; Jeppesen P.B.; Hermansen K.; Gregersen S. (2015) Cafestol, a bioactive substance in coffee, stimulates insulin secretion and increases glucose uptake in muscle cells: studies in vitro. *J Nat Prod* 78, 2447-2451.
- [5]. Mellbye F.B.; Jeppesen P.B.; Shokouh P.; et al. (2017) Cafestol, a bioactive substance in coffee, has antidiabetic properties in KKAY mice. *J Nat Prod* 80, 2353-2359.
- [6]. Loureiro L.M.R.; Reis C.E.G.; da Costa T.H.M. (2018) Effects of coffee components on muscle glycogen recovery: a systematic review. *Int J Sport Nutr Exerc Metab* 28, 284-293.
- [7]. Moolgavkar S.H. (1978) The multistage theory of carcinogenesis and the age distribution of cancer in man. *J Natl Cancer Inst* 61, 49-52.
- [8]. Kotowski U.; Heiduschka G.; Seemann R.; et al. (2015) Effect of the coffee ingredient cafestol on head and neck squamous cell carcinoma cell lines. *Strahlenther Onkol* 191, 511-517.
- [9]. Lima C.S.; Spindola D.G.; Bechara A.; et al. (2017) Cafestol, a diterpene molecule found in coffee, induces leukemia cell death. *Biomed Pharmacother* 92, 1045-1054.
- [10]. Lee K.J.; Choi J.H.; Jeong H.G. (2007) Hepatoprotective and antioxidant effects of the coffee diterpenes kahweol and cafestol on carbon tetrachloride-induced liver damage in mice. *Food Chem Toxicol* 45, 2118-2125.
- [11]. Ballica G.; Çevikbaş H.; Ulusoy S.; Yıldırım Y. (2020) The synthesis of novel Cafestol loaded zinc oxide nanoparticles and their characterization. *Appl Nanosci* 10, 4263-4272.
- [12]. Thomas S.; Pius A.; Gopi S. (2020) Handbook of Chitin and Chitosan: Volume 2: Composites and Nanocomposites from Chitin and Chitosan, Manufacturing and Characterisations. Elsevier.
- [13]. Zargar V.; Asghari M.; Dashti A. (2015) A review on chitin and chitosan polymers: structure, chemistry, solubility, derivatives, and applications. *Chem Bio Eng Reviews* 2, 204-226.
- [14]. Zhou X.; Guo L.; Shi D.; Duan S.; Li J. (2019) Biocompatible chitosan nanobubbles for ultrasound-mediated targeted delivery of doxorubicin. *Nanoscale Res Lett* 14, 1-9.
- [15]. He T.; Wang W.; Chen B.; Wang J.; Liang Q.; Chen B. (2020) 5-Fluorouracil monodispersed chitosan microspheres: Microfluidic chip fabrication with crosslinking, characterization, drug release and anticancer activity. *Carbohydr Polym* 236, 116094.
- [16]. Hamedinasab H.; Rezayan A.H.; Mellat M.; Mashreghi M.; Jaafari M.R. (2020) Development of chitosan-coated liposome for pulmonary delivery of N-acetylcysteine. *Int J Biol Macromol* 156:1455-1463.
- [17]. Buyuk N.I.; Arayici P.P.; Derman S.; Mustafaeva Z.; Yucel S. (2020) Synthesis of chitosan nanoparticles for controlled release of amiodarone. *Indian J Pharm Sci* 82:131-138.
- [18]. Gelperina S.; Kisich K.; Iseman M.D.; Heifets L. (2005) The potential advantages of nanoparticle drug delivery systems in chemotherapy of tuberculosis. *Am J Respir Crit Care Med* 172, 1487-1490.
- [19]. Paques J.P.; van der Linden E.; van Rijn C.J.; Sagis L.M. (2014) Preparation methods of alginate nanoparticles. *Adv Colloid Interface Sci* 209:63-171.
- [20]. Chiu H.I.; Ayub A.D.; Mat Yusuf S.N.A.; et al. (2020) Docetaxel-loaded disulfide cross-linked nanoparticles derived from thiolated sodium alginate for colon cancer drug delivery. *Pharmaceutics* 12(1), 1-25.
- [21]. Jayapal J.J.; Dhanaraj S. (2017) Exemestane loaded alginate nanoparticles for cancer treatment: Formulation and in vitro evaluation. *Int J Biol Macromol* 105, 416-421.
- [22]. Fleten, K. G., Hyldbakk, A., Einen, C., Benjakul, S., Strand, B. L., Davies, C. D. L., ... & Flatmark, K. (2022) Alginate Microsphere Encapsulation of Drug-Loaded Nanoparticles: A Novel Strategy for Intraperitoneal Drug Delivery. *Marine Drugs* 20(12), 744.
- [23]. Joseph, J. J., Sangeetha, D., & Shivashankar, M. (2019) In vitro release and cytotoxic studies of novel alginate nanocarrier for the antitumor drug: Sunitinib. *Regen Eng Transl Med*, 5, 220-227.
- [24]. Rai, V. K., Kumar, A., Pradhan, D., Halder, J., Rajwar, T. K., Sarangi, M. K., ... & Rath, G. Spray-Dried (2024) Mucoadhesive Re-dispersible Gargle of Chlorhexidine for Improved Response Against Throat Infection: Formulation Development, In Vitro and In Vivo Evaluation. *AAPS PharmSciTech*, 25(2), 31.
- [25]. Calvo P.; Remuñan-López C.; Vila-Jato J.L.; Alonso M.J. (1997) Chitosan and chitosan/ethylene oxide-propylene oxide block copolymer nanoparticles as novel carriers for proteins and vaccines. *Pharm Res* 14, 1431-1436. 25.2
- [26]. Vila A.; Sánchez A.; Janes K et al. (2004) Low molecular weight chitosan nanoparticles as new carriers for nasal vaccine delivery in mice. *Eur J Pharm Biopharm* 57, 123-131.
- [27]. Rajaonarivony M.; Vauthier C.; Couarraze G.; Puisieux F.; Couvreur P. (1993) Development of a new drug carrier made from alginate. *J Pharm Sci* 82, 912-917.
- [28]. Dias R.C.E.; Campanha F.G.; Vieira L.G.E et al. (2010) Evaluation of kahweol and cafestol in coffee tissues and roasted coffee by a new high-performance liquid chromatography methodology. *J Agric Food Chem* 58, 88-93.
- [29]. Silva J.A.; Borges N.; Santos A.; Alves A. (2012) Method validation for cafestol and kahweol quantification in coffee brews by HPLC-DAD. *Food Anal Methods* 5, 1404-1410.

- [30]. Guideline IHT (2005) Validation of analytical procedures: text and methodology. Q2 (R1), 1(20), 05.
- [31]. Oh J.W.; Chun S.C.; Chandrasekaran M. (2019) Preparation and in vitro characterization of chitosan nanoparticles and their broad-spectrum antifungal action compared to antibacterial activities against phytopathogens of tomato. *Agron J* 9(1), 21.
- [32]. Jain A.; Thakur K.; Sharma G.; Kush P.; Jain U.K. (2016) Fabrication, characterization and cytotoxicity studies of ionically cross-linked docetaxel loaded chitosan nanoparticles. *Carbohydr Polym* 137, 65-74.
- [33]. Çakır M.A.; İcyer N.C.; Tornuk F. (2020) Optimization of production parameters for fabrication of thymol-loaded chitosan nanoparticles. *Int J Biol Macromol* 151, 230-238.
- [34]. Paques J.P.; Sagis L.M.; van Rijn C.J.; van der Linden E. (2014) Nanospheres of alginate prepared through w/o emulsification and internal gelation with nanoparticles of CaCO₃. *Food Hydrocoll* 40, 182-188.
- [35]. Mokhtari S.; Jafari S.M.; Assadpour E. (2017) Development of a nutraceutical nano-delivery system through emulsification/internal gelation of alginate. *Food Chem* 229, 286-295.
- [36]. Lunardi C.N.; Gomes A.J.; Rocha F.S.; De Tommaso J.; Patience G.S. (2021) Experimental methods in chemical engineering: Zeta potential. *Can J Chem Eng* 99, 627-639.
- [37]. Bakhshi M.; Ebrahimi F.; Nazarian S et al. (2017) Nano-encapsulation of chicken immunoglobulin (IgY) in sodium alginate nanoparticles: In vitro characterization. *Biologicals* 49, 69-75.
- [38]. de Castro Spadari C. (2019) Alginate nanoparticles as non-toxic delivery system for miltefosine in the treatment of candidiasis and cryptococcosis. *Int J Nanomed* 14, 5187.
- [39]. Sarei F.; Dounighi N.M.; Zolfagharian H.; Khaki P.; Bidhendi S.M. (2013) Alginate nanoparticles as a promising adjuvant and vaccine delivery system. *Indian J Pharm Sci* 75, 442.
- [40]. Silvestro, I., Francolini, I., Di Lisio, V., Martinelli, A., Pietrelli, L., Scotto d'Abusco, A., ... & Piozzi, A. (2020). Preparation and characterization of TPP-chitosan crosslinked scaffolds for tissue engineering. *Materials*, 13(16), 3577.
- [41]. Costa, M. J., Marques, A. M., Pastrana, L. M., Teixeira, J. A., Sillankorva, S. M., & Cerqueira, M. A. (2018). Physicochemical properties of alginate-based films: Effect of ionic crosslinking and mannuronic and guluronic acid ratio. *Food hydrocolloids*, 81, 442-448.
- [42]. Terrile E.A.; Marcheafave G.G.; Oliveira S.G et al. (2016) Chemometric analysis of UV characteristic profile and infrared fingerprint variations of coffee Arabica green beans under different space management treatments. *J Braz Chem Soc* 27, 1254-1263.
- [43]. Derkus B.; Emregul E., Emregul K.C.; Yucesan C. (2014) Alginate and alginate-titanium dioxide nanocomposite as electrode materials for anti-myelin basic protein immunosensing. *Sens Actuators B Chem* 192, 294-302.
- [44]. El-Shamy O.A.; El-Azabawy R.E.; El-Azabawy O. (2019) Synthesis and characterization of magnetite-alginate nanoparticles for enhancement of nickel and cobalt ion adsorption from wastewater. *J Nanomater* Article ID 6326012:1-8
- [45]. Brito D.; Campana-Filho S.P. (2007) Kinetics of the thermal degradation of chitosan. *Thermochim Acta* 465, 73-82.
- [46]. Corazzari I.; Nisticò R.; Turci F et al. (2015) Advanced physico-chemical characterization of chitosan by means of TGA coupled on-line with FTIR and GCMS: Thermal degradation and water adsorption capacity. *Polym Degrad Stab* 112, 1-9.
- [47]. Zhang H.; Zhao Y. (2015) Preparation, characterization and evaluation of tea polyphenol-Zn complex loaded β -chitosan nanoparticles. *Food Hydrocoll* 48, 260-273.
- [48]. Michailidou G.; Ainali N.M.; Xanthopoulou E et al. (2020) Effect of poly (vinyl alcohol) on nanoencapsulation of budesonide in chitosan nanoparticles via ionic gelation and its improved bioavailability. *Polym J* 12, 1101-1023.
- [49]. Swamy T.M.; Ramaraj B.; Lee J.H. (2008) Sodium alginate and its blends with starch: thermal and morphological properties. *J Appl Polym Sci* 109, 4075-4081.
- [50]. Salisu A.; Sanagi M.M.; Abu Naim A et al. (2016) Alginate graft polyacrylonitrile beads for the removal of lead from aqueous solutions. *Polym Bull* 73, 519-537.
- [51]. Gokila S.; Gomathi T.; Sudha P.N.; Anil S. (2017) Removal of the heavy metal ion chromium (VI) using Chitosan and Alginate nanocomposites. *Int J Biol Macromol* 104, 1459-1468.
- [52]. Güncüm E.; Işıklan N.; Anlaş C et al. (2018) Development and characterization of polymeric-based nanoparticles for sustained release of amoxicillin—an antimicrobial drug. *Artif Cells Nanomed Biotechnol* 46, 964-973.
- [53]. Bootz A.; Vogel V.; Schubert D.; Kreuter J. (2004) Comparison of scanning electron microscopy, dynamic light scattering and analytical ultracentrifugation for the sizing of poly (butyl cyanoacrylate) nanoparticles. *Eur J Pharm Biopharm* 57, 369-375.
- [54]. Daemi H.; Barikani M. (2012) Synthesis and characterization of calcium alginate nanoparticles, sodium homopolymannuronate salt and its calcium nanoparticles. *Sci Iran* 19, 2023-2028.
- [55]. Gazori T.; Khoshayand M.R.; Azizi E et al. (2009) Evaluation of alginate/chitosan nanoparticles as antisense delivery vector: formulation, optimization and in vitro characterization. *Carbohydr Polym*. 77, 599-606.
- [56]. Nallamuthu I.; Devi A.; Khanum F. (2015) Chlorogenic acid loaded chitosan nanoparticles with sustained release property, retained antioxidant activity and enhanced bioavailability. *Asian J Pharm Sci* 10, 203-211.